HYDROGENATION OF BIOMASS DERIVED OXYGENATES

by

Huibo Sheng

A dissertation submitted to the Faculty of the University of Delaware in partial fulfillment of the requirements for the degree of Doctor of Philosophy in Chemical Engineering

Fall 2017

HYDROGENATION OF BIOMASS DERIVED OXYGENATES

by

Huibo Sheng

Approved: _____
Eric M. Furst, Ph.D.
Chair of the Department of Chemical and Biomolecular Engineering

Approved: _____
Babatunde A. Ogunnaike, Ph.D.
Dean of the College of Engineering

Approved: _____
Ann L. Ardis, Ph.D.
Senior Vice Provost for Graduate and Professional Education

I certify that I have read this dissertation and that in my opinion it meets the academic and professional standard required by the University as a dissertation for the degree of Doctor of Philosophy.

Signed: _____

Raul F. Lobo, Ph.D.
Professor in charge of dissertation

I certify that I have read this dissertation and that in my opinion it meets the academic and professional standard required by the University as a dissertation for the degree of Doctor of Philosophy.

Signed: _____

Michael T. Klein, Sc.D.
Member of dissertation committee

I certify that I have read this dissertation and that in my opinion it meets the academic and professional standard required by the University as a dissertation for the degree of Doctor of Philosophy.

Signed: _____

Feng Jiao, Ph.D.
Member of dissertation committee

I certify that I have read this dissertation and that in my opinion it meets the academic and professional standard required by the University as a dissertation for the degree of Doctor of Philosophy.

Signed: _____

Bingjun Xu, Ph.D.
Member of dissertation committee

I certify that I have read this dissertation and that in my opinion it meets the academic and professional standard required by the University as a dissertation for the degree of Doctor of Philosophy.

Signed: _____

Klaus H. Theopold, Ph.D.
Member of dissertation committee

ACKNOWLEDGMENTS

I'd like to thank my advisor, Dr. Raul Lobo, who guided me into the world of catalysis and taught me everything that I needed during the journey of PhD. I really like your philosophy of training a PhD student to conduct scientific research independently and it works very well with me. Though I've met numerous problems and difficulties during the research, you are always full of great ideas to inspire me to move forward. I'd like also to acknowledge my thesis committee members, Dr. Michael Klein, Dr. Feng Jiao, Dr. Bingjun Xu, and Dr. Klaus Theopold. I really appreciate the nice discussions and suggestions from your view of expertise during each time we meet, without which I would not be able to finish this dissertation.

I'm glad that I met a lot of great lab mates in the past few years. Thank you all, the Lobo group members: Thank you Dr. Marta Leon Garcia, Dr. Adriana Aristizabal, Dr. Bahar Ipek, Dr. Molly Koehle, Dr. Jelve Mirzababaei, during the past five years, I'm so happy to share the office with you all, who made this little room full of sweet candies when I was down and always encouraged me to keep going forward. I'd like to thank the postdoctoral researchers, Dr. Na Ji, Dr. Qingling Liu, Dr. Shewangizaw Forsido, Dr. Matt Wulfer, Dr. Takahiko Moteki, Dr. Weiqing Zheng, Dr. Young Jin Kim, Dr. Efterpi Vasileiadou, and Dr. Ali Mehdad. You were the best persons to turn to when I had questions in the research and thank you for your helpful discussions and suggestions. Also, I'd like to thank all the graduate students, Dr. Jang Ho Yun, Dr. Trong Pham, Dr. Jason Loiland, Dr. Eyas Mahmoud, Edward Schreiner, and Chen-Yu Chou, I really enjoy the days working with you guys.

Finally, I would like to thank my parents. Though you are thousands of miles away, I know you are always there to support me. Thank you Yan for your eternal love.

TABLE OF CONTENTS

LIST OF TABLES

LIST OF FIGURES

ABSTRACT

Biomass, an abundant, renewable, and near carbon-neutral feedstock, has the potential to supply many valuable chemicals and biofuels and is as an alternative to crude oil feedstocks. Biomass-derived species, however, naturally contain a high oxygen concentration, which lowers the energy density of the biomass-derived molecules, and thus are not feasible for direct use. The development of selective catalytic technology for the removal of this 'excess' oxygen from biomass-derived species is essential to making these technologies a practical reality.

At the same time, shale gas production has increased rapidly since 2007 in the U. S. due to the new extraction technologies such as hydraulic fracturing and horizontal drilling. As a clean, inexpensive, and abundant carbon source, methane has attracted scientists all over the world to research C1 chemistry and transform this molecule into more valuable species.

This dissertation focuses on the development of catalytic processes for biomass derived oxygenates upgrading and natural gas conversion into petrochemicals. In this dissertation, three types of heterogeneous catalysts are investigated: catalysts for the hydrodeoxygenation of furfural (Cu supported on silica), catalysts for the selective hydrogenation of aliphatic carboxylic acids to aldehydes (first-row metal oxides), and catalysts for the non-oxidative coupling of methane (based on Mo_2C).

The selective hydrodeoxygenation of furfural to 2-methylfuran was investigated over iron-promoted copper catalyst as the first part of the thesis. Iron was added as a promoter to the silica supported copper catalyst and the roles that the iron

play in this reaction were identified with various characterization methods. In addition, the selectivity of this reaction was investigated under different pre-treatment and reaction conditions.

The selective hydrogenation of carboxylic acids to the corresponding aldehydes was carried out on chromium containing catalyst. Different types of chromium oxide catalysts from different synthetic methods were evaluated with a series of (small) carboxylic acids of propionic acid (C3) to hexanoic acid (C6). The active phase of the catalyst was characterized and the reaction mechanism was studied further. Finally, a few kinetic studies were performed to validate the reaction rate expression derived from the proposed mechanism.

As a study for natural gas utilization, the methane coupling reaction to ethylene in a single step and oxidants free condition was investigated with Mo_2C/ZSM-5 catalyst. The effect of zeolite acidity was investigated in the methane activation reaction to control the products selectivity. A boron containing zeolite was synthesized and the zeolite structure evolution was investigated through the reaction. The active molybdenum species were characterized with surface and bulk techniques to find out the surface reaction with methane.

Chapter 1

INTRODUCTION

This dissertation focuses on the development of catalytic processes for biomass derived oxygenates upgrading and natural gas conversion. The overall goal is to produce valuable chemicals and fuels from renewable resources such as biomass, and inexpensive and abundant raw materials such as natural gas. These chemical reactions are facilitated using heterogeneous catalysts by lowering the energy barriers and tuning the reaction selectivity. In this dissertation, three types of heterogeneous catalysts are investigated: catalysts for the hydrodeoxygenation of furfural, catalysts for the selective hydrogenation of aliphatic carboxylic acids to aldehydes, and for the non-oxidative coupling of methane.

This introductory chapter presents essential background related to the production of biofuels and value-added chemicals from renewable biomass and shale gas (methane). Today fossil fuels, including coal, petroleum and natural gas, account for more than 80% of U. S.'s total energy consumption (Figure 1.1). However, concerns for the non-sustainability and possible negative effects of fossil fuels on our environment are increasing. It is important for society to take steps that move it away from its dependence on fossil fuels and to take steps towards development of renewable and carbon-neutral energy sources.

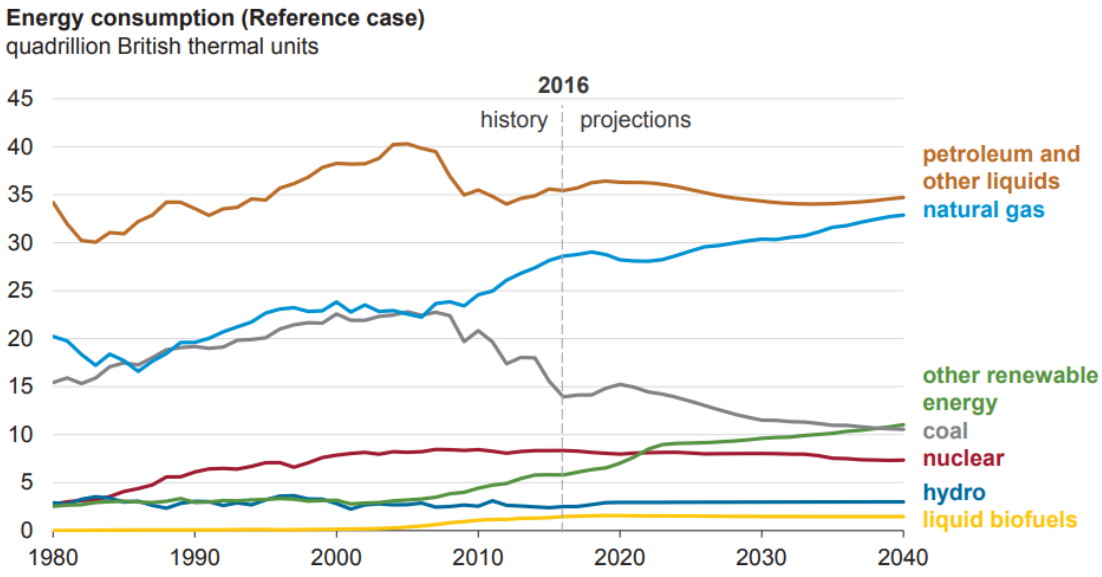

Figure 1.1 1980-2040 U. S. energy consumption. Source: U. S. Energy Information Administration[1]

The last decade has witnessed the fast development of biomass as a source of liquid fuels. Biomass, which is abundant and renewable, has a much smaller carbon footprint than fossil fuels. Also, biomass can supply energy locally and fits well with the current fuel infrastructure, which is a great advantage when the problem is viewed through a global perspective. However, biomass derivatives naturally contain high oxygen concentration, which lowers the energy density of the biomass-derived molecules, and thus are not feasible for direct use as fuels.[2] Therefore the development of selective catalytic technology for the removal of 'excess' oxygen from biomass-derived molecules is essential to making these technologies a practical reality.

At the same time, shale gas is now accessible at relatively low cost thanks to hydraulic fracturing technology and this source of hydrocarbons is projected to

account for 40% of U. S. energy production by 2040 (Figure 1.2). Although methane can be burned directly as a fuel with a highest theoretical energy content of 55.6 MJ/kg (among the hydrocarbons[3]), the transportation and storage of natural gas still require a huge effort both from scientific breakthroughs and direct capital investments. Therefore effective utilization of methane is of great interest and importance to the chemical industry because of the rapid growth of shale gas production and the low cost of this raw material.[4] Heterogeneous catalytic process is essential in chemical industry and provides solutions to either biomass upgrading and methane conversion.

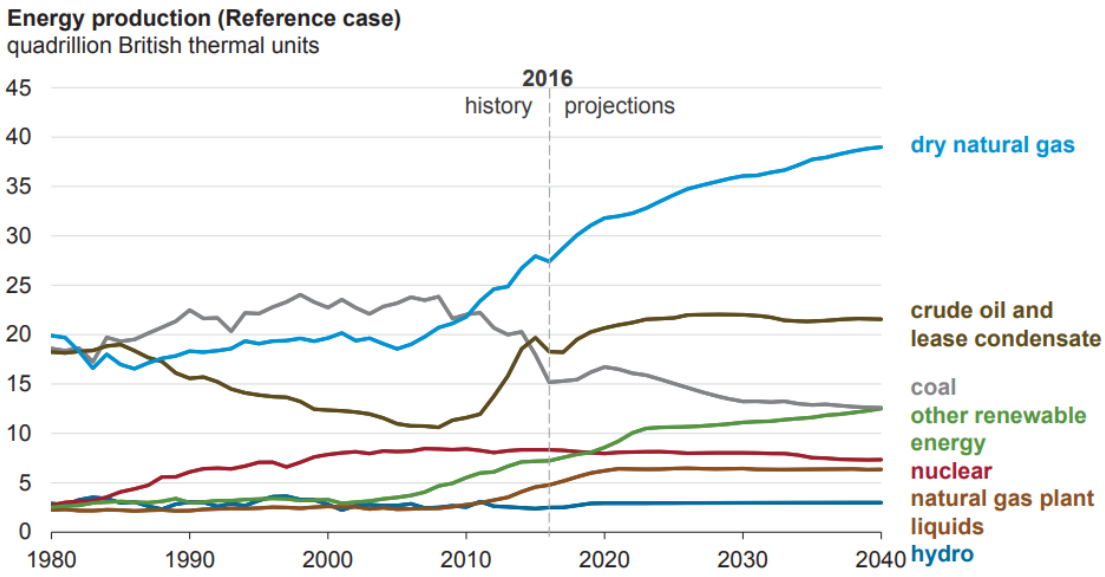

Figure 1.2 1980-2040 U. S. energy production. Source: U. S. Energy Information Administration[1]

1.1 Biomass Upgrading

There are three main carbon sources in nature that are potential candidates for renewable energy sources: starch, cellulose and hemicellulose.[5] Cellulose is the

most abundant carbon source among the three, but due to its highly crystalline structure and insolubility, cellulose is resistant to most chemical and enzymatic attack and is thus hard to utilize. The first generation of biomass fuels mainly derived from sugarcane and corn starch. Human or livestock digestible sugar-based biomass can be converted to biofuels such as ethanol, which are already used as additives to gasoline and can be directly used in a fuel cell to produce electricity.[6] However, producing energy from food crops could potentially give rise to local food shortage problems. In addition, these sugar-based carbon sources have higher value for food or feed applications than for fuel or chemicals. Therefore, scientists have moved towards developing second-generation biofuels, which are derived from non-edible hemicellulose and do not have a significant impact on human food or livestock feed demands.

1.1.1 Hydrogenation of Furfural

Furfural is viewed as a potential platform chemical for biofuels. It can be produced, for example, by hydrolysis and dehydration of xylan. However, furfural cannot be directly used as fuels because it polymerizes rapidly. Furfural contains a relatively high concentration of oxygen and needs hydrodeoxygenation to increase its energy density.[2] A simplified reaction network for HDO of furfural is depicted in Figure 1.3.

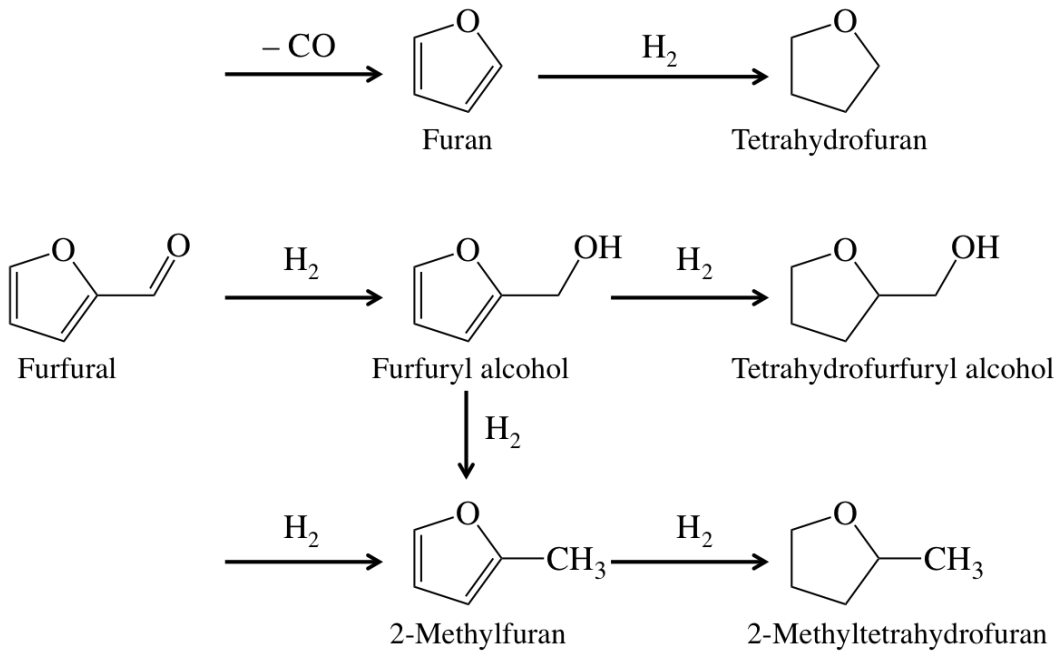

Figure 1.3 A set of three (connected) furfural reaction pathways

In the reaction network of Figure 1.3, depending on the catalyst and the reaction conditions, furfural can go through decarbonylation, hydrogenation, or hydrodeoxygenation process. If sufficient hydrogen is provided with a catalyst of strong hydrogenation ability, the hydrogenation of furan ring can occur, giving rise to over hydrogenated products of tetrahydrofuran.

The hydrogenation of furfural can be achieved either in liquid phase or in vapor phase. Typically liquid phase catalytic hydrogenation of furfural requires high pressure and high temperature,[7] and undesired side reactions can also take place (e.g., ring hydrogenation or ring opening reaction) reducing selectivity.[8] In contrast to the liquid phase reaction, vapor phase reaction is favored for its mild reaction conditions and good selectivity to desired products such as furfuryl alcohol.[9] The vapor phase method is widely used in the commercial manufacturers where the

furfural feedstock is preheated to a vapor, mixed with hydrogen, and pass through a continuous tubular reactor containing copper catalysts.[10]

Noble metals have been investigated for their known hydrogenation abilities. Palladium has been reported by many groups[11-15] to be an excellent catalyst to produce furan. Sitthisa, for example, carried out experiments using Pd-Cu[15] catalyst, on which the formation of acyl intermediate (an important intermediate during decarbonylation) was less likely. Therefore, the rate of decarbonylation was reduced and the rate of hydrogenation is increased. Several studies on supported platinum showed great performance of platinum to hydrogenate furfural to furfuryl alcohol.[16] Such noble metals as palladium and platinum, however, are not profitable for large-scaled applications.

Copper-chromate has been often used as a commercial catalyst of furfural hydrogenation to produce furfuryl alcohol[7] with high conversion (~98%) and yield (96% to 99%) since the 1950s. However, the CuCr-based catalysts were proved to be toxic and can cause severe environmental problems.[2] Efforts have been taken to develop other new, nontoxic catalysts such as Raney nickel[11] and Cu/MgO,[17] but were not very successful due to difficult reaction conditions.

Transition metal carbides have been extensively studied in the past few decades, since Levy and Boudart reported the Pt-like properties of tungsten carbides.[18] Surface science studies[19, 20] suggest molybdenum carbides are promising in selective hydrodeoxygenation of furfural, however the molybdenum carbides catalyst suffers from rapid deactivation problems.[21]

Therefore, an inexpensive, non-toxic, and stable catalyst is highly desirable for the selective hydrodeoxygenation of furfural to 2-methylfuran. In addition to this

dissertation, a number of researchers have investigated different catalysts and reaction pathways and the results are discussed in Chapter 3.[21-24]

1.1.2 Hydrogenation of Carboxylic Acids

Aliphatic and aromatic carboxylic acids such as acetic acid, palmitic acid, stearic acid, benzoic acid, and phenyl alkanoic acid have very broad application in the chemical industry, including the production of polymers, pharmaceuticals, and food additives.[25] Industrial scale production of carboxylic acids are based on the use of petrochemicals as feedstocks, namely from the oxidation of hydrocarbons, alcohols, and from hydrocarboxylation of olefins.[26] Recent reports have shown that a renewable route that carboxylic acids can be production from lignocellulosic biomass.[27] Through different catalytic processes, carboxylic acids can be converted to a board range of chemicals including aldehydes, alcohols, esters, ketones, alkanes, and olefins (Figure 1.4).

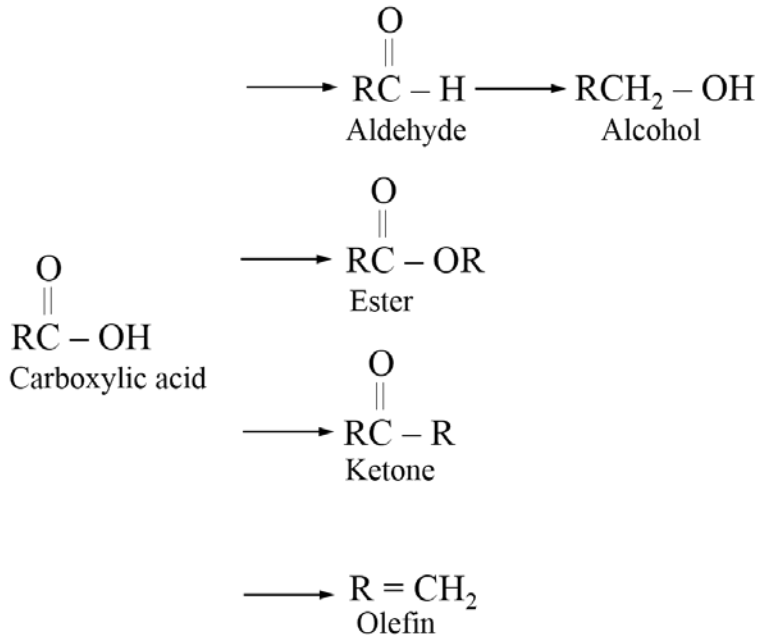

Figure 1.4 Catalytic conversion pathways of carboxylic acid via selective hydrogenations[28-33]

Hydrogenation of carboxylic acids leads to the hydrogenated intermediates aldehydes and alcohols. Several metal oxides such as Fe_2O_3, Cr_2O_3, ZrO_2, and V_2O_5 have been reported to selective convert acetic acid or other fatty acids to the corresponding aldehydes.[30, 33, 34] However, little if any information on reaction mechanism has been investigated in the past with these metal oxide catalysts, or only a general mechanism was hypothesized.[34] Metal catalysts such as Ru, Ru-Cu, and Pt have been successfully applied in the conversion of acids to alcohols,[35-37] but the capital cost of alcohol production can be high as well as the long-term stability is yet to be studied with these metal catalysts.

Apart from the hydrogenation to aldehydes and alcohols, carboxylic acids can also be converted to other chemical moieties such as esters, ketones, and olefins. For

instance, Ce-ZrO_2,[31] TiO_2[38] and many other catalysts can convert carboxylic acids to ketones via ketonization reactions. Kim and Barteau investigated the ketonization of acetic acid on TiO_2 surface, claiming that acetone is formed via bimolecular action of surface acetates, which are formed from dissociatively absorbed acetic acid.[38] Miller, Nelson, and Byrne[32] reported that 1-alkenes of one less carbon can be selectively produced from carboxylic acids on Pd or Rh catalysts, with CO as the side product and at an expense of acetic anhydride being converted to acetic acids.

With so many potential side-reactions, the selective hydrogenation of carboxylic acids to the aldehydes needs to be accomplished with an inexpensive and stable catalyst, while the reaction mechanism study is also essential to apply such catalyst to a variety of carboxylic acids. In Chapter 4 we investigate this reaction process over Cr-containing catalysts.

1.2 Methane Conversion to Higher Hydrocarbons

Since 2007 shale gas production has increased rapidly in the U. S. due to the new technologies such as hydraulic fracturing and horizontal drilling. As a clean, inexpensive, and abundant chemical resource, methane has attracted scientists all over the world to devote efforts in the C1 chemistry. The conversion of methane to higher hydrocarbons can be categorized into indirect methods and direct methods (Figure 1.5). Indirect methods use carbon monoxide and hydrogen—produced via methane steam reforming, carbon dioxide reforming, or partial oxidation—as intermediates of the Fischer-Tropsch process.[39] Direct methods involve methane coupling with or without the presence of an oxidant, known respectively as oxidative coupling of methane (OCM) and non-oxidative coupling of methane (NCM).[40]

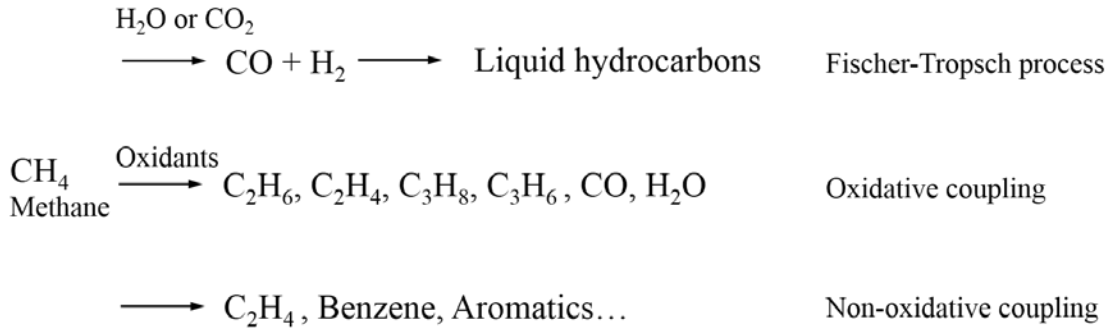

Figure 1.5 Methane conversion to higher hydrocarbons

Methane steam reforming or CO_2 reforming are essential industrial processes for the manufacture of syngas, namely mixtures of hydrogen and carbon monoxide.[41] Typically, the production and purification of syngas can account for 60 – 70% of the capital and running costs in a Fischer-Tropsch plant.[42] Catalysts such as nickel-alumina have been investigated in detail including the reaction mechanism and kinetics of methane steam reforming.[43] Coke formation, which is favored under the same reaction condition as the steam reforming, can be significantly reduced with an addition of small amount of tin.[44] For the Fischer-Tropsch synthesis, cobalt-based catalysts can convert mixture of H_2/CO to higher C5+ hydrocarbons with the best compromise between the performance and cost.[45] The Fischer-Tropsch process is a great method since it is compatible with a variety of feedstocks (especially with solid carbon mixtures such as coals and biomass) through gasification, however it may not be the most efficient method for methane, since methane is already a simple and pure compound. Therefore, methane direct conversion to hydrocarbons can reduce the capital cost in a chemical plant due to the fewer reaction steps than in the indirect methods.

The topic of methane direct conversion has been extensively studied recently, with many processes and reactions reported including oxidative coupling of methane and non-oxidative coupling of methane. Oxidative coupling requires extra oxidants co-feeding with the methane. Since methane has an unusual high C-H bond strength (435 kJ/mol), by adding an oxidant can theoretically reduce the required reaction free energy. For example, the introduction of O_2 to the reaction of methane coupling to ethylene reduces the reaction free energy from 79.0 kJ/mol to -144.6 kJ/mol at 400 K.[46] Transition metal oxides including Sn, Pb, Sb, Bi, Tl, and Mn oxides were reported for their high reactivity in synthesis of ethylene from oxidative coupling of methane.[47] The introduction of an oxidant, however, potentially increases the capital cost and may decrease the selectivity and lead to over-oxidation to CO_2.

For the non-oxidative coupling of methane, Wang and co-workers pioneered one step methane dehydroaromatization reaction on Mo/ZSM-5.[48] It is reported that only 1.4% of methane was fully converted to benzene at 973 K on HZSM-5 catalysts. A higher conversion (7.2%) was achieved in the presence of Mo in the sample.[48] An induction period was also observed with MoO_3/HZSM-5, implying that the actual active phase was formed in-situ from the MoO_3/HZSM-5 starting material.[49, 50] Further research has revealed that the primary reaction of C–H bond dissociation occurs on Mo_2C nanoparticle surface.[51] At the surface, a molybdenum-carbene-like intermediate, CH_2=Mo, is involved in the proposed mechanism. Ethylene is believed to be the primary product from the coupling of the surface carbene species in these samples.[51, 52] Ethylene oligomerization reactions take place simultaneously leading to the formation of aromatics species, the thermodynamically favored products at the

high reaction temperature.[53] The formation of aromatics is catalyzed by Brønsted acid sites in the zeolite pores and the material operates as a bi-functional catalysts.[54]

In this thesis, an oxidants-free, one-step methane to ethylene conversion process has been developed and the catalytic properties of the novel materials have been investigated.

1.3 Scope of the Thesis

This thesis focuses on the development of catalytic materials and pathways for the upgrading of biomass derived oxygenates to biofuels and chemicals, and the conversion of natural gas, with emphasis on the catalytic materials development, characterization, and thus understanding the reaction mechanisms. Three research aims will be discussed in detail in the following chapters: two of them focused on the selective oxygen removal from the biomass derived oxygenates, and one presented the non-oxidative coupling of methane to ethylene.

Chapter 2 provides background information on the materials characterization techniques, analytical equipment, and the reactor used to collect and analyze the data presented in this dissertation. To be specific, physical and chemical characterization techniques, spectroscopic techniques, and an experimental set-up for catalysts evaluation are described in the chapter. Materials general information is introduced, but the detailed synthesis process and experimental procedures of the characterization are not discussed in this chapter; they can be found in the reaction-specific chapters 3 – 5.

Chapter 3 presents an investigation of the selective hydrodeoxygenation of biomass derived furfural to 2-methylfuran on iron-promoted copper supported on silica catalyst. As previous study showed that copper based catalysts are selective for

furfural conversion to furfuryl alcohol, an introduction of second metal to copper can potentially enhance the reaction rates and tune the reaction selectivity. In this chapter, iron was investigated as the additional metal and the roles of the iron play in this reaction were identified with various characterization methods. In addition, the selectivity of this reaction was investigated under different pre-treatment and reaction conditions. Finally an iron-promoted copper catalyst was found to convert furfural to 2-methylfuran selectively.

Chapter 4 focuses on the development of an effective catalyst for the selective hydrogenation of carboxylic acids to the corresponding aldehydes. As carboxylic acids can be produced from biomass, this process provides a manufacture route of aldehydes from renewable feedstocks. The commercial chromium oxide catalyst was evaluated with a series of fatty acids of propionic acid (C3) to hexanoic acid (C6). The active phase of the catalyst was characterized and the reaction mechanism was studied further. Finally, a few kinetic studies were performed to validate the reaction rate expression derived from the proposed mechanism.

Chapter 5 discusses the catalytic methane coupling reaction to ethylene with single step and oxidants free condition. Inspired by the Mo_2C/HZSM-5 catalyst for the methane aromatization reaction, the effect of zeolite acidity was investigated in the methane activation reaction to control the products selectivity. A boron containing zeolite was synthesized and the zeolite structure was investigated through the reaction. The active molybdenum species were characterized with surface and bulk techniques to find out the surface reaction with methane. In the end, a Mo_2C supported on boron containing zeolite catalyst was found to be an effective catalyst for the methane coupling reaction to form ethylene.

Chapter 6 summarizes the main findings of this thesis in the two topics of biomass upgrading and methane utilization. In addition, new research directions are proposed for the future studies in the following two aspects: 1) a more detailed surface reaction study to extend the application to other molecules with the same functional groups; 2) scale up study of the current process which includes the catalyst long-term stability/regeneration and the optimization of the products yield.

REFERENCES

[1] U.S.E.I. Administration, Annual Energy Outlook, in, 2017, pp. 6.

[2] A. Corma, S. Iborra, A. Velty, Chemical routes for the transformation of biomass into chemicals, Chemical Reviews, 107 (2007) 2411-2502.

[3] U. Bossel, B. Eliasson, Energy and the hydrogen economy, in, Oberrohrdorf, Switzerland, 2003, pp. 5.

[4] J.H. Lunsford, Catalytic conversion of methane to more useful chemicals and fuels: a challenge for the 21st century, Catalysis Today, 63 (2000) 165-174.

[5] A.S. Mamman, J.M. Lee, Y.C. Kim, I.T. Hwang, N.J. Park, Y.K. Hwang, J.S. Chang, J.S. Hwang, Furfural: Hemicellulose/xylosederived biochemical, Biofuels Bioproducts & Biorefining-Biofpr, 2 (2008) 438-454.

[6] E. Antolini, Catalysts for direct ethanol fuel cells, Journal of Power Sources, 170 (2007) 1-12.

[7] B.H. Wojcik, CATALYTIC HYDROGENATION OF FURAN COMPOUNDS, Industrial and Engineering Chemistry, 40 (1948) 210-216.

[8] J.N. Chheda, G.W. Huber, J.A. Dumesic, Liquid-phase catalytic processing of biomass-derived oxygenated hydrocarbons to fuels and chemicals, Angewandte Chemie-International Edition, 46 (2007) 7164-7183.

[9] H.Y. Zheng, Y.L. Zhu, B.T. Teng, Z.Q. Bai, C.H. Zhang, H.W. Xiang, Y.W. Li, Towards understanding the reaction pathway in vapour phase hydrogenation of furfural to 2-methylfuran, Journal of Molecular Catalysis a-Chemical, 246 (2006) 18-23.

[10] U.S.I.T. Commission, Furfuryl Alcohol from China, South Africa, and Thailand, U.S. International Trade Commission, 1994.

[11] Y. Izumi, Y. Tanaka, K. Urabe, SELECTIVE CATALYTIC-HYDROGENATION OF PROPARGYL ALCOHOL WITH HETEROPOLY ACID-MODIFIED PALLADIUM, Chemistry Letters, (1982) 679-682.

[12] H. Singh, M. Prasad, R.D. Srivastava, METAL SUPPORT INTERACTIONS IN THE PALLADIUM-CATALYZED DECOMPOSITION OF FURFURAL TO FURAN, Journal of Chemical Technology and Biotechnology, 30 (1980) 293-296.

[13] S.H. Pang, J.W. Medlin, Adsorption and Reaction of Furfural and Furfuryl Alcohol on Pd(111): Unique Reaction Pathways for Multifunctional Reagents, Acs Catalysis, 1 (2011) 1272-1283.

[14] S. Sitthisa, T. Sooknoi, Y. Ma, P.B. Balbuena, D.E. Resasco, Kinetics and mechanism of hydrogenation of furfural on Cu/SiO2 catalysts, Journal of Catalysis, 277 (2011) 1-13.

[15] S. Sitthisa, P. Trung, T. Prasomsri, T. Sooknoi, R.G. Mallinson, D.E. Resasco, Conversion of furfural and 2-methylpentanal on Pd/SiO2 and Pd-Cu/SiO2 catalysts, Journal of Catalysis, 280 (2011) 17-27.

[16] J. Kijenski, P. Winiarek, T. Paryjczak, A. Lewicki, A. Mikolajska, Platinum deposited on monolayer supports in selective hydrogenation of furfural to furfuryl alcohol, Applied Catalysis a-General, 233 (2002) 171-182.

[17] B.M. Nagaraja, V.S. Kumar, V. Shasikala, A.H. Padmasri, B. Sreedhar, B.D. Raju, K.S.R. Rao, A highly efficient Cu/MgO catalyst for vapour phase hydrogenation of furfural to furfuryl alcohol, Catalysis Communications, 4 (2003) 287-293.

[18] R.B. Levy, M. Boudart, PLATINUM-LIKE BEHAVIOR OF TUNGSTEN CARBIDE IN SURFACE CATALYSIS, Science, 181 (1973) 547-549.

[19] H.H. Hwu, J.G.G. Chen, Surface chemistry of transition metal carbides, Chemical Reviews, 105 (2005) 185-212.

[20] A.L. Stottlemyer, T.G. Kelly, Q.H. Meng, J.G.G. Chen, Reactions of oxygen-containing molecules on transition metal carbides: Surface science insight into potential applications in catalysis and electrocatalysis, Surface Science Reports, 67 (2012) 201-232.

[21] W.-S. Lee, Z. Wang, W. Zheng, D.G. Vlachos, A. Bhan, Vapor phase hydrodeoxygenation of furfural to 2-methylfuran on molybdenum carbide catalysts, Catalysis Science & Technology, 4 (2014) 2340-2352.

[22] L. Grazia, A. Lolli, F. Folco, Y. Zhang, S. Albonetti, F. Cavani, Gas-phase cascade upgrading of furfural to 2-methylfuran using methanol as a H-transfer reactant and MgO based catalysts, Catalysis Science & Technology, 6 (2016) 4418-4427.

[23] C.P. Jimenez-Gomez, J.A. Cecilia, R. Moreno-Tost, P. Maireles-Torres, Selective Production of 2-Methylfuran by Gas-Phase Hydrogenation of Furfural on Copper Incorporated by Complexation in Mesoporous Silica Catalysts, Chemsuschem, 10 (2017) 1448-1459.

[24] M.J. Gilkey, P. Panagiotopoulou, A.V. Mironenko, G.R. Jenness, D.G. Vlachos, B. Xu, Mechanistic Insights into Metal Lewis Acid-Mediated Catalytic Transfer Hydrogenation of Furfural to 2-Methylfuran, Acs Catalysis, 5 (2015) 3988-3994.

[25] D. Bezier, S. Park, M. Brookhart, Selective Reduction of Carboxylic Acids to Aldehydes Catalyzed by B(C6F5)(3), Organic Letters, 15 (2013) 496-499.

[26] W. Riemenschneider, Carboxylic Acids, Aliphatic, in: Ullmann's Encyclopedia of Industrial Chemistry, 2000.

[27] N. Murali, K. Srinivas, B.K. Ahring, Biochemical Production and Separation of Carboxylic

Acids for Biorefinery Applications, Fermentation, 3 (2017) 22.

[28] H. Benaissa, P.N. Davey, Y.Z. Khimyak, I.V. Kozhevnikov, Heteropoly compounds as catalysts for hydrogenation of propanoic acid, Journal of Catalysis, 253 (2008) 244-252.

[29] H. Bayahia, E.F. Kozhevnikova, I.V. Kozhevnikov, Ketonisation of carboxylic acids over Zn-Cr oxide in the gas phase, Applied Catalysis B-Environmental, 165 (2015) 253-259.

[30] D.S. Merel, D. Minh Loan Tran, S. Gaillard, P. Dupau, J.-L. Renaud, Iron-catalyzed reduction of carboxylic and carbonic acid derivatives, Coordination Chemistry Reviews, 288 (2015) 50-68.

[31] C.A. Gaertner, J.C. Serrano-Ruiz, D.J. Braden, J.A. Dumesic, Ketonization Reactions of Carboxylic Acids and Esters over Ceria-Zirconia as Biomass-Upgrading Processes, Industrial & Engineering Chemistry Research, 49 (2010) 6027-6033.

[32] J.A. Miller, J.A. Nelson, M.P. Byrne, A HIGHLY CATALYTIC AND SELECTIVE CONVERSION OF CARBOXYLIC-ACIDS TO 1-ALKENES OF ONE LESS CARBON-ATOM, Journal of Organic Chemistry, 58 (1993) 18-20.

[33] T. Yokoyama, N. Fujita, Hydrogenation of aliphatic carboxylic acids to corresponding aldehydes over Cr2O3-based catalysts, Applied Catalysis a-General, 276 (2004) 179-185.

[34] R. Pestman, R.M. Koster, J.A.Z. Pieterse, V. Ponec, Reactions of carboxylic acids on oxides .1. Selective hydrogenation of acetic acid to acetaldehyde, Journal of Catalysis, 168 (1997) 255-264.

[35] L. Fabre, P. Gallezot, A. Perrard, Catalytic hydrogenation of arabinonic acid and lactones to arabitol, Journal of Catalysis, 208 (2002) 247-254.

[36] H.G. Manyar, C. Paun, R. Pilus, D.W. Rooney, J.M. Thompson, C. Hardacre, Highly selective and efficient hydrogenation of carboxylic acids to alcohols using titania supported Pt catalysts, Chemical Communications, 46 (2010) 6279-6281.

[37] R.D. Cortright, M. Sanchez-Castillo, J.A. Dumesic, Conversion of biomass to 1,2-propanediol by selective catalytic hydrogenation of lactic acid over silica-supported copper, Applied Catalysis B-Environmental, 39 (2002) 353-359.

[38] K.S. Kim, M.A. Barteau, STRUCTURE AND COMPOSITION REQUIREMENTS FOR DEOXYGENATION, DEHYDRATION, AND KETONIZATION REACTIONS OF CARBOXYLIC-ACIDS ON TIO2(001) SINGLE-CRYSTAL SURFACES, Journal of Catalysis, 125 (1990) 353-375.

[39] A.T. Ashcroft, A.K. Cheetham, M.L.H. Green, P.D.F. Vernon, PARTIAL OXIDATION OF METHANE TO SYNTHESIS GAS-USING CARBON-DIOXIDE, Nature, 352 (1991) 225-226.

[40] T.V. Choudhary, E. Aksoylu, D.W. Goodman, Nonoxidative activation of methane, Catalysis Reviews-Science and Engineering, 45 (2003) 151-203.

[41] J.R. Rostrup-Nielsen, Syngas in perspective, Catalysis Today, 71 (2002) 243-247.

[42] M.E. Dry, The Fischer-Tropsch process: 1950-2000, Catalysis Today, 71 (2002) 227-241.

[43] J.G. Xu, G.F. Froment, METHANE STEAM REFORMING, METHANATION AND WATER-GAS SHIFT .1. INTRINSIC KINETICS, Aiche Journal, 35 (1989) 88-96.

[44] D.L. Trimm, Catalysts for the control of coking during steam reforming, Catalysis Today, 49 (1999) 3-10.

[45] E. Iglesia, Design, synthesis, and use of cobalt-based Fischer-Tropsch synthesis catalysts, Applied Catalysis a-General, 161 (1997) 59-78.

[46] R.H. Crabtree, ASPECTS OF METHANE CHEMISTRY, Chemical Reviews, 95 (1995) 987-1007.

[47] G.E. Keller, M.M. Bhasin, SYNTHESIS OF ETHYLENE VIA OXIDATIVE COUPLING OF METHANE .1. DETERMINATION OF ACTIVE CATALYSTS, Journal of Catalysis, 73 (1982) 9-19.

[48] L.S. Wang, L.X. Tao, M.S. Xie, G.F. Xu, J.S. Huang, Y.D. Xu, DEHYDROGENATION AND AROMATIZATION OF METHANE UNDER NONOXIDIZING CONDITIONS, Catalysis Letters, 21 (1993) 35-41.

[49] B.M. Weckhuysen, D.J. Wang, M.P. Rosynek, J.H. Lunsford, Conversion of methane to benzene over transition metal ion ZSM-5 zeolites - I. Catalytic characterization, Journal of Catalysis, 175 (1998) 338-346.

[50] R.W. Borry, Y.H. Kim, A. Huffsmith, J.A. Reimer, E. Iglesia, Structure and density of Mo and acid sites in Mo-exchanged H-ZSM5 catalysts for nonoxidative methane conversion, Journal of Physical Chemistry B, 103 (1999) 5787-5796.

[51] W.P. Ding, S.Z. Li, G.D. Meitzner, E. Iglesia, Methane conversion to aromatics on Mo/H-ZSM5: Structure of molybdenum species in working catalysts, Journal of Physical Chemistry B, 105 (2001) 506-513.

[52] Y.D. Xu, S.T. Liu, L.S. Wang, M.S. Xie, X.X. Guo, METHANE ACTIVATION WITHOUT USING OXIDANTS OVER MO/HZSM-5 ZEOLITE CATALYSTS, Catalysis Letters, 30 (1995) 135-149.

[53] F. Solymosi, J. Cserenyi, A. Szoke, T. Bansagi, A. Oszko, Aromatization of methane over supported and unsupported Mo-based catalysts, Journal of Catalysis, 165 (1997) 150-161.

[54] D.J. Wang, J.H. Lunsford, M.P. Rosynek, Characterization of a Mo/ZSM-5 catalyst for the conversion of methane to benzene, Journal of Catalysis, 169 (1997) 347-358.

Chapter 2

EXPERIMENTAL: MATERIALS AND METHODS

This chapter provides background information on the catalytic materials and the experimental techniques used for materials characterization and data collection. This chapter starts with a summary of the micro- and mesoporous catalytic materials, and then describes the reactor setup and analytical tools that used for catalysts evaluation and kinetic studies. In the end of this chapter, the fundamentals of the characterization techniques are discussed, which provides information on the crystal structure, local geometry, surface area, porosity, reducibility, and elemental composition. The detailed materials synthesis procedures and the characterization experiments can be found in the subsequent chapters.

2.1 Micro- and Mesoporous Materials

Micro- and mesoporous materials are porous solids that containing pores with diameters less than 2 nm (microporous) and between 2 and 50 nm (mesoporous). The porosity enables the molecular level interaction both at the surfaces of the materials and throughout the bulk, which gives the materials large applications including ion exchange, separation, and catalysis. [1] In this work, zeolites and mesoporous silica were investigated as the catalyst or the support in the hydrogenation and methane coupling reactions.

2.1.1 Zeolites

Zeolites are microporous, crystalline tectoaluminosilicate that are comprised of TO_4 tetrahedra (T = tetrahedral atom, e.g. Si, Al, B, or P) with each apical oxygen atom shared by adjacent two tetrahedral.[2] The three-dimensional expansion of the TO_4 tetrahedra in different patterns forms the zeolite frameworks with rings, pores, and channels in molecular dimensions (Figure 2.1).

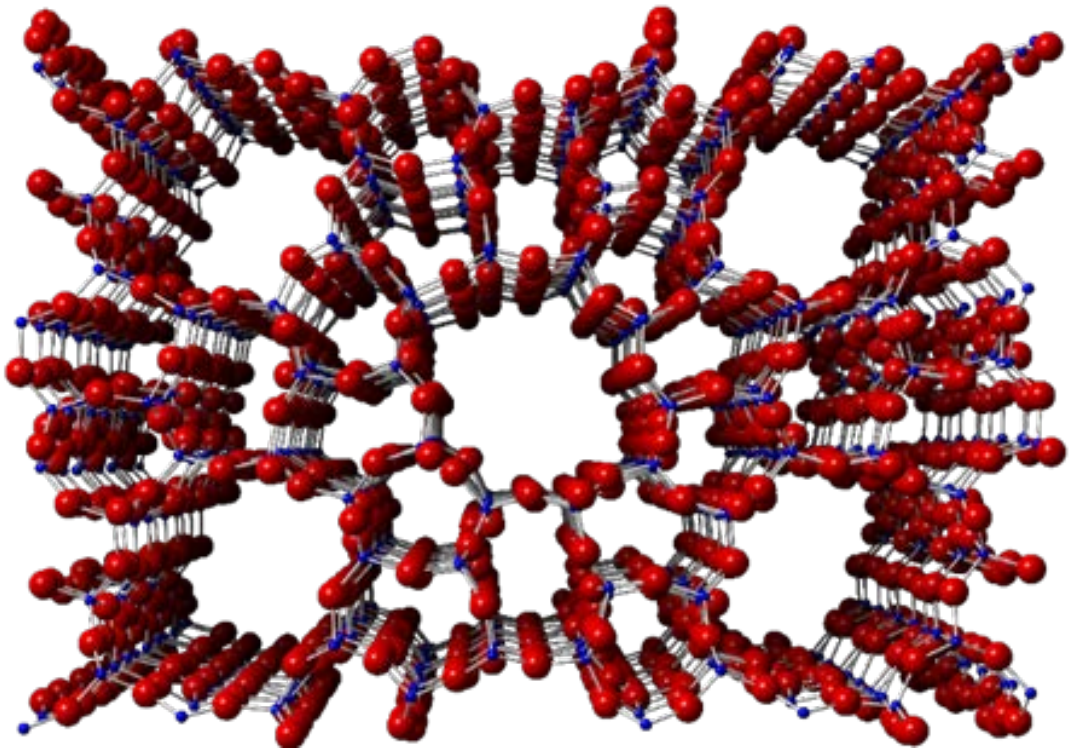

Figure 2.1 Framework structure of a MFI type zeolite (ZSM-5)

Such well-defined crystal structure with micropores makes it feasible for catalytic reactions while introducing the active sites can enhance its activity and selectivity.[3] One of the active sites that a Brønsted acid site is generated on the

zeolite surface when a Si^{IV} is substituted by a trivalent Al^{III} atom, while the negative charge created by this substitution is compensated by a proton. Thus, a Brønsted acid site can be viewed as a bridged hydroxyl group between silicon and aluminum atoms (Si-OH-Al), which gives rise to strong surface acidity.

2.1.2 Supported Catalysts from Wetness Impregnation

Wetness impregnation method is very commonly used in the synthesis of heterogeneous catalysts. Typically a metal precursor is firstly dissolved in a solvent such as DI water. Then the catalyst support is added into the solution. The mixture is dried at certain temperature and will be calcined to fully oxide the precursor to metal oxide. Before reaction, the catalyst usually needs to be treated either to reduce the metal or make other type of metal compound. The following figure presents the wetness impregnation process with Mo_2C/ZSM-5 as an example (Figure 2.2).

Figure 2.2 Synthesis of Mo2C/ZSM-5 through wetness impregnation method

2.2 Flow-reactor for Catalysts Evaluation and Kinetic Studies

Flow reactors are used for the catalysts evaluation and kinetic studies in this thesis. An example of the reactor system design is presented in Figure 2.3, which is designed for furfural hydrodeoxygenation. Multiple gases can be fed into the vertical positioned flow reactor, while the catalyst can be loaded between two layers of quartz wools inside the reactor tube. Liquid reactant flow can be introduced into the reactor from the top and the liquid will be vaporized with all the lines heated. The reactor is heated by a furnace and all the heated part are controlled at the same temperature in order to ensure an isothermal condition. Finally, the products are collected and analyzed with an online GC.

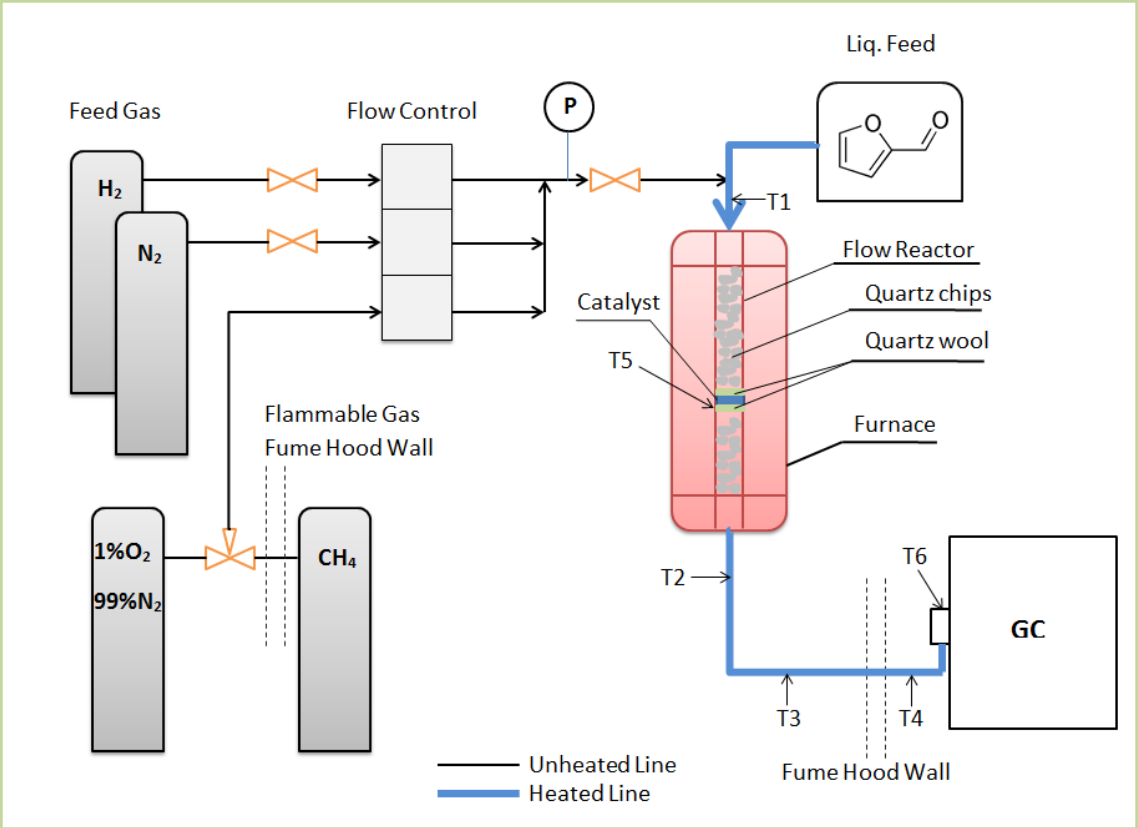

Figure 2.3 Illustration of a flow reactor setup for furfural hydrodeoxygenation

2.3 Characterization Techniques and Spectroscopies

Multiple materials characterization techniques have been applied in this thesis and the fundamental information of the characterization methods are briefly introduced in the next session.

2.3.1 Powder X-ray Diffraction (XRD)

X-ray diffraction (XRD) is an analytical technique to determine the structure of crystalline materials. To be specifically, it is widely used to identify the crystalline phases, as well as provide information on the unit cell dimensions. An X-ray diffractometer is composed of an X-ray tube, a sample holder, and a detector. An X-

ray tube can produce a monochromatic X-ray beam and the most common one in laboratory uses a copper anode with a Kα wavelength of 1.5418 Å. For the measurement of loose powder sample, typically the powder is loaded onto a stationary sample container while the X-ray tube and the detector are rotated simultaneously around it. During the XRD measurement, the X-ray is shined onto the sample at an incident angle θ, while the detector is positioned at the opposite end of the equipment at the same angle θ above the sample. The incident beam angle increases slowly as the measurement proceeds and the X-ray intensity is measured at the detector as a function of the angle θ (Figure 2.4).

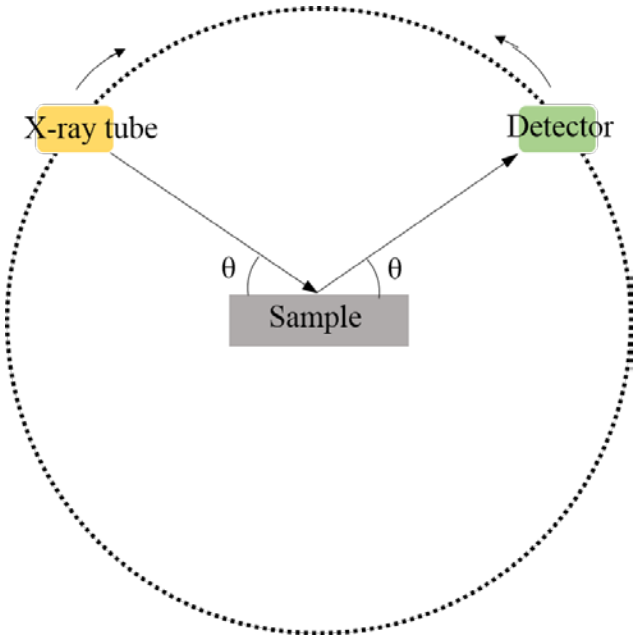

Figure 2.4 Illustration of an x-ray diffractometer setup

When the X-ray scattering occurs, the scattered waves cancel one another in most directions due to the destructive interference, while they add up constructively in

some specific directions. These directions with an incident angle θ is described by Bragg's law (Eqn 2.1):

$$2d\sin\theta = n\lambda \qquad \text{Eqn. 2.1}$$

where *d* is the distance between the diffracting planes, θ is the diffraction angle, *n* is a positive integer, λ is the wavelength of the incident X-ray beam. In this dissertation, the XRD patterns were compared to the reference spectra from International Zeolite Association (IZA)[4] and Inorganic Crystal Structure Database (ICSD)[5].

2.3.2 X-ray Absorption Spectroscopy (XAS)

X-ray absorption spectroscopy (XAS) is used to determine the local geometric and electronic structures of materials. X-ray beam that are accelerated by a synchrotron can have sufficient energy to eject a core electron from an atom. The electron gets excited and emits when the incoming beam energy reaches the core-electron binding energy. When the beamline energy is scanned through the binding energy, there is an energy absorption increase that give rise to an absorption edge when the absorption coefficient is plotted as a function of the scanning energy (Figure 2.5).

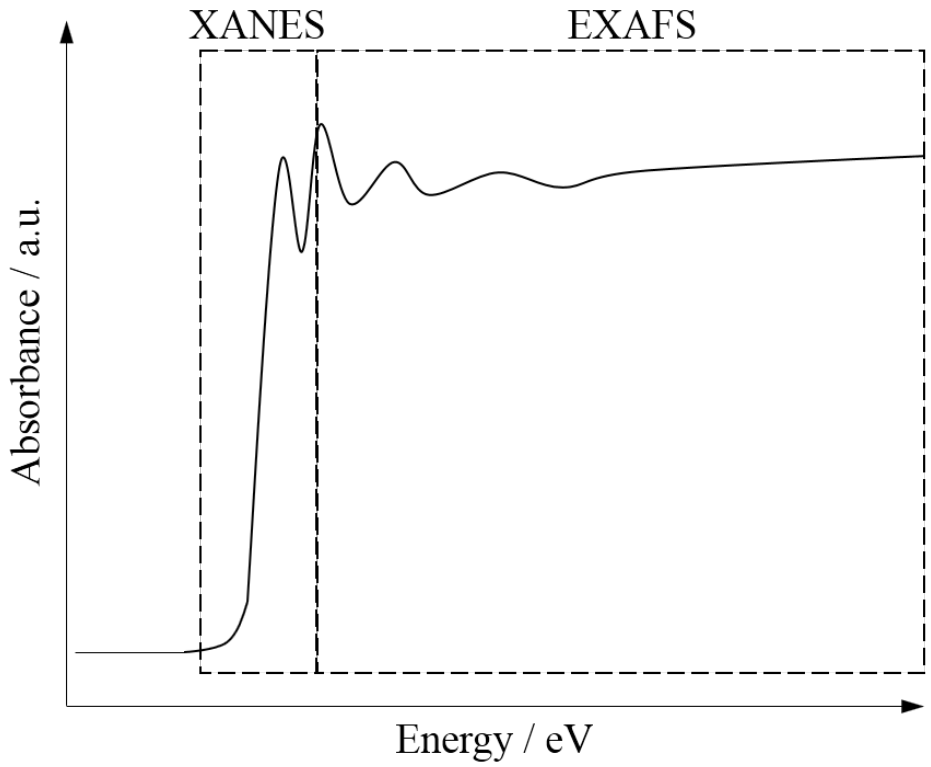

Figure 2.5 Schematic illustration of an X-ray absorption spectrum

There are three regions in terms of the energy: 1) pre-edge region, where the energy of the incident x-ray beam ranges from 150 eV below to the edge; 2) edge, where the absorption increases dramatically; 3) post edge region, where the energy starts from the absorption edge to several hundreds eV above. According to the energy region, the XAS spectrum can be analyzed in two regions: X-ray absorption near edge spectroscopy (XANES) and extended x-ray absorption fine structure (EXAFS). The XANES zone includes the absorption edge with the energy of incident x-ray beam ranging from 50 eV below edge to 50 eV above edge. The EXAFS spectrum starts approximately from 50 eV and ends up to 1000 eV above the edge. Figure 2.5 presents

a typical XAS spectrum including the XANES and EXAFS. In general, XANES spectra can be used to measure the average oxidation state of a compound by comparing the edge energy with the standards. EXAFS data can be analyzed for evaluating the local coordinate of a specific compound. The advantages of this technique are to measure the spectra in-situ and each spectrum collection only takes several minutes.

The XAS experiments were carried out at the Advanced Photon Source (APS) at Argonne National Laboratory (ANL) with the beamline facility 10 B, C.

2.3.3 Diffuse Reflectance UV-VIS Spectroscopy

UV-VIS spectroscopy is a widely used technique to measure absorption or reflectance within the ultraviolet and visible light regions. The chemical bonds can absorb the energy of ultraviolet or visible of certain wavelength and get excited to the higher energy stage. By scanning the wavelength of the light, the transmitted or reflected light can be collected and measured. A signal is generated when there is a characteristic absorption for a specific compound. In this thesis, the UV-VIS spectra for the solid phase catalysts were collected with the diffuse reflectance methods, while the in-situ experiments were carried out with a home designed cell (Figure 2.6).

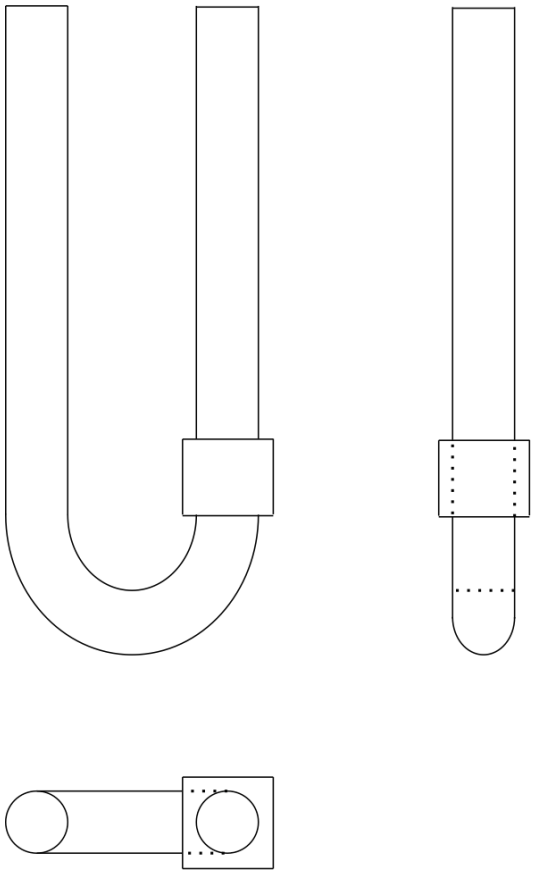

Figure 2.6 Home designed in-situ UV-VIS cell

The cell is assembled with a regular U-shaped tube and a squared tube inserted in the lower right position. The treatment gases can be introduced from the right side of the cell, while the whole cell can be heated with a programmed temperature controller. The catalyst powders can be loaded into the cube to reflect the in-shooting light. During the spectra measurement, the cell needs to be cooled down to room temperature with a flow of inert gas.

The UV-VIS studies were performed with a Jasco-V550 instrument.

2.3.4 Diffuse Reflectance Infrared Fourier Transform Spectroscopy (DRIFTS)

FT-IR spectroscopy can provide information on the molecular structure by measuring the dipole moment change of the vibration. For this reason, a symmetrical vibration from a non-pole molecule cannot be detected in FT-IR. Practically, FT-IR is widely used for organic compounds such as hydrocarbons and inorganic gases like CO and NO_x.

In this thesis the IR spectra were collected with the DRIFTS technique with an in-situ DRIFTS cell (Figure 2.7). When incident infrared beam is focused onto the surface of the sample, the beam interacts with the particles in the following ways: the beam can be reflected of the top surface; the light can undergo multiple reflections off the sample surface. The reflected light is collected and analyzed with a liquid nitrogen cooled mercury cadmium telluride (MCT) type detector. The cell body is made of stainless steel with a sample holder in the center of it. The whole cell is heated by a heating cartridge located in the back of the cell, while during the measurement, multiple treatment gases can be fed into the cell and flow through the sample.

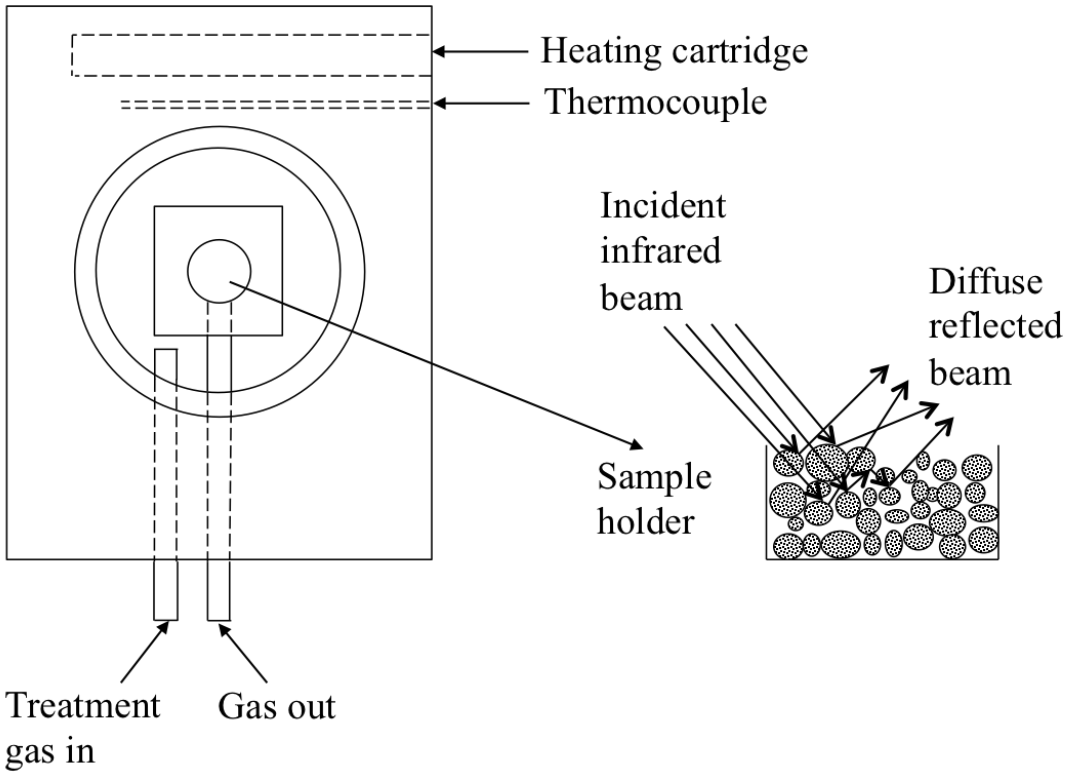

Figure 2.7 In-situ DRIFT cell with illustration of infrared beam diffuse reflectance

2.3.5 Transition Electron Microscopy (TEM)

Transition electron microscopy is an imaging method that allows the surface morphology analysis with a nanometer-scale resolution. The images are formed when a beam of electrons is transmitted through a sample specimen and interacts with the sample. The TEM images were taken in the Keck Center for Advanced Microscopy and Microanalysis in University of Delaware and I'd like to acknowledge Dr. Weiqing Zheng for his work of taking TEM image of the Mo_2C/[B]ZSM-5.

2.3.6 Inductively Coupled Plasma Mass Spectrometry (ICP-MS) Analysis

Inductively coupled plasma-mass spectrometry is the method to analyze elements concentrations in a sample with high sensitivity. The process is conducted

with the samples being ionized with the inductively coupled plasma and then separation and quantification with a mass spectroscopy attached to it. This technique has a broad application including the area of chemistry, materials science, and medical applications. In this thesis, the boron containing zeolites were analyzed with ICP-MS for the boron concentration in the sample. I’d like to acknowledge Edward Schreiner for the help in this part of work.

REFERENCES

[1] M.E. Davis, Ordered porous materials for emerging applications, Nature, 417 (2002) 813-821.

[2] M.E. Davis, R.F. Lobo, ZEOLITE AND MOLECULAR-SIEVE SYNTHESIS, Chemistry of Materials, 4 (1992) 756-768.

[3] A. Corma, State of the art and future challenges of zeolites as catalysts, Journal of Catalysis, 216 (2003) 298-312.

[4] M.M.J. Treacy, J.B. Higgins, Collection of Simulated XRD Powder Patterns for Zeolites, Collection of Simulated Xrd Powder Patterns for Zeolites, (2007) 1-474.

[5] G. Bergerhoff, I.D. Brown, Inorganic Crystal Structure Database (ICSD), in, pp. https://www.fiz-karlsruhe.de/icsd.html.

[6] P.J. Chupas, K.W. Chapman, C. Kurtz, J.C. Hanson, P.L. Lee, C.P. Grey, A versatile sample-environment cell for non-ambient X-ray scattering experiments, Journal of Applied Crystallography, 41 (2008) 822-824.

Chapter 3

IRON-PROMOTION FOR FURFURAL HYDRODEOXYGENATION WITH SILICA SUPPORTED COPPER CATALYST

3.1 Introduction

Selective hydrogenation of biomass-derived compounds is often necessary for the valorization of compounds such as this form of renewable carbon is oxidized relative to the most important commodity organic chemicals such as ethylene, methanol, etc. A catalyst that is inexpensive, stable and selective is desired to accomplish such hydrogenations. As a derivative of lignocellulose,[1] furfural is a platform chemical that can be upgraded to a variety of valuable organic chemicals and biofuels.[2] Several cellulosic ethanol plants have been opened in the Midwest of the USA with 30-million gallon ethanol annual production capacity,[3] and since C5 sugar streams are not ideal for fermentation, these could be used instead for the preparation of furfural. The hydrodeoxygenation (HDO) of furfural is a promising process to remove 'excess' oxygen and increase energy density and stability. The product, 2-methylfuran, for example, is an excellent biofuel candidate or additive. The challenge of this process is the stable hydrogenation of the side carbonyl group only, leaving the furan ring untouched.

Copper-chromite is a well-known commercial catalyst that can selectively convert furfural to furfuryl alcohol (99% conversion and 96% selectivity).[4] However, due to concerns about the toxicity of chromite, many other Cu-based catalysts have been investigated including Cu/SiO_2,[5] Cu/SBA-15,[6] Cu/C,[7]

Cu/MgO,[8] Cu/ZnO,[9] Cu-Co/SBA-15[10] and Cu, Pd, Ni catalyst:[11] the observed selectivity of these Cu-based catalysts is geared mainly towards furfuryl alcohol. Other transition metal catalysts have been reported for the hydrogenation of furfural such as Au/Al_2O_3,[12] Mo_2C,[13] supported Pt,[14, 15] and Ru-based catalyst.[16-18]

Unsupported Cu-Fe catalysts haveshown51% selectivity to 2-methylfuran, according to Yan and Chen.[19] The catalyst was calcined at 1123 K and then was added directly into a batch reactor without any pre-reduction, where acidic centers in these Cu-Fe catalysts are claimed as the active sites for the dehydration of furfuryl alcohol to 2-methylfuran. Recently $FeCu/\gamma\text{-}Al_2O_3$ was reported to be an effective catalyst with 93% furfural conversion and 98% selectivity to furfuryl alcohol.[20] Manikandan and coworkers show that Fe and Cu are fully reduced to metal and bimetallic FeCu was formed at 673 K, as observed by in-situ X-ray powder diffraction (XRD) analyses. They also show that Fe was responsible for the high reactivity while the selectivity was driven by Cu. However, Lukes and Wilson reported that 80% of 2-methylfuran was obtained from furfuryl alcohol with metallic Fe-Cu (10:90 w/w) catalyst. The catalyst was synthesized using fine copper turnings and sintered iron powder (4-16 mesh). Prior reaction, it was activated by a calcination at 773 K followed by a reduction at 573 K in H_2. By not observing water formation at 573 K, they believe that the metal mixtures were fully reduced. They indicate that the hydrogenation performance of the catalyst was facilitated by the presence of unfilled 3d-electron levels of metallic copper.[21]

While all these Cu-Fe catalysts showed different properties in terms of the product selectivity, the role of Fe plays in the reaction network remains unclear.

Therefore it is of interest to discover the active phase of the catalyst and with this understanding, it can be learned that how to tune the product selectivity.

In this report iron promoted Cu/SiO_2 catalysts were investigated to understand the structure-property relations of this material for furfural selective hydrogenation. It is shown that addition of a small amount of iron Fe (0.15% w/w) increases copper dispersion and reaction rates, while keeping very high selectivity to furfuryl alcohol (~87%). Furthermore, catalysts pre-reduction at 543 K instead of 483 K leads to a remarkable change in selectivity. At the higher temperature, the Fe species are partially reduced (into Fe^{2+}) leading to the activation of a new reaction channel to rapidly hydrogenate furfuryl alcohol into 2-methylfuran. The reduced iron species catalyze furfuryl alcohol hydrogenation at much faster rates than furfural hydrogenation.

3.2 Experimental Section

3.2.1 Catalyst Preparation

The $Cu\text{-}Fe/SiO_2$ catalysts were prepared by wetness co-impregnation method at a liquid to solid ratio of 1 mL/g. First the $Cu(NO_3)_2{\cdot}xH_2O$ (99.999%, Sigma-Aldrich) and $Fe(NO_3)_3{\cdot}9H_2O$ (99.999%, Sigma-Aldrich) were dissolved in DI water and silica gel (high-purity grade, Sigma-Aldrich) was then added into the aqueous solution. After drying at the room temperature for 12 hours, the mixture was transferred to an oven at 393 K for 12 hrs. The dried catalyst was then calcined at 773 K for 5 hours, with a ramping rate of 2 K/min. Finally, the catalyst was reduced under 50 sccm H_2 for 4 hours. The reduction temperature was determined by temperature programmed reduction (TPR) experiments. The copper loading is 1% wt. in all the

catalysts and the atomic ratios of Cu/Fe are 1 : 0, 9 : 1 and 7 : 1. Also 1% wt. Fe/SiO_2 was prepared using the same procedure for comparison purpose.

3.2.2 Morphology Characterization

XRD analysis was performed using Bruker D8 x-ray powder diffractometer with monochromatic Cu Kα1 line (λ=1.540 Å). SEM images were obtained by a Zeiss Cross Beam Auriga 60 FIB-SEM.N_2 adsorption experiments were performed with 3Flex surface characterization analyzer. BET Surfaces were calculated using the MicroActive for 3Flex software.

3.2.3 Temperature Programmed Reduction (TPR)

The reducibility of Cu-Fe/SiO_2 catalysts were determined by hydrogen temperature programmed reduction. In each measurement, about 100 mg of catalyst sample was loaded in a U-shaped quartz tube reactor. The catalyst was firstly heated to 773 K at 10 K/min under a 20% O_2/Ar flow of 25 sccm and held for 1 hour. After cooling down in Ar flow to room temperature, the catalyst sample was then heated to 1123 K at 10 K /min under a 20% H_2/Ar flow of 25 sccm. The TPR experiments were performed using an Altamira AMI-200.

3.2.4 N_2O Pre-oxidized TPR

The N_2O pre-oxidized TPR was carried out in the same setup as section 2.2. About 100 mg of material was placed in the U-shaped quartz tube reactor. Cu/SiO_2 was first reduced at 483 K in 20% H_2/Ar flow of 25 sccm. For comparison, Cu-Fe/SiO_2 was reduced at 483 K or 543 K. After the reduction, the material was cooled down to 323 K in Ar flow followed by N_2O oxidation to convert Cu metal to Cu(I) species. The N_2O oxidation was finished after holding at 323 K for 1 hour with a 10%

N_2O/Ar flow of 20 sccm. Finally, a full TPR was performed under a 20%H_2/Ar flow of 25 sccm until 1123 K at 10 K/min.

3.2.5 *In situ* Diffused Reflectance UV-VIS

Diffused reflectance UV-VIS study was carried out using a flow cell and a Jasco V550 UV-VIS spectroscopy. The *in situ* flow cell is made of U-shaped quartz round tube with a UV window made of square quartz tube (Quartz Plus, Inc.). Typically, 100 mg of the catalyst sample was loaded into the flow cell at the window. Other auxiliary systems (a heating system and gas flow control system) are included to perform the in-situ UV-VIS study. All the spectra were taken at room temperature with inert gas flowing through the sample bed.

3.2.6 *In situ* Fourier Transform Infrared (FT-IR) Characterization

The FT-IR measurements were performed using an *in situ* diffused reflectance infrared Fourier transform (DRIFT) cell with ZnSe windows (15 x 2 mm, Harrick Sci.). The IR cell consists of a cell body, sample holder and aluminum heating block. About 50 mg of the catalyst sample was required to load into the sample holder as a pellet. Proper gases could be fed through the sample by mass flow controllers (Brooks 5850E series). IR spectra were collected using a Fourier transform infrared spectrometer (Nicolet Nexus 470). The IR spectral data were analyzed by OMNIC software. The catalyst sample was pre-treated with He at 573 K (5 K/min ramping rate) for 4 hours to remove moisture and other surface contaminates. After cooling down to room temperature, the sample was then reduced at 483 K or 543 K (2 K/min ramping rate) under 20% H_2/He of 50 sccm for 2 hours. After cooling down to room

temperature in He flow, the catalyst was treated with 2% NO/He of 10 sccm. IR spectra were collected every 3 min once the NO/He flow started.

3.2.7 Catalyst Evaluation

The reactivity of the catalysts was tested in a flow reactor made of 9/16'' ID stainless steel tubing. Typically, 50 mg catalyst was loaded in the middle of reactor between two quartz wool layers. Fresh distilled furfural (99%, Sigma-Aldrich) or furfuryl alcohol (98%, Sigma-Aldrich) was fed into the reactor using a pump (NE-1000, New Era Pump System Inc.) and syringe (Hamilton) from the top of the tubing along with the reduction gas flow. The reactor was heated using a furnace and all the gas lines were wrapped with heating tapes and heated to the same temperature as the reactor to ensure an isothermal reaction system. All the products were collected and analyzed with an online gas chromatography (GC 2014, Shimadzu) that is equipped with an HP-INNOWax capillary column.

3.3 Results and Discussion

3.3.1 Materials Characterization

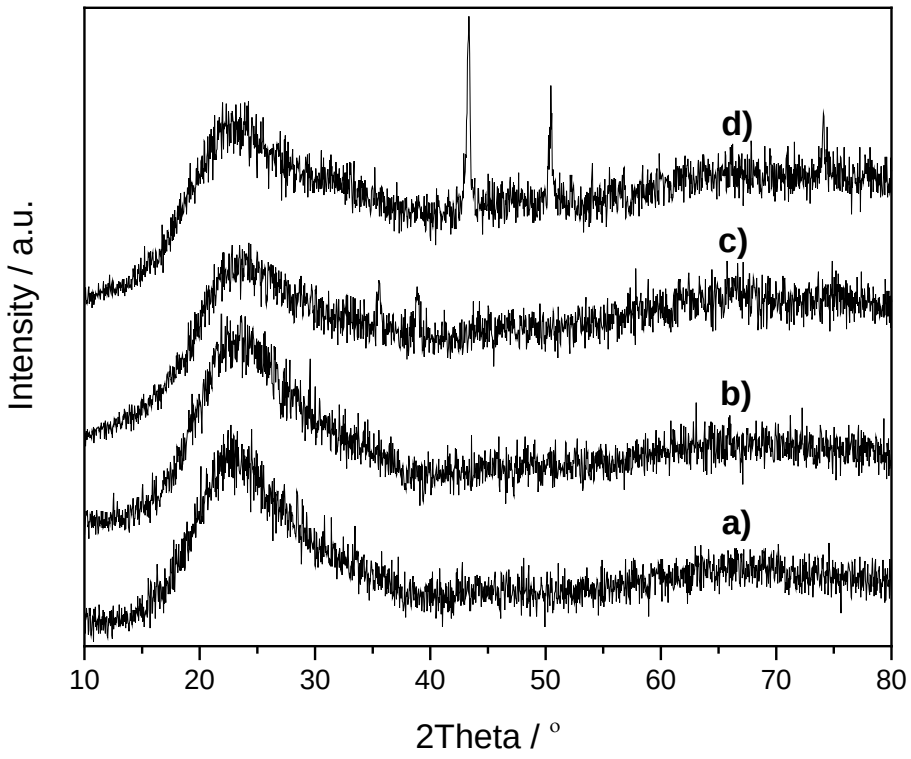

Figure 3.1 XRD patterns of Cu-Fe/SiO_2. a) 1% Cu-Fe/SiO_2 calcined@773 K, b) 1% Cu-Fe/SiO_2reduced@543 K, c) 2% Cu-Fe/SiO_2calcined@773 K, d) 2% Cu-Fe/SiO_2 reduced@543 K.

The XRD patterns of Cu-Fe/SiO_2 samples show predominantly the scattering of the amorphous silica support (Figure 3.1a and 3.1b). When the Cu loading is increased to 2% at the same Cu-Fe atomic ratio (7:1), two peaks at 35.8° and 38.9° 2Theta are observed on the calcined sample (Figure 3.1c). These peaks can be assigned to $CuFe_2O_4$ (JCPDS No. 25-0283) and CuO (JCPDS No. 80-0076) formed

during calcination.[22] When the 2% Cu-Fe/SiO_2sample is reduced in hydrogen, three new peaks, assigned to metallic Cu, are observed at 43.3°, 50.4°, and 74.1°. It can be inferred that initially Fe reacts with Cu to form $CuFe_2O_4$ spinel during the calcination of the co-impregnated sample. This is observed clearly for the 2% Cu-Fe/SiO_2 sample. In the 1% Cu-Fe sample there is no indication of these phases in the diffractograms either because the amount of spinel and CuO formed are too small to be detected, or because at these concentrations the interaction with the support prevents further reaction between Cu and Fe.

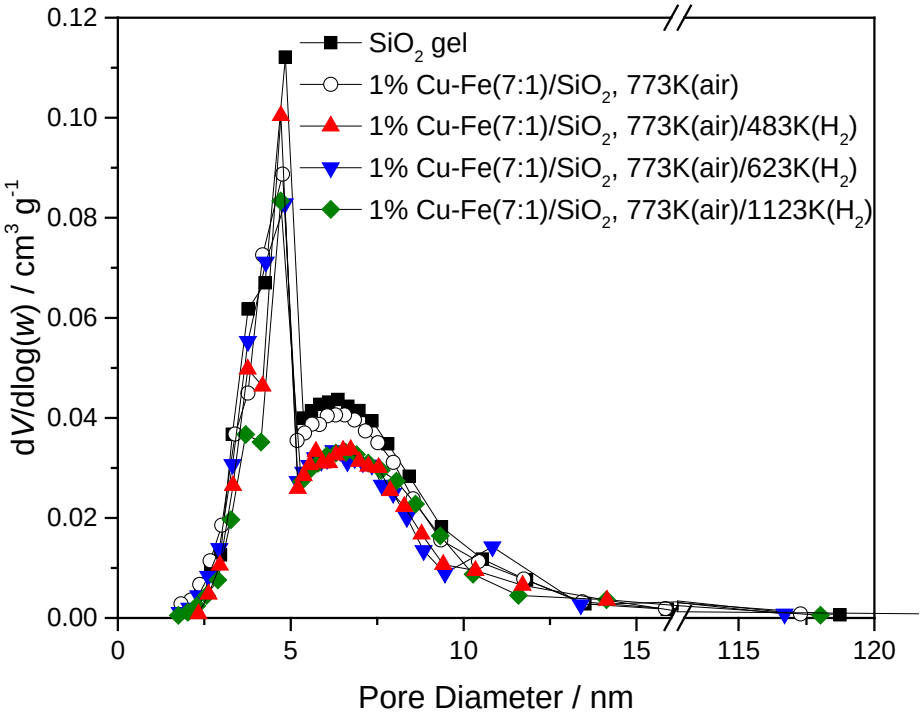

Figure 3.2 BJH pore size distribution of Cu-Fe/SiO_2 catalysts.

Table 3.1 BET surface area of Cu-Fe/SiO_2 catalysts

Catalysts& treatment methods	BET surface area (m^2/g)
SiO_2 gel (support)	480
1% Cu-Fe (7:1)/SiO_2, calcined@773K	492
1% Cu-Fe (7:1)/SiO_2, calcined@773 K, then reduced to 483 K using TPR	462
1% Cu-Fe (7:1)/SiO_2, calcined@773 K, then reduced to 623 K using TPR	471
1% Cu-Fe (7:1)/SiO_2, calcined@773 K, then reduced to 1123 K using TPR	326

The BJH analysis of the Cu-Fe/SiO_2 catalysts (Figure 3.2) shows a bimodal pore size distribution. A fraction of the pores have a narrow distribution centered around 4 nm (d_{TSE}=4.6 nm) and there is also another broader pore-size distribution centered around 6 nm. The N_2 adsorption isotherms indicate that the support has a BET surface area of 480 m^2/g (Table 3.1). This area increases to 492 m^2/g for the impregnated and calcined samples, and then decreases by 6% to 462 m^2/g after reduction at 483 K. If the reduction temperature is increased to 1123 K, the BET surface area decreases to 326 m^2/g. Thus, a suitable reduction temperature is necessary to achieve a balance between reduction of the metal precursors and catalyst activity.

3.3.2 Study on the Reducibility of the Catalyst

The reducibility of the Cu-Fe/SiO_2 catalysts was investigated using temperature-programmed reduction (TPR) in 20% H_2/Ar. Figure 3.3 displays the TPR traces of four catalysts showing that the reduction of 1% Cu/SiO_2 is complete at approximately 483 K. A shift in the reduction temperature of Cu is observed upon the addition of small amounts of Fe (0-0.15% w/w). The shift may be due to a better

dispersion of Cu onto the SiO_2 surface with the co-impregnated iron and reveals a direct interaction of the iron with the copper on the catalyst surface. This interaction is expected due to the formation of $CuFe_2O_4$ as noted above. Note too that in the reduction profile of the iron-containing samples there is a shoulder in the low-temperature side of the peak that is assigned to the reduction of CuO to Cu_2O.[23]

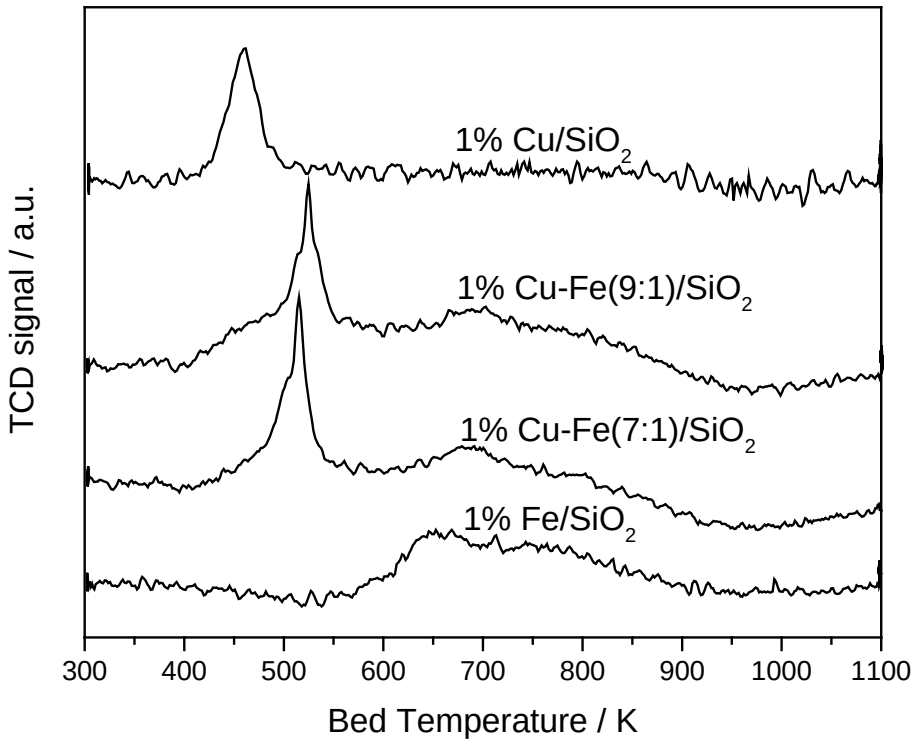

Figure 3.3 Temperature Programmed Reduction of Cu-Fe/SiO_2 catalysts

Silica supported iron oxide is not reducible to metallic iron using only H_2 as the reducing agent.[24] As shown in Figure 3.3, 1% Fe/SiO_2 does not display any indication of a reduction process until the sample temperature is higher than 573 K.

However, in the presence of Cu, the reduction of iron (III) is possible at lower temperature, as has been observed by others.[23-25] It is likely that upon the formation of Cu metal nanoparticles, H_2 dissociates on the Cu particles reaching the iron by spillover facilitating in this way the reduction of iron oxide.

3.3.3 Quantification of Accessible Copper Sites

The number of accessible Cu sites of the Cu-Fe/SiO_2 catalyst was determined by titration of a N_2O pre-oxidized sample using TPR.[26, 27] The accessible Cu sites are oxidized to Cu(I) oxide using N_2O, and then TPR is used to quantify the amount of oxygen chemisorbed on the pre-oxidized sample by integrating the water peak observed after reduction of the surface Cu_2O. In Table 3.2 is observed that the addition of Fe increases the number of accessible Cu sites, that is, iron increases the dispersion of Cu. In Figure 3.4 the reduction of Cu starts at about 400 K and is completed at temperature below 500 K (first reduction peak). However, reduction of Fe/SiO_2 does not start until the temperature is above 500 K. In the trace of Cu-Fe (7:1)/SiO_2 reduced at 483 K, a broad reduction peak from 500 K to 700 K is clearly visible; this feature, however, is not observed for the catalyst reduced at 543 K.

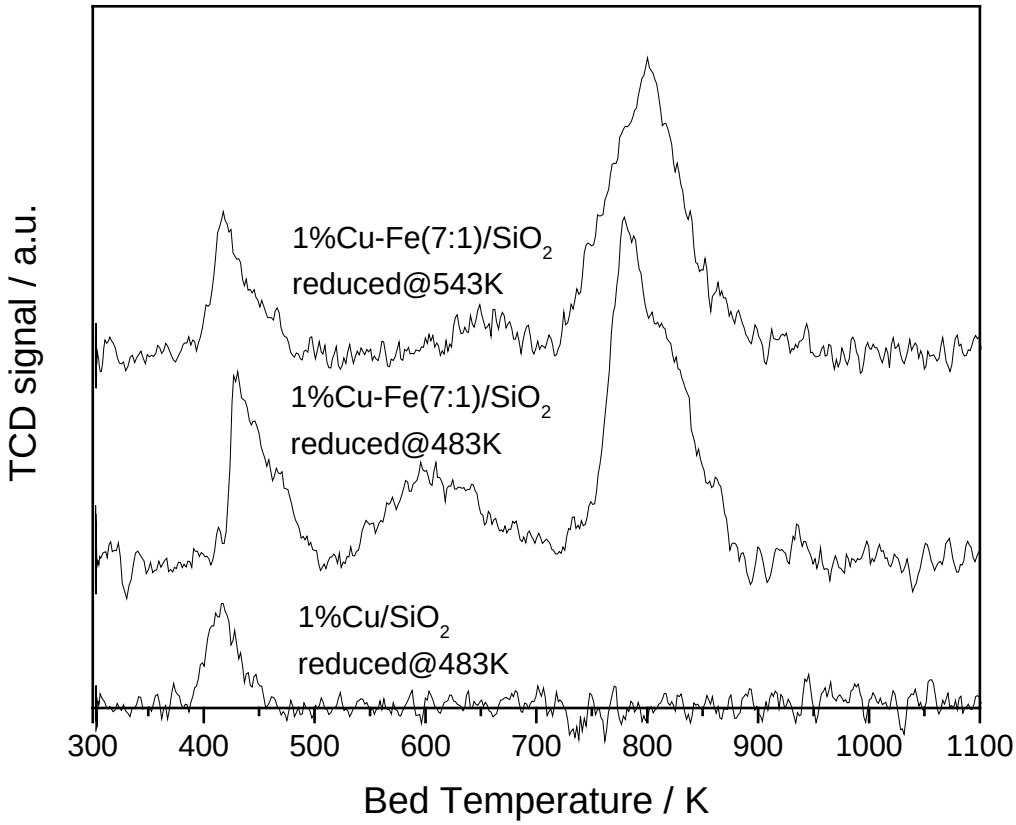

Figure 3.4 TPR of N_2O pre-oxidized Cu/SiO_2 and $Cu\text{-}Fe/SiO_2$ catalysts

Table 3.2 Active Cu sites in Cu/SiO_2 and $Cu\text{-}Fe\ (7:1)/SiO_2$

Catalysts	Weight (mg)	reduction temperature (K)	dispersion	S_{Cu} (m^2/g_{cat})	average Cu particle size (nm)
Cu/SiO_2	87	483	0.20	1.4	4.0
$Cu\text{-}Fe(7:1)/SiO_2$	133	483	0.27	1.9	3.0
$Cu\text{-}Fe(7:1)/SiO_2$	113	543	0.26	1.8	3.1

3.3.4 In-situ UV-VIS Study

In-situ diffuse reflectance UV-VIS spectroscopy was used to follow the oxidation state of the various components of the catalysts at different points during catalyst preparation (Figure 3.5). The catalyst was first calcined at 773 K for 4 hours and was then reduced at 543K in H_2 flow (20 sccm for 2 hours); the UV-VIS spectra were collected in He flow (~298 K) after reduction. The sample calcined at 773 K (1% Cu-Fe(7:1)/SiO_2) has an absorption feature at 740nm, which is consistent with the presence of small CuO particles (the sample had a light-brownish color). The absorption was blue shifted with respect the bulk CuO (~ 860 nm) as a result of particle size effects.[28] After reduction at 543 K, a different absorption peak with a maximum at 555nmis observed; this peak is assigned to the plasmonic absorption of the metallic copper particles.[28] The UV-VIS experiments indicate that copper was reduced from CuO to small metallic copper particles, while iron-related absorption peaks are not observed due to the low iron concentration.

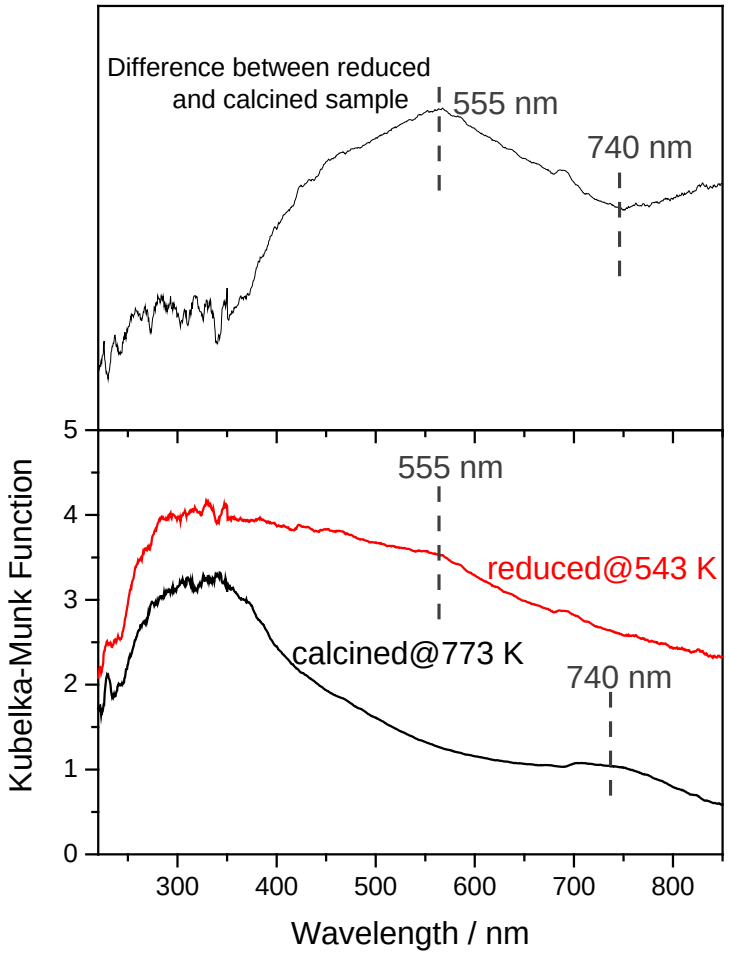

Figure 3.5 UV-VIS spectra of 1% Cu-Fe (7:1)/SiO_2 catalyst

In summary, high surface area Cu-Fe/SiO_2 catalysts were synthesized. The effect of iron co-impregnation initially leads to spinel $CuFe_2O_4$ formation upon calcination and yields better Cu dispersion after reduction. The in-situ UV-VIS investigations show that copper is reduced at temperatures of about 543 K.

3.4 Catalytic Tests

Silica supported Cu can convert furfural to furfuryl alcohol and 2-methylfuran in a two-step series reaction:[2]

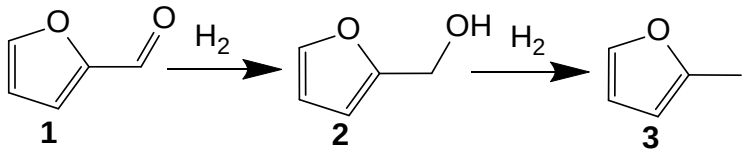

Figure 3.6 Reaction network of furfural hydrodeoxygenation

3.4.1 Study on Catalyst Stability

Previous reports have shown that supported Cu or $Cu_2Cr_2O_5$ are good catalysts for the selective conversion of furfural to furfuryl alcohol.[4] Consistent with these investigations here a 1% Cu/SiO_2 forms predominantly furfuryl alcohol (78% selectivity at 9% furfural conversion) at a temperature of 483 K, with a total flow of 124 mmol h^{-1} (1% furfural, 99% H_2).The catalytic tests ran for up to 3 hours on stream for the 1% $Cu\text{-}Fe/SiO_2$ catalyst; in this period carbon balance was maintained at least at 85%+ and conversion decreased from 34% to 27% at a rate 0.058 h^{-1} assuming linear decay. Selectivity remained nearly constant during this period (Figures 3.7).

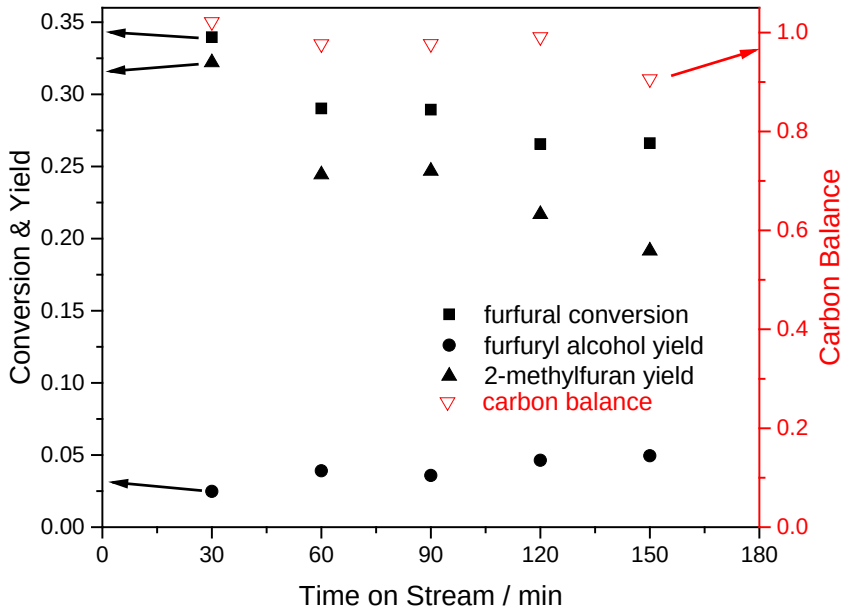

Figure 3.7 Furfural reaction with 1% Cu-Fe(7:1)/SiO_2 (reaction condition: 483 K, atmospheric pressure, WHSV = 2.3 h^{-1}, 50 mg, 543K pre-reduced catalyst)

In Figure 3.8, the initial furfural conversion decreased to 16% with the 5%-diluted Cu-Fe(7:1)/SiO_2. During the 2-hour test, the conversion only decreased slightly from 16% to about 15%, while the selectivity of furfuryl alcohol remained at ~90%. The carbon balance stayed at 90%+ in this run.

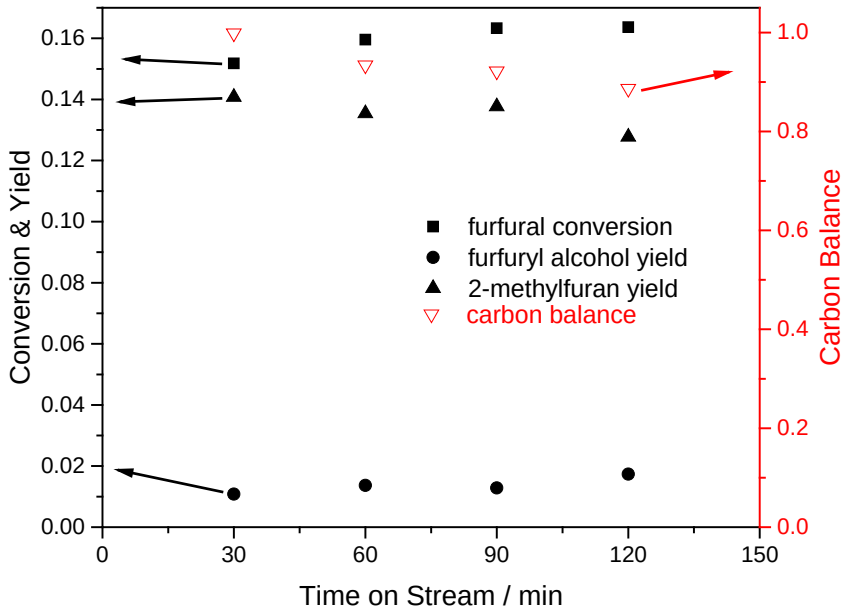

Figure 3.8 Furfural reaction with 5%-diluted 1% Cu-Fe(7:1)/SiO_2 (reaction condition: 483 K, atmospheric pressure, WHSV = 2.3 h^{-1}, 100 mg, 543K pre-reduced catalyst)

The reaction results of furfural alcohol on the 1% Fe/SiO_2 is presented in Figure 3.9. The conversion of furfural alcohol remained at 95%+ during the 4-hour run, and a ~85% selectivity of 2-methylfuran was observed in the test. Note there is a small amount of furfural generated during the run, indicating the reverse reaction from furfuryl alcohol to furfural, while the reactivity is neglectable when compared to the conversion to 2-methylfuran.

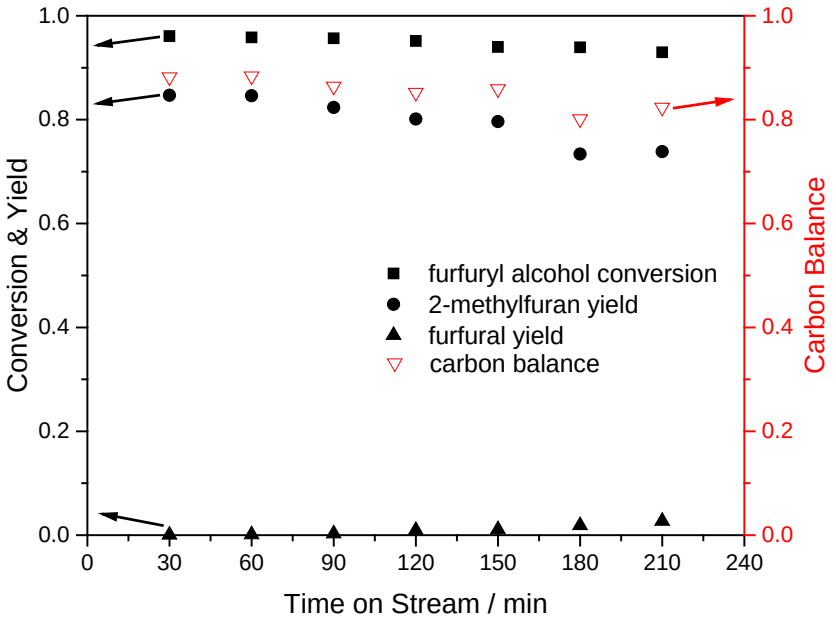

Figure 3.9 Furfuryl alcohol reaction with 1% Fe/SiO_2 (reaction condition: 483 K, atmospheric pressure, WHSV = 2.3 h^{-1}, 50 mg, 543K pre-reduced catalyst)

Furfural reaction at different temperatures was investigated and the results are shown in Figure 3.10. When the temperature was increased from 483 K to 523 K, the conversion of furfural doubled from ~8% to 16%. While the selectivity of furfuryl alcohol decreased slightly at higher temperature, the selectivity of 2-methylfuran increased. The result that high temperature favors the production of 2-methylfuran, suggesting that the second step conversion of furfuryl alcohol requires more energy and possesses a higher activation energy.

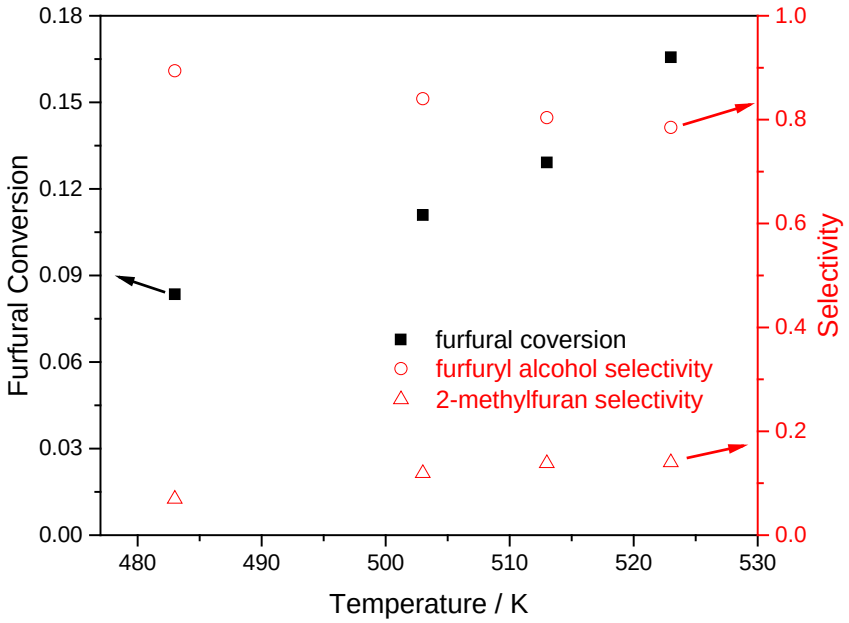

Figure 3.10 Furfural reaction with 1% Cu/SiO_2 at different temperatures (reaction condition: 483 – 523 K, atmospheric pressure, WHSV = 2.3 h^{-1}, 50 mg, 543K pre-reduced catalyst)

3.4.2 Effect of Iron on the Catalyst Reactivity

Addition of Fe (0.15% w/w) increases reaction rates by more than a factor of 3 (Table 3.3) without loss in selectivity. According to the N_2O pre-oxidized TPR results discussed above, more active Cu sites were generated in the Fe co-impregnated samples and therefore the reaction rates increased. However, the increase in surface area is insufficient to explain the observed increase in reaction rates and thus there seems to be an additional promotion effect generated by the presence of this small amount of iron.

Table 3.3 Reactivity of Cu-Fe/SiO_2 catalysts with furfural

Catalysts[a]	Conversion of furfural	Selectivity to furfuryl alcohol	Selectivity to 2-methylfuran
Cu/SiO_2	9%	78%	11%
Cu-Fe (9:1)/SiO_2	16%	87%	7%
Cu-Fe (7:1)/SiO_2	31%	74%	16%

a All samples have 1%Cu w/w

Cu-Fe (7:1)/SiO_2 shows the highest reaction rates of the three samples depicted in Table 3.3, with a furfural conversion of 31%. In fact, at a dilution ratio of 19:1 (w/w) conversion decreases only to 16% (see Table 3.4) suggesting that there is a product inhibition effect on reaction rates at this level of conversion. The results depicted in Table 4 also show that reduction temperature has an important effect on the selectivity of the reaction. In particular, by raising the reduction temperature from 483 K to 543 K, the product selectivity shifted from furfuryl alcohol to 2-methylfuran at the same conversion.

Table 3.4 Reactivity of 5% silica gel diluted Cu-Fe (7:1)/SiO_2 catalysts with furfural

Catalysts	Reduction temperature (K)	Conversion of furfural	Selectivity to furfuryl alcohol	Selectivity to 2-methylfuran
Cu-Fe (7:1)	483	16%	86%	7%
Cu-Fe (7:1)	543	16%	8%	90%

Turnover frequencies (TOF) of Cu-Fe/SiO_2 catalysts were calculated as the number of furfural molecules reacted per Cu site per unit time (Table 3.5). The TOF of Cu/SiO_2 (0.019 s^{-1}) is comparable with other supported Cu catalysts such as Cu/C[7]

(0.018 – 0.032 s^{-1}) and Cu/MgO[8] (0.005 – 0.038 s^{-1}). However, the TOF for Cu-Fe (7:1)/SiO_2 is more than ten times larger than the values obtained for pure Cu.

Table 3.5 Turnover frequencies of Cu-Fe/SiO_2 catalysts

Catalyst Samples[a]	weight (mg)	reduction T (K)	*TOF* (s^{-1})
Cu/SiO_2	50	483	0.019
Cu-Fe(7:1)/SiO_2	100	483	0.257
Cu-Fe(7:1)/SiO_2	100	543	0.266

a Cu-Fe catalysts are diluted with silica gel to 5% of the initial concentration.

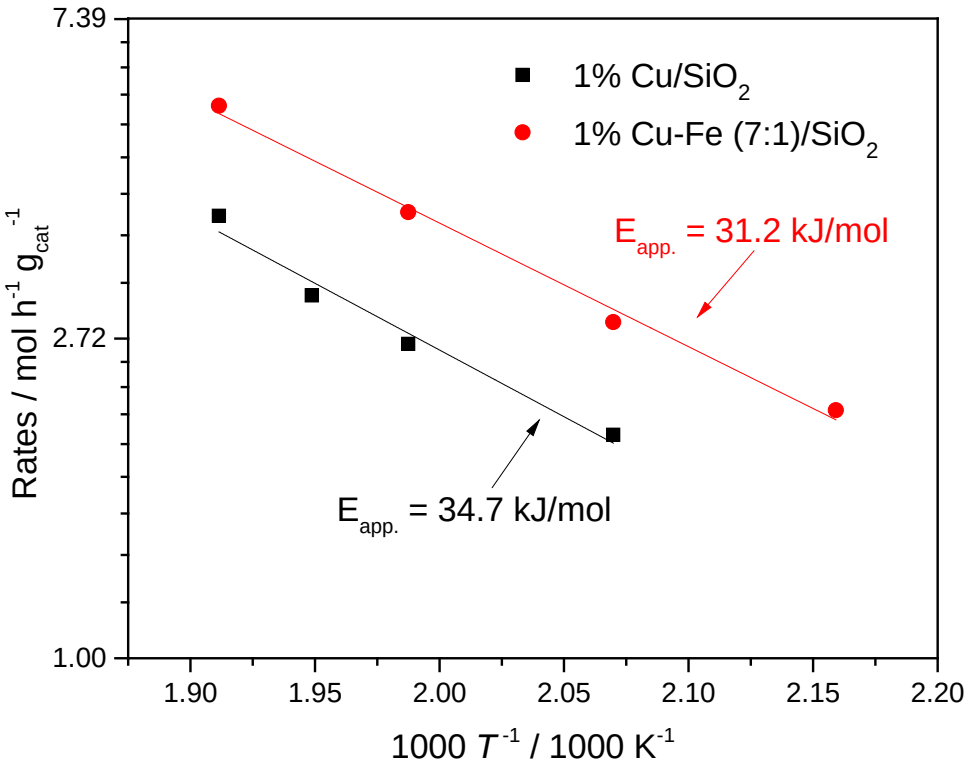

Figure 3.11 Measured apparent activation energy of furfural conversion with 1% Cu/SiO_2 and 1% Cu-Fe (7:1)/SiO_2.

The apparent activation energy of the furfural to furfuryl alcohol reaction was measured (Figure 3.11) with a WHSV of 2.3 h^{-1}, at T = 463~523 K, and atmospheric pressure. A pre-reduction temperature of 483 K was selected to keep the selectivity to furfuryl alcohol high. A value of 34.7 kJ/mol was obtained for the 1% Cu/SiO_2 catalyst, and a value of 31.2 kJ/mol was obtained for the 1% Cu-Fe(7:1)/SiO_2. These similar values suggest that the rate-determining step and the active site for the reaction is similar in both catalysts for the conversion of furfural to furfuryl alcohol.

3.4.3 Identification of Active Iron Species

To understand the role of Fe and the effect of reduction temperature on selectivity, a sample of 1% Fe/SiO_2 was investigated after H_2 reduction at 483 K or 543 K. Furfural or furfuryl alcohol were fed separately to the reactor after the reduction step was completed (Table 3.6). There was no significant conversion when furfural is the reactant, however, when furfuryl alcohol is used as the reactant and the iron catalyst is pre-reduced at a temperature of 543 K, 2-methyl furan is produced with a high selectivity (89%) at 95% furfuryl alcohol conversion.

Table 3.6 Reactivity of Fe/SiO_2 with furfuryl alcohol

Catalyst	Reduction temperature (K)	Conversion of furfuryl alcohol	Selectivity to 2-methylfuran
1% Fe/SiO_2	483	12%	25%
1% Fe/SiO_2	543	95%	89%

The TPR experiments presented before suggest that in the presence of Cu, Fe can be partially reduced at temperatures as low as 573 K. In situ IR investigations of adsorbed NO have been carried out to elucidate the oxidation state of the Fe species that serve as active sites in the reduction of furfuryl alcohol. The high affinity of NO

towards exposed Fe^{2+} and Fe^{3+}metal centers makes this a highly sensitive technique for the characterization of exposed Fe^{x+} centers.

The stretching frequencies of homogeneous Fe-organic complexes such as $[FeL_n(NO)]^+X^-$,[29] are usually observed in the 1800 – 1900 cm^{-1} range. When Fe is well distributed onto a zeolite or a silica surface, due to the interaction of Fe and the supports, the *d*-π back-donation properties decrease. As a consequence, the $\nu[Fe^{2+}(NO)]$ stretching frequencies are observed at lower energies (1700 – 1800 cm^{-1} range).[30] Multiple NO molecules (1, 2, or 3) can be absorbed onto Fe^{2+} depending on the sites structure as has been reported in a number of publications.[30, 31]

As shown in Figure 3.12, there was no IR band related to NO absorbed onto Fe^{2+} after a H_2 treatment at 483 K. In contrast, if the reduction temperature is increased to 543 K, an IR absorption band is observed at 1745 cm^{-1}. This peak was assigned to ν(NO) stretching in $Fe^{2+}(NO)_2$ complexes where two NO molecules were absorbed onto single Fe^{2+} site based on the assignments done on Fe-containing zeolites.[31]

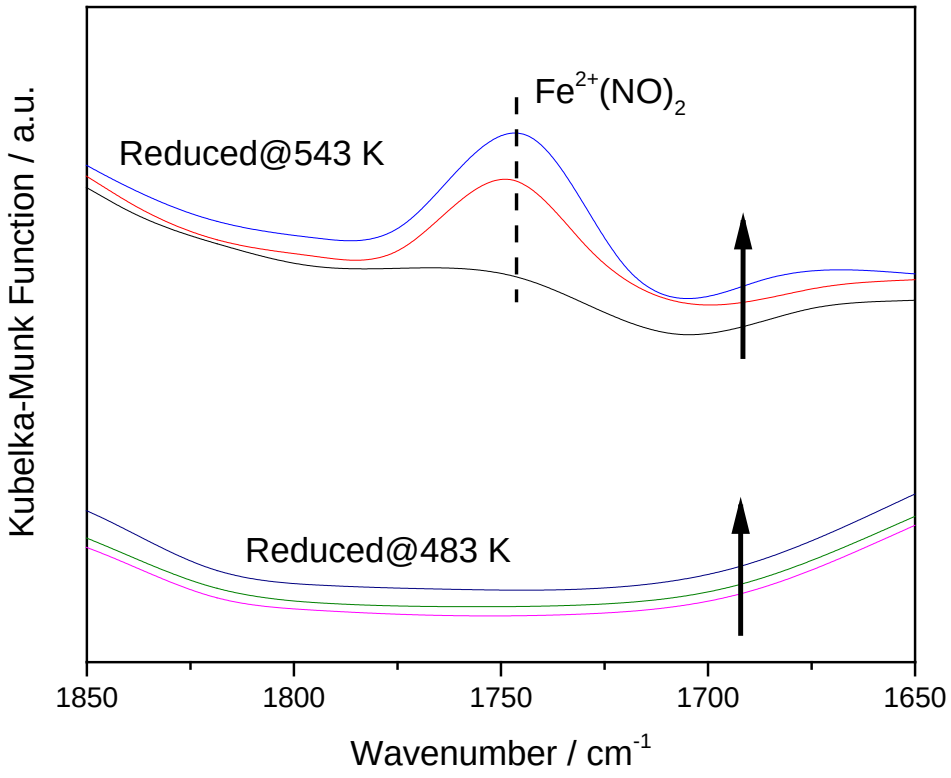

Figure 3.12 Infrared spectra of NO adsorbed on Cu-Fe/SiO_2 catalysts (Spectra were recorded every 24 min) reduced at different temperatures.

At first a redox mechanism involving oxygen vacancies was considered for the hydrogenation of furfural on Cu-Fe/SiO_2 catalyst, but this hypothesis was discarded since the reduced Fe species are not reactive with furfural without the presence of Cu. Therefore the in-situ formed Fe^{2+} species are necessary for the high activity of the Cu-Fe catalyst for furfuryl alcohol hydrogenation. Examples of the hydrogenation properties of Fe (II) exist in both homogeneous and heterogeneous catalysis. In homogeneous catalysis, Fe(II) species were reported to possess noble metal properties in multiple applications including aldehyde,[32] ketone,[33] and C=C bond hydrogenation.[34] In heterogeneous catalysis, Fe/SiO_2 and other supports such as

activated carbon, have been shown to be selective for the hydrodeoxygenation of m-cresol and guaiacol to benzene toluene with no ring hydrogenation activity.[35, 36]

In a summary, we have determined that iron is a promoter of Cu/SiO_2 catalysts for the furfural hydrodeoxygenation reaction. The high selectivity of C=O group hydrogenation on Cu-based catalysts lays in the weak affinity of Cu surface to C=C bonds.[5] Therefore only side chain of furfural is adsorbed on the catalyst surface and being hydrogenated,[37] which explains no decarbonylation, ring hydrogenation, or even ring opening reactions were observed in our system. According to Kameoka and coworkers,[22] the formation of $CuFe_2O_4$ spinel structure during the calcination brings down the Cu particle sizes after further reduction and thus increases the catalyst activity. We have found that a small amount of iron (0.15% w/w) is sufficient to increase copper dispersion, enhancing catalyst reaction rates. Further we found the product selectivity can be tuned by controlling the oxidation state of iron. If the iron promoted Cu/SiO_2 is pre-reduced at 543 K, the reaction selectivity totally shifted from furfuryl alcohol to 2-methylfuran. Under these conditions the iron species are partially reduced and the formed Fe^{2+} sites function as co-catalyst increasing the rate of reduction of the furfuryl alcohol to 2-methylfuran.

3.5 Conclusions

The furfural hydrogenation to furfuryl alcohol and 2-methylfuran has been investigated over Cu/SiO_2 and $Cu\text{-}Fe/SiO_2$ catalyst at low metal loading. The reaction network is a two-step series reaction: carbonyl hydrogenation and then hydrodeoxygenation of the alcohol group. We have identified an iron promoted Cu/Silica catalyst that selectively converts furfural to 2-methylfuranwith over 90% selectivity.

Supported Cu is well known as a commercial catalyst to produce furfuryl alcohol from furfural, but only has a selectivity of 11% to 2-methylfuran. Addition of a small amount of Fe (up to 0.15% w/w) to the Cu (1% w/w) catalyst increases reaction rates by more than a factor of 3 without change in selectivity (31% furfural conversion, 16% selectivity to 2-methylfuran). Catalyst pre-reduction at a temperature of 543 K changes the catalyst properties leading to a significant enhancement of 2-methylfuran selectivity (90%), when compared to pre-treatment at 483 K. TPR investigations indicate that the reduction of Fe was not complete at either reduction temperature. In situ FT-IR experiments with NO as the probe molecule further showed that Fe^{2+} active sites are generated after a reduction at 543 K instead of 483K. In a conclusion, we have found promotion effects of iron in two forms: firstly the co-impregnated iron increased the copper dispersion and reaction rates substantially in what may be called structural promotion effect; secondly the partially reduced Fe can act as a co-catalyst and selectively convert furfuryl alcohol to 2-methylfuran, which was responsible for the reaction selectivity shift after the addition of Fe.

REFERENCES

[1] G.W. Huber, S. Iborra, A. Corma, Synthesis of transportation fuels from biomass: Chemistry, catalysts, and engineering, Chemical Reviews, 106 (2006) 4044-4098.

[2] J.-P. Lange, E. van der Heide, J. van Buijtenen, R. Price, FurfuralυA Promising Platform for Lignocellulosic Biofuels, Chemsuschem, 5 (2012) 150-166.

[3] U.S.E.I. Administration, Commercial-scale cellulosic ethanol plant opens, in, Online, 2014.

[4] B.H. Wojcik, CATALYTIC HYDROGENATION OF FURAN COMPOUNDS, Industrial and Engineering Chemistry, 40 (1948) 210-216.

[5] S. Sitthisa, T. Sooknoi, Y. Ma, P.B. Balbuena, D.E. Resasco, Kinetics and mechanism of hydrogenation of furfural on Cu/SiO2 catalysts, Journal of Catalysis, 277 (2011) 1-13.

[6] D. Vargas-Hernandez, J.M. Rubio-Caballero, J. Santamaria-Gonzalez, R. Moreno-Tost, J.M. Merida-Robles, M.A. Perez-Cruz, A. Jimenez-Lopez, R. Hernandez-Huesca, P. Maireles-Torres, Furfuryl alcohol from furfural hydrogenation over copper supported on SBA-15 silica catalysts, Journal of Molecular Catalysis a-Chemical, 383 (2014) 106-113.

[7] R.S. Rao, R.T.K. Baker, M.A. Vannice, Furfural hydrogenation over carbon-supported copper, Catalysis Letters, 60 (1999) 51-57.

[8] B.M. Nagaraja, V.S. Kumar, V. Shasikala, A.H. Padmasri, B. Sreedhar, B.D. Raju, K.S.R. Rao, A highly efficient Cu/MgO catalyst for vapour phase hydrogenation of furfural to furfuryl alcohol, Catalysis Communications, 4 (2003) 287-293.

[9] C.P. Jimenez-Gomez, J.A. Cecilia, D. Duran-Martin, R. Moreno-Tost, J. Santamaria-Gonzalez, J. Merida-Robles, R. Mariscal, P. Maireles-Torres, Gas-

phase hydrogenation of furfural to furfuryl alcohol over Cu/ZnO catalysts, Journal of Catalysis, 336 (2016) 107-115.

[10] S. Srivastava, N. Solanki, P. Mohanty, K.A. Shah, J.K. Parikh, A.K. Dalai, Optimization and Kinetic Studies on Hydrogenation of Furfural to Furfuryl Alcohol over SBA-15 Supported Bimetallic Copper-Cobalt Catalyst, Catalysis Letters, 145 (2015) 816-823.

[11] S. Sitthisa, D.E. Resasco, Hydrodeoxygenation of Furfural Over Supported Metal Catalysts: A Comparative Study of Cu, Pd and Ni, Catalysis Letters, 141 (2011) 784-791.

[12] M. Li, Y. Hao, F. Cardenas-Lizana, M.A. Keane, Selective production of furfuryl alcohol via gas phase hydrogenation of furfural over Au/Al2O3, Catalysis Communications, 69 (2015) 119-122.

[13] W.-S. Lee, Z. Wang, W. Zheng, D.G. Vlachos, A. Bhan, Vapor phase hydrodeoxygenation of furfural to 2-methylfuran on molybdenum carbide catalysts, Catalysis Science & Technology, 4 (2014) 2340-2352.

[14] J. Luo, M. Monai, H. Yun, L. Arroyo-Ramirez, C. Wang, C.B. Murray, P. Fornasiero, R.J. Gorte, The H-2 Pressure Dependence of Hydrodeoxygenation Selectivities for Furfural Over Pt/C Catalysts, Catalysis Letters, 146 (2016) 711-717.

[15] M.J. Taylor, L.J. Durndell, M.A. Isaacs, C.M.A. Parlett, K. Wilson, A.F. Lee, G. Kyriakou, Highly selective hydrogenation of furfural over supported Pt nanoparticles under mild conditions, Applied Catalysis B-Environmental, 180 (2016) 580-585.

[16] P. Panagiotopoulou, N. Martin, D.G. Vlachos, Effect of hydrogen donor on liquid phase catalytic transfer hydrogenation of furfural over a Ru/RuO2/C catalyst, Journal of Molecular Catalysis a-Chemical, 392 (2014) 223-228.

[17] J. Jae, W. Zheng, A.M. Karim, W. Guo, R.F. Lobo, D.G. Vlachos, The Role of Ru and RuO2 in the Catalytic Transfer Hydrogenation of 5-Hydroxymethylfurfural for the Production of 2,5-Dimethylfuran, Chemcatchem, 6 (2014) 848-856.

[18] M.J. Gilkey, P. Panagiotopoulou, A.V. Mironenko, G.R. Jenness, D.G. Vlachos, B. Xu, Mechanistic Insights into Metal Lewis Acid-Mediated Catalytic Transfer Hydrogenation of Furfural to 2-Methylfuran, Acs Catalysis, 5 (2015) 3988-3994.

[19] K. Yan, A.C. Chen, Selective hydrogenation of furfural and levulinic acid to biofuels on the ecofriendly Cu-Fe catalyst, Fuel, 115 (2014) 101-108.

[20] M. Manikandan, A.K. Venugopal, A.S. Nagpure, S. Chilukuri, T. Raja, Promotional effect of Fe on the performance of supported Cu catalyst for ambient pressure hydrogenation of furfural, Rsc Advances, 6 (2016) 3888-3898.

[21] R.M. Lukes, C.L. Wilson, REACTIONS OF FURAN COMPOUNDS .11. SIDE CHAIN REACTIONS OF FURFURAL AND FURFURYL ALCOHOL OVER NICKEL COPPER AND IRON COPPER CATALYSTS, Journal of the American Chemical Society, 73 (1951) 4790-4794.

[22] S. Kameoka, T. Tanabe, A.P. Tsai, Spinel CuFe2O4: a precursor for copper catalyst with high thermal stability and activity, Catalysis Letters, 100 (2005) 89-93.

[23] E. de Smit, F.M.F. de Groot, R. Blume, M. Haevecker, A. Knop-Gericke, B.M. Weckhuysen, The role of Cu on the reduction behavior and surface properties of Fe-based Fischer-Tropsch catalysts, Physical Chemistry Chemical Physics, 12 (2010) 667-680.

[24] A.F.H. Wielers, C. Hop, J. Vanbeijnum, A.M. Vanderkraan, J.W. Geus, ON THE PROPERTIES OF SILICA-SUPPORTED BIMETALLIC FE-CU CATALYSTS .1. PREPARATION AND CHARACTERIZATION, Journal of Catalysis, 121 (1990) 364-374.

[25] E. de Smit, I. Swart, J.F. Creemer, C. Karunakaran, D. Bertwistle, H.W. Zandbergen, F.M.F. de Groot, B.M. Weckhuysen, Nanoscale Chemical Imaging of the Reduction Behavior of a Single Catalyst Particle, Angewandte Chemie-International Edition, 48 (2009) 3632-3636.

[26] S. Xia, R. Nie, X. Lu, L. Wang, P. Chen, Z. Hou, Hydrogenolysis of glycerol over Cu-0.4/Zn5.6-xMgxAl2O8.6 catalysts: The role of basicity and hydrogen spillover, Journal of Catalysis, 296 (2012) 1-11.

[27] O. Martin, C. Mondelli, D. Curulla-Ferre, C. Drouilly, R. Hauert, J. Perez-Ramirez, Zinc-Rich Copper Catalysts Promoted by Gold for Methanol Synthesis, Acs Catalysis, 5 (2015) 5607-5616.

[28] F. Boccuzzi, S. Coluccia, G. Martra, N. Ravasio, CuiSiO(2) and Cu/SiO2-TiO2 catalysts I. TEM, DR UV-Vis-NIR, and FTIR characterisation, Journal of Catalysis, 184 (1999) 316-326.

[29] McClever.Ja, N.M. Atherton, J. Locke, E.J. Wharton, C.J. Winscom, TRANSITION METAL-DITHIOLENE COMPLEXES .3. NITROSYL COMPLEXES OF IRON AND COBALT, Journal of the American Chemical Society, 89 (1967) 6082-&.

[30] C. Lamberti, A. Zecchina, E. Groppo, S. Bordiga, Probing the surfaces of heterogeneous catalysts by in situ IR spectroscopy, Chemical Society Reviews, 39 (2010) 4951-5001.

[31] A. Zecchina, M. Rivallan, G. Berlier, C. Lamberti, G. Ricchiardi, Structure and nuclearity of active sites in Fe-zeolites: comparison with iron sites in enzymes and homogeneous catalysts, Physical Chemistry Chemical Physics, 9 (2007) 3483-3499.

[32] N. Gorgas, B. Stoeger, L.F. Veiros, K. Kirchner, Highly Efficient and Selective Hydrogenation of Aldehydes: A Well-Defined Fe(II) Catalyst Exhibits Noble-Metal Activity, Acs Catalysis, 6 (2016) 2664-2672.

[33] N. Meyer, A.J. Lough, R.H. Morris, Iron(II) Complexes for the Efficient Catalytic Asymmetric Transfer Hydrogenation of Ketones, Chemistry-a European Journal, 15 (2009) 5605-5610.

[34] S. Gaillard, J.-L. Renaud, Iron-Catalyzed Hydrogenation, Hydride Transfer, and Hydrosilylation: An Alternative to Precious-Metal Complexes?, Chemsuschem, 1 (2008) 505-509.

[35] R.N. Olcese, M. Bettahar, D. Petitjean, B. Malaman, F. Giovanella, A. Dufour, Gas-phase hydrodeoxygenation of guaiacol over Fe/SiO2 catalyst, Applied Catalysis B-Environmental, 115 (2012) 63-73.

[36] L. Nie, P.M. de Souza, F.B. Noronha, W. An, T. Sooknoi, D.E. Resasco, Selective conversion of m-cresol to toluene over bimetallic Ni-Fe catalysts, Journal of Molecular Catalysis a-Chemical, 388 (2014) 47-55.

[37] S. Sitthisa, W. An, D.E. Resasco, Selective conversion of furfural to methylfuran over silica-supported Ni-Fe bimetallic catalysts, Journal of Catalysis, 284 (2011) 90-101.

[38] P.J. Chupas, K.W. Chapman, C. Kurtz, J.C. Hanson, P.L. Lee, C.P. Grey, A versatile sample-environment cell for non-ambient X-ray scattering experiments, Journal of Applied Crystallography, 41 (2008) 822-824.

Chapter 4

CARBOXYLIC ACID HYDROGENATION TO ITS CORRESPONDING ALDEHYDE WITH Cr_2O_3 CATALYSTS

4.1 Introduction

Carboxylic acids occur widely in nature in molecules such as fatty acids derived from triglycerides, and in many other organic acids from plants and fruits. In the chemical industry, carboxylic acids are essential chemicals for the production of polymers, pharmaceuticals, and food additives.[1] In addition, carboxylic acids can be potentially produced in large scale from lignocellulosic biomass,[2] a renewable carbon source in contrast to current industrial processes that are based on catalytic oxidation.[3]

An abundant source of carboxylic acids from biomass can be hydrogenated to the corresponding aldehyde and alcohol: the challenge is to do this selectively. It is relatively easier to hydrogenate carboxylic acids to alcohols, as the process has been extensively studied over many metallic catalysts such as Ru, Pt, Cu-Fe.[4-8] This chapter discusses the selective hydrogenation of carboxylic acids to aldehydes, species that will be hydrogenated to alcohols on these metallic catalysts in a second step. Aldehydes are important chemicals in industry since they are versatile intermediates to other valuable chemicals such as amines, polymers, and ingredients in flavors and perfumes.[3]

Grootendorst et al.[9] reported the conversion of acetic acid to acetaldehyde over Fe_3O_4, in the presence of hydrogen at ambient pressure. They claim that the

simultaneous existence of metallic iron and oxygen vacancies is responsible for the high selectivity towards acetaldehyde. Pestman et al.[10] also investigated the acetic acid conversion over other transition metal oxides and found that iron oxide showed the best properties in this redox reaction. They also concluded that the 'right' metal-oxygen bond strength is essential in this reaction. If the metal-oxygen bond is too weak, such as in Pb, Cu, Ni, these metal are easily reducible and thus not reactive or selective for the production of aldehyde. If the metal-oxygen bond is too strong, such as Ti, Zr, Al, the metal oxide bond is not reducible and acetone is the main product through the ketonization reaction.

Yokoyama and Fujita[11-13] found that 10% Cr_2O_3/α-Al_2O_3 catalyst can almost completely convert a variety of carboxylic acids to the corresponding aldehyde, when compared to 10% Cr_2O_3/γ-Al_2O_3. However, they only stated that the nature of the catalyst surface rather than the crystal phase is the key in the high activity. According to Pestman,[10] Cr–O bond strength is much higher than that of iron oxide and only showed 8% selectivity in the conversion of acetic acid. Pestman proposed a reaction mechanism of acetic acid on iron oxide, where the hydrogen spill-over is facilitated by metallic iron and the surface reaction is taken place on the oxygen vacancy. The reaction mechanism of carboxylic acids hydrogenation over Cr_2O_3, however, has not been studied and discussed in detail.

In this chapter, I show that Cr_2O_3 catalyst can catalyze hydrogenation of aliphatic acids with over 90% selectivity towards aliphatic acids with carbon chains larger than C3 but that they are poor catalysts for acetic acid hydrogenation. The surface reaction mechanism is analyzed with a model that evaluates different adsorption configurations for the carboxylic acid and aldehyde. Finally, the rate

expression of aldehyde formation is derived from the proposed reaction mechanism and further validated with a few experimental results.

4.2 Materials and Methods

4.2.1 Catalyst Preparation

Supported chromium oxide catalysts were synthesized by the wetness impregnation method at a liquid to solid ratio of 1 mL/g. Typically, $Cr(NO_3)_3 \cdot 9H_2O$ (99.99%, Sigma-Aldrich) was dissolved in DI water and γ-Al_2O_3 or α-Al_2O_3 (99.97%, 99.9%, Alfa Aesar) was then added into the aqueous solution. After drying at the room temperature for 12 hours, the mixture was transferred to an oven at 393 K for 12 h. The dried catalyst was then calcined at 823 K for 5 hours, with a ramping rate of 2 K/min. The catalyst was not further treated before the test. The loadings of chromium that are discussed in this chapter are 1%, 10%, and 20% wt. Bulk chromium oxide (99.9%, Sigma-Aldrich) was used as received without any treatment.

4.2.2 In-situ Diffuse Reflectance UV-VIS Study

Diffused reflectance UV-VIS study was carried out using a flow cell and a Jasco V550 UV-VIS spectroscopy. The in-situ flow cell is made of U-shaped quartz round tube with a UV window made of square quartz tube (Quartz Plus, Inc.), as introduced in Chapter 2. Typically, 100 mg of the catalyst sample was loaded into the flow cell at the window. During the experiment, the catalyst was treated with hydrogen at reaction temperature for 2 h first. After cooling down to room temperature in a flow of helium, the spectra were taken under the helium flow.

4.2.3 H_2-D_2 Scrambling Experiments

The H_2-D_2 scrambling experiment was carried out in the same setup for the catalysts evaluation. Typically, 50 mg of catalyst was loaded in the two feet long quartz tube reactor between two layers of quartz wool. Before heating the reactor, a 5 sccm of hydrogen flow was fed into the reactor until the hydrogen signal was stabilized in the mass spectroscopy. Then a 5 sccm of deuterium flow was co-fed into the reactor at room temperature. After the signal of deuterium was stabilized for at least 15 min, the reactor was heated by a furnace with a ramping rate of 5 K/min. After the final temperature was reached, the system was held at 623 K for at least 30 min until all the signals were stabilized. The gases outlet was connected to a mass spectrometer (Pfeiffer, Thermostar GSD 320T) for the analysis.

4.2.4 Propionic Acid Reaction with D_2

The reaction of propionic acid with D_2 was carried out in the same setup for the catalysts evaluation. Typically, 50 mg of catalyst was loaded in the two feet long quartz tube reactor between two layers of quartz wool. The reaction was studied with a 10 sccm of deuterium flow. The reactor was heated to the reaction temperature at a ramping rate of 5 K/min and held for analysis. After the signals of targeted products were stabilized for at least 15 min, 1 μL of propionic acid or propanal was injected from the top of the reactor. The products were collected and analyzed by a mass spectrometer (Pfeiffer, Thermostar GSD 320T).

4.2.5 Catalysts Evaluation

The catalysts were evaluated in a flow reactor made of 1/4’’ OD quartz tube. Typically, 50 mg catalyst was loaded in the middle of the reactor between two layers of quartz wool. Carboxylic acids including acetic acid (99.7%, Sigma-Aldrich),

propionic acid (99%, Alfa Aesar), butyric acid (99%+, Alfa Aesar), valeric acid (99%, Alfa Aesar), or hexanoic acid (99%, Sigma-Aldrich) were fed into the reactor using a syringe pump (NE-1000, New Era Pump System Inc.) and syringe (Hamilton) from the top of the tubing along with the reduction gas flow. The reactor was heated using a furnace and all the gas lines were wrapped with heating tapes and heated to the same temperature as the reactor to ensure an isothermal reaction system. All the products were collected and analyzed with an online gas chromatography (GC 2014, Shimadzu) that is equipped with an HP-INNOWax capillary column and an FID detector.

4.3 Results and Discussion

4.3.1 Diffuse Reflectance UV-VIS Study of Chromium Oxide

A diffuse reflectance UV-VIS study was conducted with chromium oxide catalysts. Chromium oxides present a variety of colors based on the oxidation state of chromium and have multiple absorption peaks in the UV and visible region. First the effect of supports was investigated with alpha- or gamma-alumina as supports and with bulk Cr_2O_3 as the reference. The results are present in Figure 4.1.

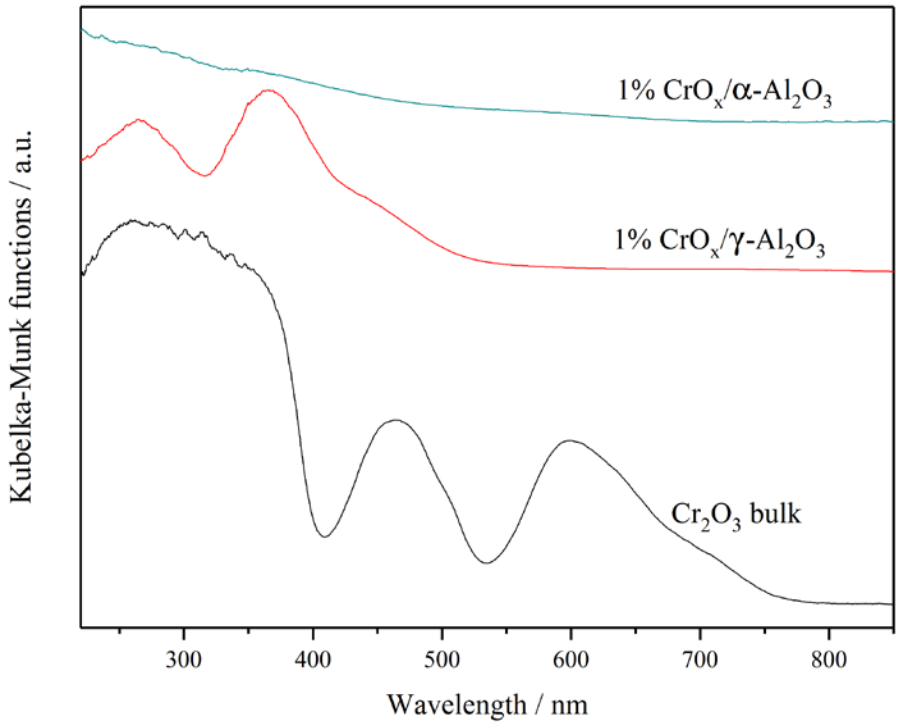

Figure 4.1 Chromium oxide supported on different materials

In Figure 4.1, two main peaks at 270 nm and 380 nm were observed on 1% $CrO_x/\gamma\text{-}Al_2O_3$. The two bands are typically attributed to tetrahedral chromate (Cr^{6+}) transitions.[14] These two bands were not clearly observed on 1% $CrO_x/\alpha\text{-}Al_2O_3$, indicating the chromium species are different from 1% $CrO_x/\gamma\text{-}Al_2O_3$. The structural differences in surface chromium species are yet to be explained here, but these spectral differences can be the bases for understanding the different reactivity that Yokoyama reported for similar materials.[11] In their report, Yokoyama found that 10% $Cr_2O_3/\gamma\text{-}Al_2O_3$ converted only 45% of caprylic acid with 36% selectivity to the

caprylaldehyde, while a 96% conversion and a 96% selectivity was obtained on 10% $Cr_2O_3/\alpha\text{-}Al_2O_3$ catalyst. The UV-VIS bands for bulk Cr_2O_3 are very different from the supported catalyst, as two bands at 470 nm and 610 nm were presented. These two bands can be attributed to *d-d* transition of trivalent chromium species.[15, 16] Weckhuysen et al. also reviewed the presence of these two UV-VIS bands in different Cr-containing materials including $\alpha\text{-}Cr_2O_3$.[17]

The effect of chromium loading was investigated on $\alpha\text{-}Al_2O_3$ and the results are shown in Figure 4.2.

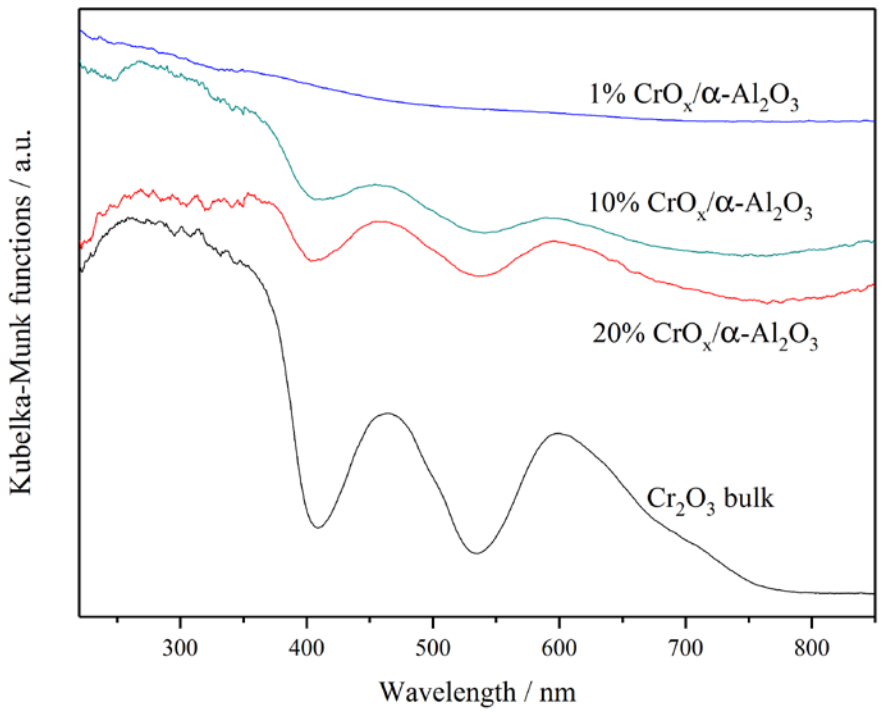

Figure 4.2 Different loadings of Chromium oxide supported on alpha-alumina

In Figure 4.2, as the loading of chromium is increased from 1% to 20% wt., it can be observed that the band intensity at 470 nm and 610 nm increased gradually. This suggests that the chromium surface species aggregate at higher loadings and the Cr^{3+} species are the stable chromium oxidation state during the calcination. This trend has also been reported by other authors.[14, 16, 17] For example, Cherian et al. found that when the loading of Cr was increased to 15% on Al_2O_3 support, the octahedral Cr^{3+} symmetry transitions were gradually developed, which led to two peaks centered at 460 and 600 nm.[16]

Finally, the effect of calcination temperature was investigated (Figure 4.3). The materials are all unsupported chromium oxide synthesized via a calcination of chromium nitrate at different temperatures. Before the UV-VIS spectra were collected at room temperature, the materials were treated in hydrogen at the reaction temperature of 623 K for 2 h.

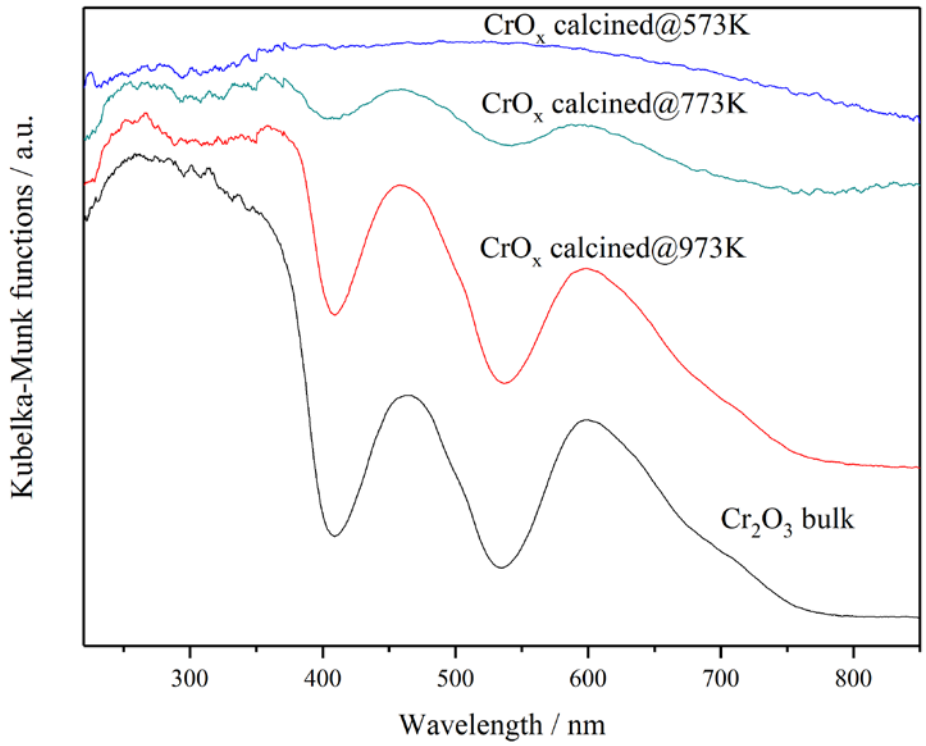

Figure 4.3 Effect of calcination temperatures on the unsupported chromium oxides with chromium nitrate as the precursor

As the calcination temperature is increased from 573 K to 973 K, a higher intensity of the two Cr^{3+} bands at 470 nm and 610 nm was observed over the unsupported chromium oxides catalysts. This observation indicates that Cr^{3+} species are the thermally stable species during the high temperature calcination at 973 K. This result is also consistent with the literature of the decomposition of $Cr(NO_3)_3 \cdot 9H_2O$,[18] where the Cr_2O_3 is found to be the favored product when the treatment temperature is higher than 723 K.

To summarize, the effect of supports is evaluated first and Cr^{6+} species were observed on γ-Al_2O_3 supported catalyst instead of α-Al_2O_3. If the loading of chromium is increased, the trivalent chromium become the dominant species on the α-Al_2O_3 supported catalyst. Finally, the increased bands intensity (denoted for Cr^{3+} species) at high calcination temperature suggests that Cr_2O_3 is the thermal stable product. The results of UV-VIS experiments identify the favored chromium species during the reaction and may help understand the different catalytic activities in the sections below.

4.3.2 H_2-D_2 Scrambling Experiments

H_2-D_2 scrambling experiments were carried out to understand the role of hydrogen dissociation on hydrogenation reactions with the Cr_2O_3 catalyst. First, the catalyst was treated with a hydrogen flow at room temperature and then deuterium gas was introduced. After the MS signals were stabilized, the reactor was heated to 623 K in the flow of hydrogen/deuterium gas mixture. Three MS signals (m/z = 2, 3, 4) were kept tracking through the experiment. The results are presented in Figure 4.4.

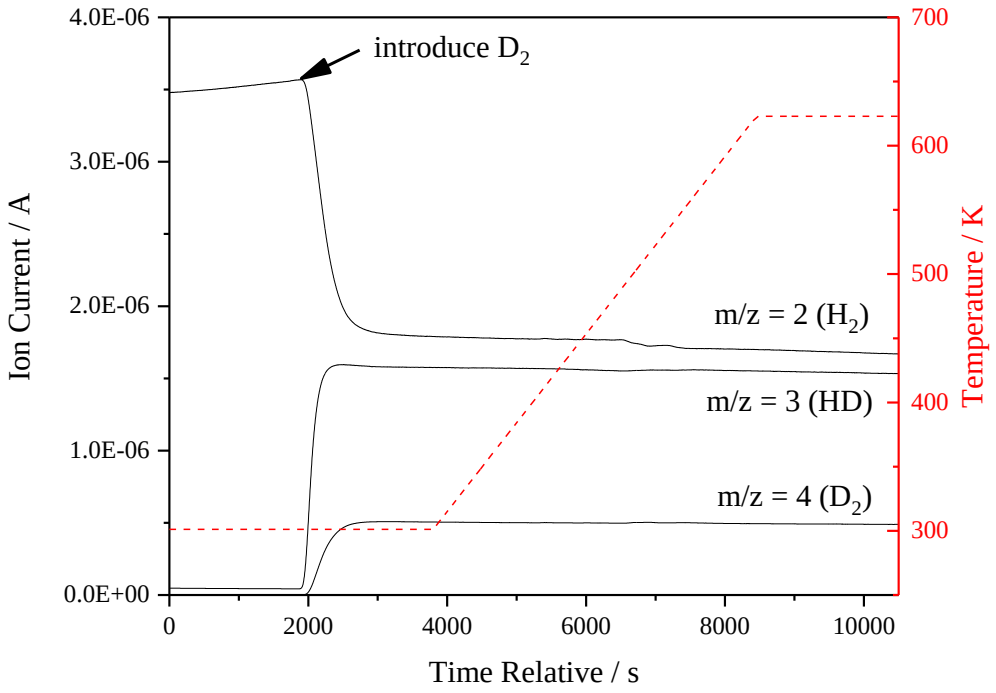

Figure 4.4 H_2-D_2 scrambling experiments on bulk Cr_2O_3 catalyst

As deuterium was introduced at t = 1950 s, the hydrogen signal (m/z = 2) decreased immediately and deuterium curve (m/z = 4) increased gradually. At the same time, the signal of HD (m/z = 3) increased, indicating the H_2-D_2 exchange reaction (Eqn 4.1) occurring on the Cr_2O_3 catalyst surface.

$$H_2 + D_2 \rightarrow 2HD \qquad \text{Eqn. 4.1}$$

Note that the reaction reached equilibrium within a few minutes at room temperature, as the HD curve plateaued after the sharp increase. When the reaction temperature was increased to 623 K at 5 K/min, the MS signals (m/z = 2, 3, 4) remained almost constant, suggesting that the H_2-D_2 exchange reaction equilibrium is independent on

the temperature ranging from 293 K to 623 K. According to the Van't Hoff equation (Eqn. 4.2), the enthalpy change of such reaction on Cr_2O_3 is very small.

$$\frac{d\ln K_{eq}}{dT} = \frac{\Delta H^{\ominus}}{RT^2} \qquad \text{Eqn. 4.2}$$

On other metal oxides that were reported to be effective for the hydrogenation of carboxylic acids, such as iron oxide,[10] the reduced metallic iron helps hydrogen spill-over first and then an oxygen vacancy is created by the removal of a water molecule. However, our results indicate that the hydrogen can dissociatively adsorb onto the Cr_2O_3 surface, without any metallic chromium sites being involved. This property has not been linked with hydrogenation of carboxylic acids before. However, Cr_2O_3 is a commercial catalyst in many related industrial processes such as dehydrogenation of propane to propene on chromia-alumina, known as the Houdry catalyst.[17] The active sites for hydrogen adsorption dissociation were reported to be Cr^{3+} sites, while it is not active with other stable chromium oxidation states such as Cr^{2+} and Cr^{6+}.[19] The mechanism was explained by Dowden and Wells,[20] in that the adsorption dissociation of hydrogen completes the octahedral coordination of the surface chromium ions and the large crystal field stabilization energy of the Cr^{3+} (d^3) is thus lowered (Figure 4.5). This reaction is reversible and occurring on the chromium oxide surface in a dynamic equilibrium. If both hydrogen and deuterium are presented and dissociated, there is a chance to form the new species of HD.

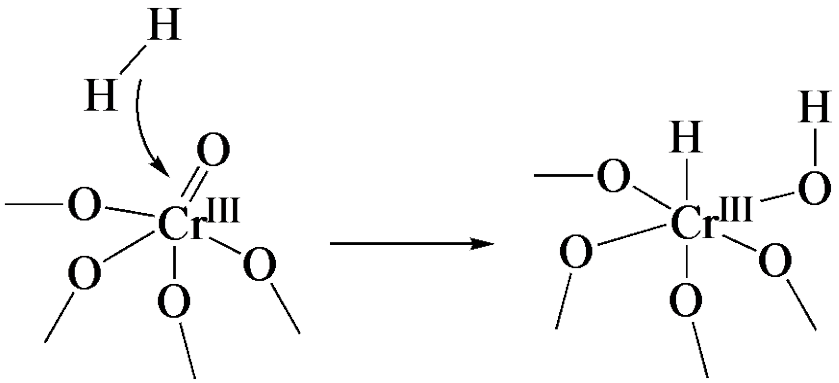

Figure 4.5 Schematic illustration of hydrogen heterolytic dissociation on Cr_2O_3

4.3.3 Propionic Acid Reaction with D_2

The surface reaction of propionic acid over Cr_2O_3 was investigated with deuterium as the reducing agent. This experiment was carried out at 623 K and atmospheric pressure under a 10 sccm flow of deuterium. Figure 4.6 presents the MS signals of CH_3CH_2CDO (m/z = 59) and CH_3CH_2CHO (m/z = 58) during three injections of 1 μL propanal or propionic acid. Deuterium was flowing from t = 0 s to t = 10000 s, when it was switched to helium. As for the three injections, the first two were in the presence of deuterium and the third one was in helium.

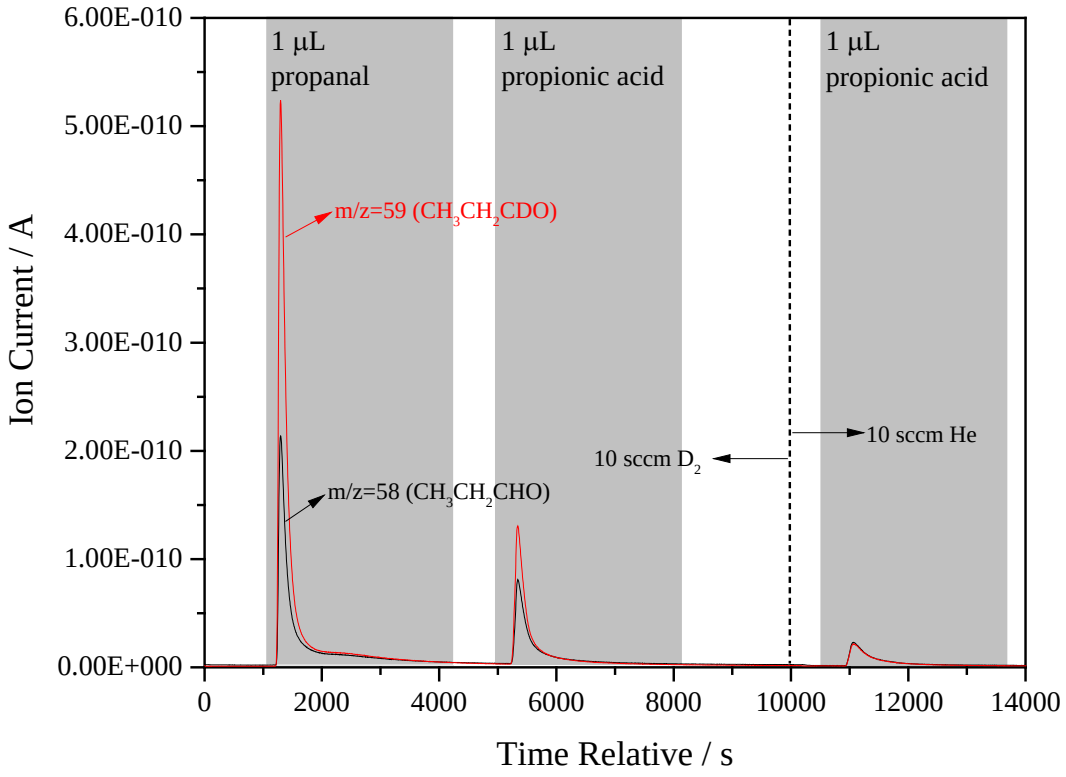

Figure 4.6 Propionic acid surface reaction with D_2

As showed in the figure, 1 µL propanal was injected at t = 1100 s and in the flow of deuterium, and both products peaks of the deuterium exchanged propanal (m/z = 59) and regular propanal (m/z = 58) were observed. For this injection, the ratio of area (CH_3CH_2CDO) : area (CH_3CH_2CHO) equals to 1.98 : 1. This result indicates that hydrogen in the aldehyde group can exchange fast with the surface dissociated deuterium.

At t = 5100 s and in the flow of deuterium, 1 µL of propionic acid was injected and both signals increased as well. However, the ratio of area (CH_3CH_2CDO) : area

(CH_3CH_2CHO) decreased to 1.30 : 1. This result suggests that the surface reaction occurs through a mechanism, where the formation of C–D bond is more favored instead of C–H bond where the proton is from the parent acid.

At t = 10000 s, the deuterium gas flow was switched to a 10 sccm of helium. After the system was stabilized, another 1 μL of propionic acid was introduced at t = 11000 s. Both deuterium exchanged propanal and regular propanal peaks were observed at this time, however the intensities were greatly decreased when compared to the results from the second injection. This result suggests that the catalyst surface was still covered with some dissociated deuterium, though the flowing gas was switched to helium. The decreased conversion implies that the surface active sites were consumed during the reaction and could not be regenerated without continuous flow of the reducing gas. The ratio of area (CH_3CH_2CDO) : area (CH_3CH_2CHO) further decreased to 0.95 : 1, in the last injection which is consistent with the fact that the surface had been purged with helium resulting in less deuterium surface concentration.

The different values of the ratio of area (CH_3CH_2CDO) : area (CH_3CH_2CHO) from the three the injections are related to the different types of molecular adsorption and the dissociated deuterium on the surface. The aldehyde adsorbs on the metal oxide in a configuration (Figure 4.7a) in which the oxygen in the aldehyde group binds to a surface Lewis site[21] or an oxygen vacancy.[22] In this case, the hydrogen from the parent aldehyde stays in the same plane of the carbonyl group, while the dissociated deuterium can attack the carbonyl group to form a C–D bond from both sides (Figure 4.7b). Assuming the C–H bond scission or the C–D bond formation is not the rate determining step, the formation of deuterium exchanged propanal is twice the chance

of the propanal remained unchanged when leaving the surface upon desorption. In fact, a ratio of 1.98 was observed when 1 μL propanal was introduced in the first injection, which is consistent with the above discussion.

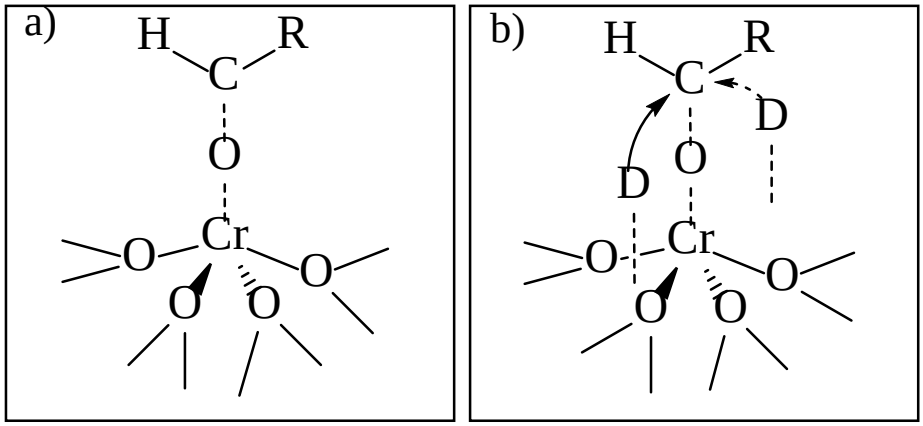

Figure 4.7 Illustration of (a) aldehyde adsorption configuration and (b) possible surface reaction on Cr_2O_3 surface

In general, when a carboxylic acid adsorbs on to the metal oxide surface, the adsorption process is described as an acid-base type reaction, where the acid molecule adsorbs dissociatively on a cation-anion site pair with the formation of a hydroxyl group and the conjugate base anion of the parent acid (Figure 4.8a).[23, 24] The aldehyde is formed following a C–O bond cleavage and the nearby hydrogen attack to form a C–H bond. Since the whole carboxylate group lies in the same plane, the chance of hydrogen/deuterium attack from either side should be equal, with an assumption of the C–H bond formation is not the rate determining step. Therefore if one side of the adsorbed carboxylate group is the dissociated hydrogen from the parent acid, and the other side is covered with the dissociated deuterium from gas phase

(Figure 4.8b), the formation rate of deuterium exchanged propanal should be similar to that of regular propanal. However, this was not observed in the experiment of propionic acid injection, as a ratio of 1.30 : 1 was obtained for the deuterium exchanged propanal to the regular propanal. Remember the results from the H_2-D_2 scrambling experiments, that the proton can leave the surface as HD and the vacancy can be filled with newly dissociated deuterium atom. In this case (Figure 4.8c), the deuterium exchanged propanal is the only possible product upon desorption. As a result of the reactions in Figure 4.8b and 4.8c, the deuterium exchanged propanal is more likely to form when compared to regular propanal, which explains the observed ratio of greater than 1. This theory was further studied with another 1 μL propionic acid injected after the flowing gas was switched to helium. In this case, the surface had only some residual deuterium, and H_2-D_2 exchange was less likely to take place under an inert gas atmosphere. Therefore the surface reaction presented in Figure 4.8b is possible instead of the reaction in Figure 4.8c. As a result, the formation rate of deuterium exchanged propanal should be similar to that of regular propanal (with an assumption that the C–H bond formation is not the rate determining step). This predicted result is consistent with the experimental result, as a ratio of 0.95 : 1 for the deuterium exchanged propanal to the regular propanal was obtained.

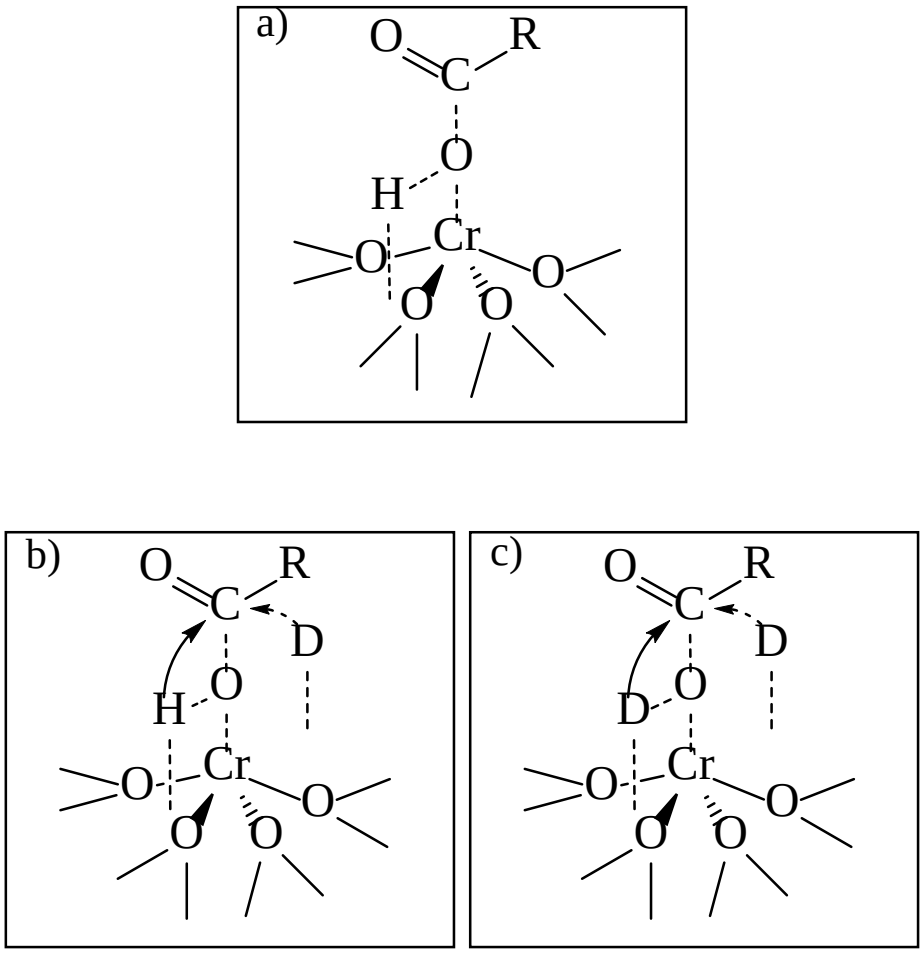

Figure 4.8 Illustration of (a) carboxylic acid adsorption on Cr_2O_3 surface, (b) possible surface reaction, (c) possible surface reaction after H-D exchange

4.4 Catalytic Tests

4.4.1 Reaction Results for C2-C6 Carboxylic Acid over Cr-containing Catalyst

A few experiments were carried out to investigate the effect of catalyst support, metal loading, and the calcination temperature on the reaction with hexanoic acid. The reason hexanoic acid was chosen as a model molecule is that it reaches the

detection limitation of the current GC column as the heaviest acid. The reaction results of hexanoic acid with different supports are presented in Table 4.1 below.

Table 4.1 Effect of support on the reaction of hexanoic acid with Cr-containing catalyst

Catalyst	Conversion of hexanoic acid	Selectivity to hexanal
1% CrOx/γ-Al_2O_3	<0.1%	/
1% CrOx/α-Al_2O_3	2.2%	83%

The reactivity of hexanoic acid over γ-Al_2O_3/α-Al_2O_3 is completely different. A 2.2% conversion of hexanoic acid was observed on α-Al_2O_3 supported chromium oxide, while less than 0.1% conversion was obtained with the 1% CrOx/γ-Al_2O_3. Yokoyama[11] found the same reaction trend over γ-Al_2O_3/α-Al_2O_3 supported chromium oxide with caprylic acid. From the difference in the UV-VIS spectra (Figure 4.1), it seems that the less reactivity over γ-Al_2O_3 is due to the Cr^{6+} centers, which was not observed in the α-Al_2O_3 supported catalyst. Therefore, the reaction was investigated with a focus on the α-Al_2O_3 supported catalyst and the effect of chromium loading was studied with the results shown in Table 4.2.

Table 4.2 Effect of Cr loading on the reaction of hexanoic acid with Cr-containing catalyst

Catalyst	Conversion of hexanoic acid	Selectivity to hexanal
1% CrOx/α-Al_2O_3	2.2%	83%
10% CrOx/α-Al_2O_3	4.9%	80%
20% CrOx/α-Al_2O_3	6.8%	78%

In the above table, the conversion of hexanoic acid increased from 2.2% to 6.8% when the loading of chromium was increased from 1% to 20% over α-Al_2O_3. At the same time, the selectivity to hexanal remained at the similar level of around 80%.

The UV-VIS spectra for these three materials (Figure 4.2) suggests that the more Cr^{3+} centers were formed with an increase of the chromium loading, as the intensity of the bands at 470 nm and 610 nm was increased. These Cr^{3+} centers were reported[25] to be the active sites for hydrogen dissociation and the generated oxygen vacancies are responsible for the adsorption of hexanoic acid and the following surface reaction. Since the reaction rates rely on the amount of Cr^{3+} centers, the reactivity was studied with unsupported chromium oxide calcined at different temperatures. Chromium nitrate is the precursor for the unsupported catalysts and the results are presented in Table 4.3.

Table 4.3 Effect of calcination temperature on the reaction of hexanoic acid with Cr-containing catalyst

Catalyst	Conversion of hexanoic acid	Selectivity to hexanal
CrOx calcined@573K	<1%	/
CrOx calcined@773K	7.9%	81%
CrOx calcined@973K	5.2%	73%
Cr_2O_3 bulk	22%	88%

Three different calcination temperatures of 573 K, 773 K, and 973 K were investigated in Table 4.3. Chromium oxide calcined at 573 K didn't show any reactivity with hexanoic acid, while the catalysts calcined at 773 K converted 7.9% hexanoic acid with 81% selectivity to hexanal. When the calcination temperature was increased to 973 K, the conversion decreased a little bit to 5.2 % and the selectivity to hexanal was 73%. As a comparison, Cr_2O_3 bulk material was tested as well, but interestingly it showed the best reactivity as a 22% conversion of hexanoic acid and 88% selectivity to hexanal was observed. During the thermal decomposition of chromium nitrate, the high oxidation state chromium species was formed first at low

temperature region (< 723 K) and these species were converted to thermal stable Cr_2O_3 when the temperature was further increased.[18] Similar to the findings in the Table 4.1, where the support has an effect of the surface chromium species, this results also shown that chromium with high oxidation state is not reactive, but the Cr^{3+} species are the active sites in this reaction. The decrease in hexanoic acid conversion when the calcination temperature was increased to 973 K is probably due to the dramatical decrease of the catalyst surface area.

As a result of high activity with hexanoic acid, Cr_2O_3 catalyst was further tested with a series of carboxylic acid from C2 – C6 acids and the results are listed in Table 4.4. All the reactions were carried out at 623 K and atmospheric pressure, with a 30 sccm flow of hydrogen and 0.1 mL h^{-1} flow of the acid.

Table 4.4 Reaction results of C2-C6 carboxylic acids on Cr_2O_3 catalyst

Carboxylic acid (C2-C6)	Conversion	Selectivity to aldehyde
Acetic acid	<1%	/
Propionic acid	20%	92%
Butyric acid	19%	89%
Valeric acid	20%	90%
Hexanoic acid	22%	88%

The results in Table 4.4 show that in general Cr_2O_3 catalyst can convert carboxylic acids to the corresponding aldehydes with about 90% selectivity at the given reaction condition, except that it is not reactive with acetic acid. According to Pestman,[10, 26] who studied the reactivity of acetic acid over a series of transition metal oxides, it showed the highest selectivity (80 %) over iron oxide to acetaldehyde at 593 K, while it is less reactive on chromium oxide and it only showed 8% selectivity to acetaldehyde even at 723 K. Ferrero[27] reported a 89% acetic acid

conversion and 59% acetaldehyde selectivity over Ru-Sn-B on alumina catalyst. However, it is interesting to investigate why Cr_2O_3 catalyst is not reactive with acetic acid, while it showed ~20% conversion and ~90% selectivity with C3 – C6 carboxylic acids. Further discussion will not be discussed in this chapter but are included in the future work.

Yokoyama and co-workers[11] reported that high purity Cr_2O_3 catalyst is very reactive with a variety of long chain aliphatic acids including octanoic acid, dodecanoic acid, octadecanoic acid, 9-octadecenoic acid, and cyclohexanecarboxylic acid. The conversions are all over 92% and the selectivity to corresponding aldehydes are over 95%.

4.4.2 Reaction Mechanism of Carboxylic Acids Hydrogenation

Barteau[24] reviewed the surface reaction of organic oxygenates on metal oxides, including the carboxylic acids. The molecular adsorption of carboxylic acid onto the metal oxide surface is via an acid-base type reaction, where the carboxylates species generated from the parent acid bind to the metal cation[23] or an oxygen vacancy generated through a removal of water[28] or surface fracture.[19] Yamagata reported that the intermediate carboxylates species were observed during the hydrogenation of 10-undecenoic acid over Cr_2O_3 catalyst.[13]

Pestman[10] reported a Mars and van Krevelen mechanism for the hydrogenation of acetic acid over iron oxides. The hydrogen is activated by metallic iron through spill-over and then migrates to oxygen surface to create oxygen vacancies by the removal of water. After the acetic acid adsorbs onto the oxygen vacancy with the oxygen in the carboxylate group binding to the iron cation, the carbonyl group gets attacked by the nearby hydrogen and desorbs the surface as acetaldehyde, with the

oxygen filling the vacancy. However with Cr_2O_3, whose redox activity is less compared to iron oxide, the hydrogen dissociation is completed on the Cr^{3+} center, while the remaining steps can be similar. Therefore, a reaction mechanism is proposed in Figure 4.9.

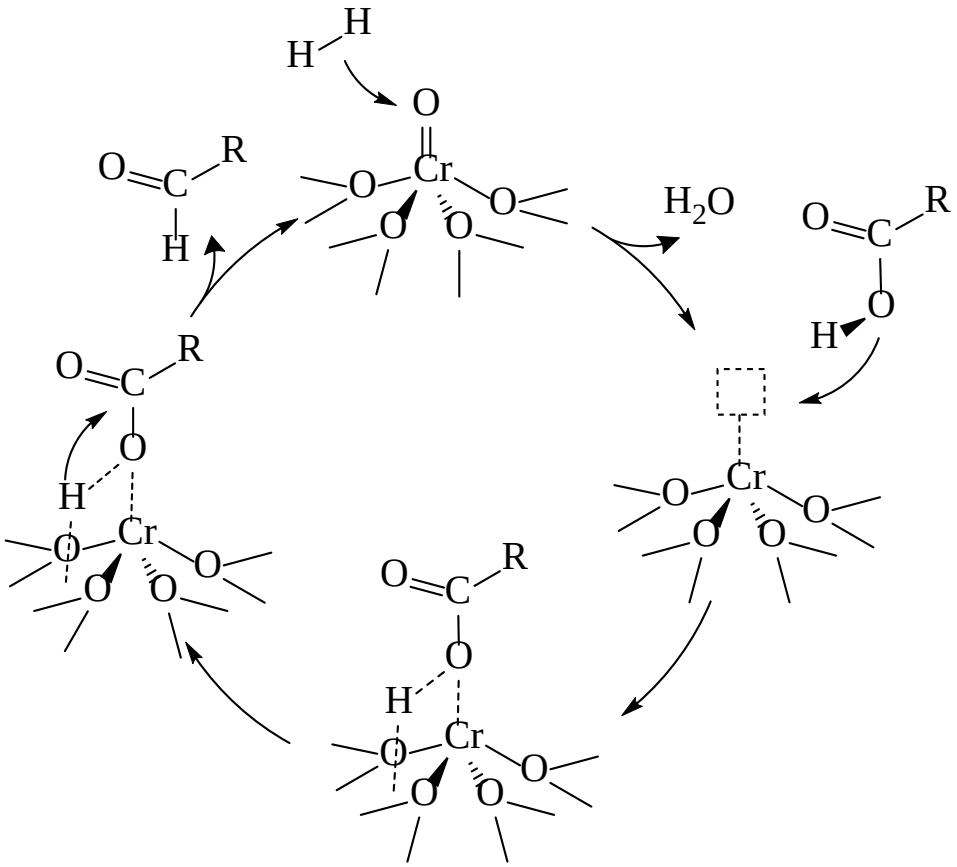

Figure 4.9 Proposed reaction mechanism of carboxylic acid on Cr_2O_3 surface

In general, the hypothesized reaction mechanism of carboxylic acid on Cr_2O_3 can be expressed as the following steps:

$$H_2 + 2\theta \overset{k0}{\leftrightarrow} 2H\theta \qquad \text{Eqn. 4.3}$$

$$2H\theta + O* \xrightarrow{k1} H_2O + 2\theta + * \quad \text{Eqn. 4.4}$$

$$RCOOH + * \xrightarrow{k2} RCOOH* \quad \text{Eqn. 4.5}$$

$$RCOOH* \xrightarrow{k3} RCHO + * \quad \text{Eqn. 4.6}$$

Where k_0 to k_3 are the rate constant, θ is the active site for hydrogen dissociation on Cr^{3+}, and * is the active site for the adsorption of carboxylate species.

With the above elementary steps, the production rate of the aldehyde [RCHO] can be expressed as:

$$r[RCHO] = k_3[RCOOH*] \quad \text{Eqn. 4.7}$$

Assuming the concentration change of reactive intermediates equal to zero, we can have the quasi-steady state assumptions (QSSA) below:

$$\frac{d[H\theta]}{dt} = 2k_{+0}[H_2][\theta]^2 - 2k_{-0}[H\theta]^2 - 2k_1[H\theta]^2[O*] = 0 \quad \text{Eqn. 4.8}$$

$$\frac{d[O*]}{dt} = -2k_1[H\theta]^2[O*] + k_3[RCOOH*] = 0 \quad \text{Eqn. 4.9}$$

$$\frac{d[RCOOH*]}{dt} = k_2[RCOOH][*] - k_3[RCOOH*] = 0 \quad \text{Eqn. 4.10}$$

The sum of each type of active site concentrations should be equals to 1 and we have the following equations:

$$[\theta] + [H\theta] = 1 \quad \text{Eqn. 4.11}$$

$$[*] + [O*] + [RCOOH*] = 1 \quad \text{Eqn. 4.12}$$

By solving the equations above (Eqn. 4.8 – 4.12),

$$r[RCOOH*] = \frac{k_1k_2}{k_1k_2 + k_2k_3 + k_1k_3\frac{1}{[RCOOH]} + k_2k_3\frac{k_{-0}}{k_{+0}[H_2]}} \quad \text{Eqn. 4.13}$$

Substitute the result into Eqn. 4.7, and the production rate of aldehyde can be express as:

$$r[RCHO] = \frac{k_1 k_2 k_3}{k_1 k_2 + k_2 k_3 + k_1 k_3 \frac{1}{[RCOOH]} + k_2 k_3 \frac{k_{-0}}{k_{+0}[H_2]}} \qquad \text{Eqn. 4.14}$$

For any given concentration of the acid ([RCOOH] = constant), if the partial pressure of hydrogen is decreased to half of its original value,

$$[H_2]' = 0.5[H_2] \qquad \text{Eqn. 4.15}$$

Then the new production rate of aldehyde can be expressed as,

$$r[RCHO]' = \frac{k_1 k_2 k_3}{k_1 k_2 + k_2 k_3 + k_1 k_3 \frac{1}{[RCOOH]} + k_2 k_3 \frac{k_{-0}}{k_{+0} * 0.5[H_2]}} \qquad \text{Eqn. 4.16}$$

$$= \frac{k_1 k_2 k_3}{k_1 k_2 + k_2 k_3 + k_1 k_3 \frac{1}{[RCOOH]} + 2 k_2 k_3 \frac{k_{-0}}{k_{+0}[H_2]}} \qquad \text{Eqn. 4.17}$$

When compared to the original production rate, the new rate should be greater than half the original rate, but less than the original rate.

$$0.5\, r[RCHO] < r[RCHO]' < r[RCHO]$$

Figure 4.10 shows the experimental result from propionic acid reaction over Cr_2O_3. In the experiment, the partial pressure of hydrogen was decreased to half by introducing an inert nitrogen gas while keeping the total gas flow rate constant, after a 3-hour run with pure hydrogen environment. As a result, the production rate of propanal was decreased from 4.9 to 2.7 mmol h^{-1} g_{cat}^{-1}, which is consistent with the rate expression derived from the mechanism.

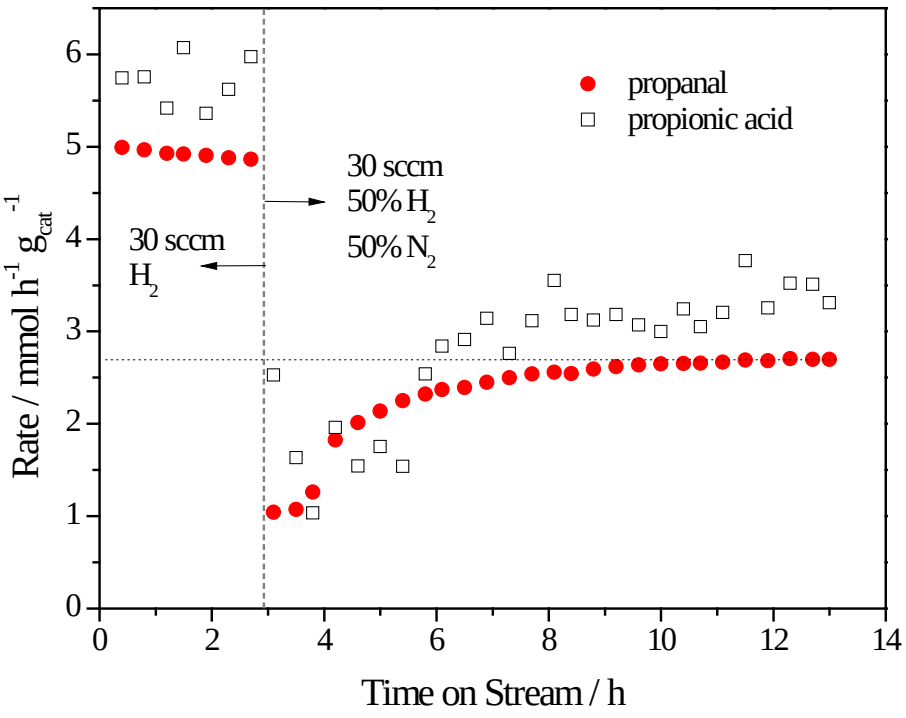

Figure 4.10 Effect of hydrogen partial pressure on the reaction rates

The same analysis can be applied to the acid as well. If the partial pressure of hydrogen is kept as constant, while the partial pressure of the acid is decreased to half of its original value, the production rate of aldehyde should also lay between half the original value and the original rate. Figure 4.11 presents the result of such analysis, where the production rate of propanal was decreased from 4.9 to 4.0 mmol h^{-1} g_{cat}^{-1}.

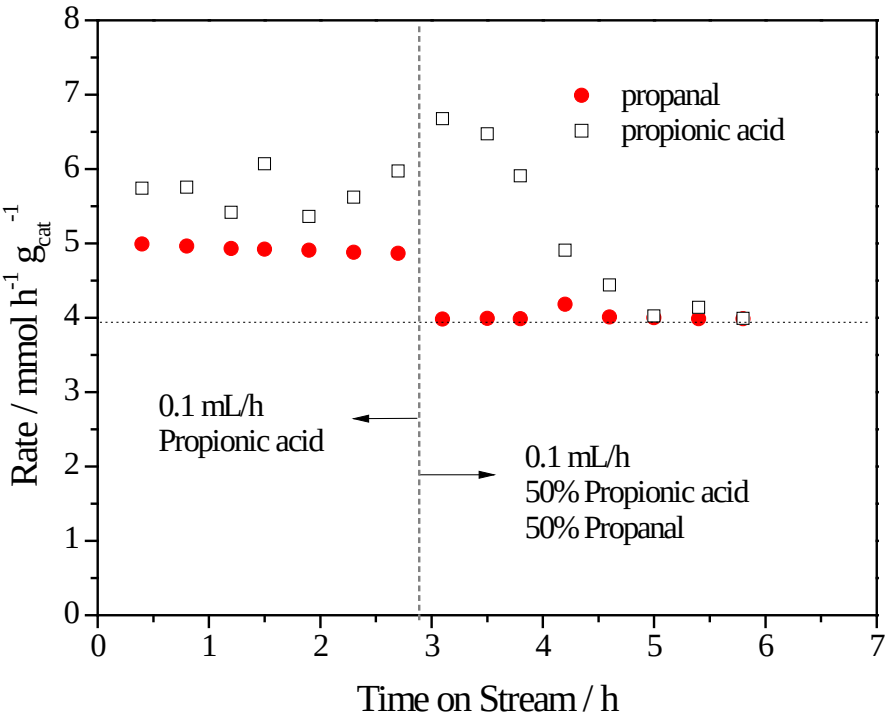

Figure 4.11 Effect of propionic acid partial pressure on the reaction rates

4.5 Conclusion

The hydrogenation of carboxylic acids to the corresponding aldehydes is investigated in this chapter with Cr_2O_3 catalyst. The reactivity of Cr_2O_3 catalyst has been tested with a series of carboxylic acids including C2 – C6 acids. Expect for acetic acid, the catalyst showed an overall 20% conversion of the other acids (C3 – C6) and ~90% selectivity to the aldehydes. For the alumina supported chromium oxide, it is less reactive when compared to bulk Cr_2O_3 catalyst. UV-VIS results showed that lower chromium loading favors the formation of higher oxidation states chromium species, which is not reactive for the hydrogenation of carboxylic acid. The hydrogen

dissociation on the Cr_2O_3 catalyst was studies with H_2-D_2 scrambling experiment and further discussed. The hydrogen can dissociate onto the Cr_2O_3 catalyst and a fast equilibrium of H_2-D_2 exchange reaction was reached at room temperature. The adsorption of carboxylic acid on Cr_2O_3 catalyst is completed via an acid-base type reaction, when the conjugate carboxylate species from the parent acid binding to the chromium cation. This adsorption mechanism is consistent with the deuterium labeling reaction result. Finally, the overall reaction mechanism is discussed through a Mar and van Krevelen type mechanism and the rate of aldehyde is expressed as a function of carboxylic acid and hydrogen. The results of varying the reactants concentration are consistent with the rate expression, where less than first order of both reactants is determined.

REFERENCES

[1] D. Bezier, S. Park, M. Brookhart, Selective Reduction of Carboxylic Acids to Aldehydes Catalyzed by B(C6F5)(3), Organic Letters, 15 (2013) 496-499.

[2] N. Murali, K. Srinivas, B.K. Ahring, Biochemical Production and Separation of Carboxylic Acids for Biorefinery Applications, Fermentation, 3 (2017) 22.

[3] W. Riemenschneider, Carboxylic Acids, Aliphatic, in: Ullmann's Encyclopedia of Industrial Chemistry, 2000.

[4] L. Fabre, P. Gallezot, A. Perrard, Catalytic hydrogenation of arabinonic acid and lactones to arabitol, Journal of Catalysis, 208 (2002) 247-254.

[5] H.G. Manyar, C. Paun, R. Pilus, D.W. Rooney, J.M. Thompson, C. Hardacre, Highly selective and efficient hydrogenation of carboxylic acids to alcohols using titania supported Pt catalysts, Chemical Communications, 46 (2010) 6279-6281.

[6] R.D. Cortright, M. Sanchez-Castillo, J.A. Dumesic, Conversion of biomass to 1,2-propanediol by selective catalytic hydrogenation of lactic acid over silica-supported copper, Applied Catalysis B-Environmental, 39 (2002) 353-359.

[7] C.S. Spanjers, D.K. Schneiderman, J.Z. Wang, J. Wang, M.A. Hillmyer, K. Zhang, P.J. Dauenhauer, Branched Diol Monomers from the Sequential Hydrogenation of Renewable Carboxylic Acids, Chemcatchem, 8 (2016) 3031-3035.

[8] M. Kitson, P.S. Williams, Alcohols production by hydrogenation of carboxylic acids, in, 1988.

[9] E.J. Grootendorst, R. Pestman, R.M. Koster, V. Ponec, SELECTIVE REDUCTION OF ACETIC-ACID TO ACETALDEHYDE ON IRON-OXIDES, Journal of Catalysis, 148 (1994) 261-269.

[10] R. Pestman, R.M. Koster, J.A.Z. Pieterse, V. Ponec, Reactions of carboxylic acids on oxides .1. Selective hydrogenation of acetic acid to acetaldehyde, Journal of Catalysis, 168 (1997) 255-264.

[11] T. Yokoyama, N. Fujita, Hydrogenation of aliphatic carboxylic acids to corresponding aldehydes over Cr2O3-based catalysts, Applied Catalysis a-General, 276 (2004) 179-185.

[12] T. Yokoyama, N. Yamagata, Hydrogenation of carboxylic acids to the corresponding aldehydes, Applied Catalysis a-General, 221 (2001) 227-239.

[13] N. Yamagata, T. Yokoyama, T. Maki, Direct hydrogenation of aliphatic carboxylic acids to corresponding aldehydes with Cr2O3 catalyst, Studies in Surface Science and Catalysis, 121 (1999) 441-444.

[14] F. Cavani, M. Koutyrev, F. Trifiro, A. Bartolini, D. Ghisletti, R. Iezzi, A. Santucci, G. DelPiero, Chemical and physical characterization of alumina-supported chromia-based catalysts and their activity in dehydrogenation of isobutane, Journal of Catalysis, 158 (1996) 236-250.

[15] Z.G. Szabo, K. Kamaras, S. Szebeni, I. Ruff, INVESTIGATION OF CHROMATE SALTS BY DIFFUSE REFLECTANCE SPECTROSCOPY, Spectrochimica Acta Part a-Molecular and Biomolecular Spectroscopy, 34 (1978) 607-612.

[16] M. Cherian, M.S. Rao, W.T. Yang, H.M. Jehng, A.M. Hirt, G. Deo, Oxidative dehydrogenation of propane over Cr2O3/Al2O3 and Cr2O3 catalysts: effects of loading, precursor and surface area, Applied Catalysis a-General, 233 (2002) 21-33.

[17] B.M. Weckhuysen, I.E. Wachs, R.A. Schoonheydt, Surface chemistry and spectroscopy of chromium in inorganic oxides, Chemical Reviews, 96 (1996) 3327-3349.

[18] A. Malecki, B. Malecka, R. Gajerski, S. Labus, Thermal decomposition of chromium(III) nitrate(V) nanohydrate - Different chromium oxides CrO1.5+y formation, Journal of Thermal Analysis and Calorimetry, 72 (2003) 135-144.

[19] P.W. Selwood, SITES ACTIVE FOR CATALYTIC HYDROGEN-DEUTERIUM EQUILIBRATION OVER ALPHA-CHROMIA, Journal of the American Chemical Society, 92 (1970) 39-&.

[20] D.A. Dowden, D. Wells, Actes du deuxième Congrès international de catalyse, Paris, 1960.

[21] J. Rasko, J. Kiss, Adsorption and surface reactions of acetaldehyde on TiO2, CeO2 and Al2O3, Applied Catalysis a-General, 287 (2005) 252-260.

[22] T.L. Chen, D.R. Mullins, Adsorption and Reaction of Acetaldehyde over CeOX(111) Thin Films, Journal of Physical Chemistry C, 115 (2011) 3385-3392.

[23] J.M. Vohs, Site Requirements for the Adsorption and Reaction of Oxygenates on Metal Oxide Surfaces, Chemical Reviews, 113 (2013) 4136-4163.

[24] M.A. Barteau, Organic reactions at well-defined oxide surfaces, Chemical Reviews, 96 (1996) 1413-1430.

[25] R.L. Burwell, J.F. Read, K.C. Taylor, G.L. Haller, ADSORPTIVE AND CATALYTIC PROPERTIES OF CHROMIA, Zeitschrift Fur Physikalische Chemie-Frankfurt, 64 (1969) 18-&.

[26] R. Pestman, R.M. Koster, V. Ponec, SELECTIVE HYDROGENATION OF ACETIC-ACID TOWARDS ACETALDEHYDE, Recueil Des Travaux Chimiques Des Pays-Bas-Journal of the Royal Netherlands Chemical Society, 113 (1994) 426-430.

[27] Ferrero, Ru-Sn-B on alumina catalysts for hydrogenation of a wide variety of carboxylic acids to aldehydes, in: E.P. Application (Ed.), 1993.

[28] R. Pestman, R.M. Koster, E. Boellaard, A.M. van der Kraan, V. Ponec, Identification of the active sites in the selective hydrogenation of acetic acid to acetaldehyde on iron oxide catalysts, Journal of Catalysis, 174 (1998) 142-152.

Chapter 5

NON-OXIDATIVE METHANE COUPLING TO ETHYLENE USING Mo_2C/[B]ZSM-5

5.1 Introduction

Effective utilization of methane is of great interest and importance to the chemical industry because of the rapid growth of shale gas production and the low cost of this raw material.[1] The conversion of methane to higher hydrocarbons can be categorized into indirect methods and direct methods. Indirect methods use carbon monoxide and hydrogen—produced via methane steam reforming, carbon dioxide reforming, or partial oxidation—as intermediates.[2] Direct methods involve methane coupling with or without the presence of an oxidant, known respectively as oxidative coupling of methane (OCM) and non-oxidative coupling of methane (NCM).[3]

One of the methane coupling products is ethylene and according to a PwC(PricewaterhouseCoopers) report, the capital cost of ethylene produced using NCM is estimate as $316/ton, while the current ethylene price from crude oil steam cracking is $1717/ton.[4] Non-oxidative coupling of methane to ethylene is thus a promising alternative to generate a carbon stream that can be fed directly into the existing structure of the chemical industry, with potentially less than one fifth of the current cost.

Wang and co-workers pioneered non-oxidative methane dehydroaromatization reaction on Mo/ZSM-5.[5] It is reported that only 1.4% of methane was fully converted to benzene at 973 K on HZSM-5 catalysts. A higher conversion of 7.2%

was achieved in the presence of Mo in the sample.[5] An induction period was observed with MoO_3/HZSM-5, implying that the actual active phase was formed in-situ from the MoO_3/HZSM-5 starting material.[6, 7] Further research has revealed that the primary reaction of C–H bond dissociation occurs on Mo_2C nanoparticle surface.[8] At the surface, a molybdenum-carbene-like intermediate, CH_2=Mo, is involved in the proposed mechanism. Ethylene is believed to be the primary product from the coupling of the surface carbene species in these samples.[8, 9] Ethylene oligomerization reactions take place simultaneously leading to the formation of aromatics species, the thermodynamically favored products at the high reaction temperature.[10] The formation of aromatics is catalyzed by Brønsted acid sites in the zeolite pores and the material operates as a bi-functional catalysts.[11]

The acidic OH groups of the zeolite catalyst, however, also promote coke formation and fast catalyst deactivation at high temperature.[12] By removal of external acid sites[13] or of part of the framework aluminum,[14] the catalyst activity and stability can be significantly improved. In the rich literature of methane aromatization to benzene, the selectivity of ethylene has not been investigated in much detail. Considering the nature of the bi-functional Mo/HZSM-5 catalysts, one may assume that ethylene could be selectively produced solely on molybdenum carbide, where the methane C–H bond dissociation and coupling reactions occur. However, unsupported Mo_2C shows very limited methane reactivity (0.1 ~ 0.3% conversion), has poor selectivity (hydrogen, carbon, and a minor amount of ethane are produced), and suffers from fast deactivation.[10] In contrast, in this chapter an investigation of methane coupling to ethylene on molybdenum carbide nanoparticles supported on non-acidic [B]ZSM-5 is described. Different from Mo_2C/[Al]ZSM-5 catalysts for

methane aromatization reaction, this material exhibits very high ethylene selectivity (>90%) instead of producing aromatics (benzene and naphthalene). Due to the low acidity of the zeolite support, the stability of the catalyst is also greatly improved with a deactivation rate of less than 0.5% h^{-1} during an 18 h reaction test period, while Mo_2C/[Al]ZSM-5 usually deactivates within a few hours.[11]

5.2 Experimental Section

5.2.1 Catalyst Preparation

[B]ZSM-5 was synthesized by the hydrothermal method using tetrapropylammonium bromide (TPABr) as the organic structure director. Fumed silica was used as the silica source and boric acid as the boron source. After calcination and NH_4^+ ion exchange, 2% ammonium heptamolybdate was impregnated onto the zeolite support. Before reaction, the catalyst was calcined at 773 K and carburized at 973 K.

5.2.2 Catalyst Evaluation

The catalyst was evaluated in a quarter inch quartz tube reactor. Typically, 50 mg of sample will be loaded into the reactor between two layers of quartz wool. The reactor was installed in a flow reactor system, which also includes a gas flow system, a heating system, and products analysis system. Multiple gases can be fed using Brooks mass flow controller E5850. The quartz reactor is heated by a furnace and the gas lines after the reactor are properly wrapped with heating tapes. An online gas chromatography (GC, Shimadzu 2014) and a mass spectroscopy (Pfeiffer, Thermostar GSD 320T) are employed to collect and analyse the products.

5.2.3 X-ray Diffraction (XRD) and Transmission Electron Microscopy (TEM)

XRD analysis were performed using Bruker D8 x-ray powder diffractometer with monochromatic Cu Kα1 line (k = 1.540 Å). TEM image was obtained by a JEM-2010F. N_2 adsorption experiments were performed with 3Flex surface characterization analyzer. BET Surfaces were calculated using the MicroActive for 3Flex software.

5.2.4 UV-VIS Spectroscopy

Diffused reflectance UV-VIS study was carried out using a flow cell and a Jasco V550 UV-VIS spectroscopy. The in-situ flow cell is made of U-shaped quartz round tube with a UV window made of square quartz tube (Quartz Plus, Inc.). Typically, 100 mg of the catalyst sample was loaded into the flow cell at the window. Other auxiliary systems (a heating system and gas flow control system) are included to perform the in-situ UV-VIS study. All the spectra were taken at room temperature with inert gas flowing through the sample bed.

5.2.5 Temperature Programmed Oxidation (TPO)

TPO experiment was conducted with the quartz reactor as mentioned in section 2.0. About 100 mg of the calcined catalyst was loaded into the reactor and a carburization was performed before the TPO experiment. After the catalyst bed was cooled down to room temperature in He flow, a 20% O2/He gas was introduced with a ramping rate of 10 K/min until 823 K. The gas products were collected and analysed by a mass spectroscopy (Pfeiffer, Thermostar GSD 320T).

5.2.6 X-ray Absorption Spectroscopy (XAS)

In-situ XAS studies were carried out in Argonne National Lab (ANL) at beamline 11B.The impregnated 2% wt. Mo/[B]ZSM-5 was loaded into an in-situ

reaction cell.[15] The sample was first calcined at 773 K and then carburized with 20% CH_4/H_2 at 973 K. Full EXAFS spectra were taken at the beginning and the end of each process. XANES spectra were taken every 5 min during the in-situ treatment.

5.2.7 In situ Fourier Transform Infrared (FT-IR) Characterization

The FT-IR measurements were performed using an in situ diffused reflectance infrared Fourier transform (DRIFT) cell with ZnSe windows (15 x 2 mm, Harrick Sci.). The IR cell consists of a cell body, sample holder and aluminium heating block. About 50 mg of the catalyst sample was required to load into the sample holder as a pellet. Proper gases could be fed through the sample by mass flow controllers (Brooks 5850E series). IR spectra were collected using a Fourier transform infrared spectrometer (Nicolet Nexus 470). The IR spectral data were analysed by OMNIC software. The catalyst sample was pre-treated with He at 773 K (5 K/min ramping rate) for 4 hours to remove moisture and other surface contaminates. After cooling down to room temperature, IR spectra were collected in He flow.

5.3 Results and Discussion

5.3.1 Zeolite Characterization

[B]ZSM-5 was synthesized under hydrothermal crystallization conditions at 423 K for three days using fumed silica, boric acid, sodium hydroxide, and tetrapropylammonium bromide (TPABr) as starting materials. After calcination at 823 K and NH_4^+ ion exchange (in triplicate), the zeolite was submitted for Inductively Coupled Plasma (ICP) measurements to quantify composition. A high Si/B ratio of 70 is obtained by this technique. 2% of Mo is introduced to the zeolite by wetness impregnation. The impregnated sample is then calcined in air at 823 K for 4 h. Before

the methane reaction, the calcined sample is carburized in 20% CH_4/H_2 at 923K (detailed information can be found below). Different types of characterization techniques were applied to the above four samples, namely [B]ZSM-5, impregnated, calcined, and carburized 2% Mo/[B]ZSM-5.

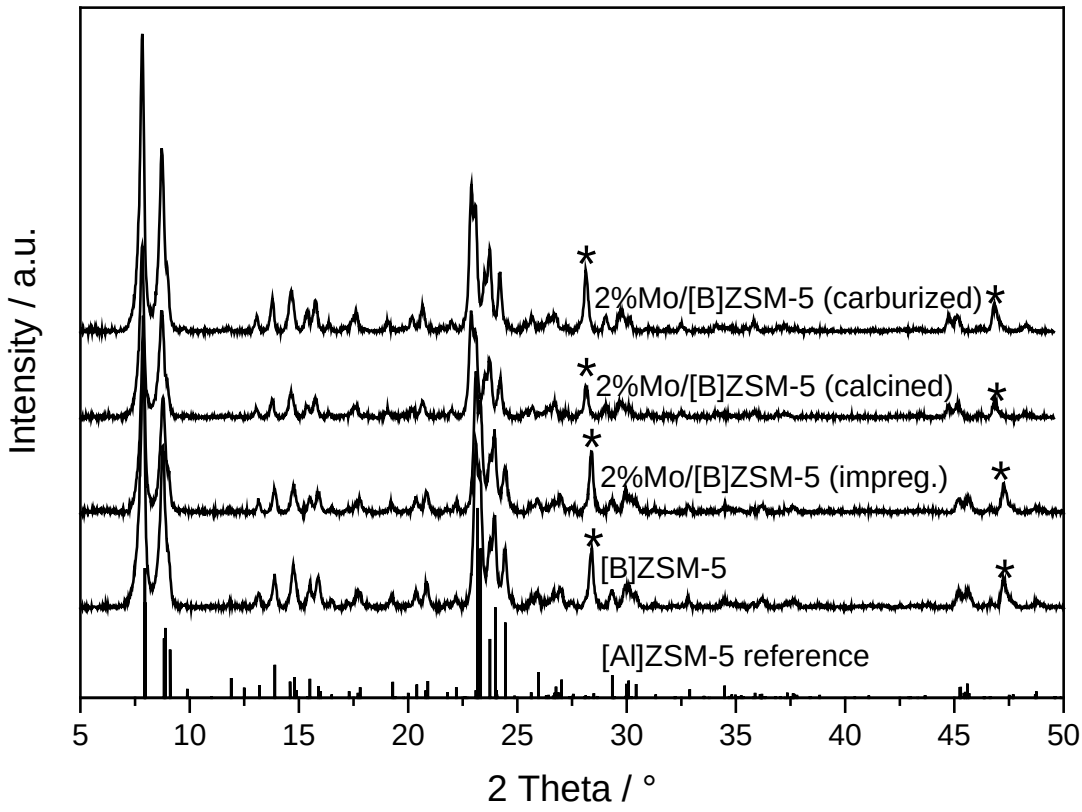

Figure 5.1 XRD patterns of Mo/[B]ZSM-5 (Peaks marked are from 10% wt. Si internal standard), [Al]ZSM-5 reference: $H_{0.32}(Si_{95.68}Al_{0.32}O_{192})$[16]

As shown in Figure 5.1, the X-ray powder diffraction patterns of the synthesized B-containing MFI-type zeolites samples have a well-defined diffraction

pattern consistent with the formation of the pure MFI-type structure. There is no evidence for the presence of any amorphous material in any of the samples. Furthermore, in all the 2% Mo/[B]ZSM-5 samples, the peak positions are slightly shifted towards lower angles as compared to silicalite, which indicates a decrease of the unit cell dimensions of the boron-containing zeolite upon impregnation and calcination of the Mo precursor. This is consistent with the small size of B with respect to Si. No diffraction peaks for molybdenum oxides are observed in any of the samples ruling out the formation of (detectable) large Mo particles in the exterior of the zeolite crystals. This is likely due to the low Mo loading and is an indication of good dispersion of the Mo precursors before and after the experiments.

To measure accurately the zeolite unit cell volume, 10 wt.% of pure Si powder was mixed with each sample and used as internal standard.[17] Calculated unit cell volumes and u.c. parameters are listed in Table 1. This table shows that zeolite unit cell expanded after the calcination and carburization steps, indicating the loss of framework boron during both reactions. Deboronation is facilitated at the high temperature range and in the presence of water generated in both calcination and caburization steps. Unlike dealumination in aluminosilicate zeolite, boron can be removed from the framework even under mild conditions (e.g. stirring in water at room temperature), an in the presence of high temperatures and water vapor this process is accelerated.[18] The amount of framework B can be estimated on the basis of the size of the unit cell because unit cell dimensions are linearly correlated with the unit cell volume.[19, 20] According to the published correlation,[20] the as-made zeolite B-MFI sample contained about 2.5 boron atoms per unit cell, this number

decreased to 1.7 after calcination and decreased further to 1 per unit cell after carburization.

Table 5.1 Unit cell volume (UCV) and parameters of 2% Mo/[B]ZSM-5

parameter	UCV / $Å^3$	a / Å	b / Å	c / Å
[B]ZSM-5	5322	19.853	20.067	13.360
2%Mo/[B]ZSM-5 (impregnated)	5323	19.845	20.080	13.357
2%Mo/[B]ZSM-5 (calcined)	5337	19.847	20.087	13.387
2%Mo/[B]ZSM-5 (carburized)	5350	19.904	20.094	13.378

Textural and micropore volume estimates of the catalyst were measured using N_2 adsorption isotherms (Table 2). Both BET surface area and the micropore volume decreased after Mo was loaded onto the zeolite, suggesting that the Mo species are entering the channels of the zeolite in this step.

Table 5.2 BET surface areas and micropore volumes of 2% Mo/[B]ZSM-5

Material	BET surface area m^2/g	Micropore volume cm^3/g
[B]ZSM-5	403.8	0.136
2%Mo/[B]ZSM-5 (impregnated)	391.1	0.112
2%Mo/[B]ZSM-5 (calcined)	358.5	0.101
2%Mo/[B]ZSM-5 (carburized)	337.5	0.099

5.3.2 In-situ UV-VIS Study on the Molybdenum Species

We carried out an in-situ UV-VIS investigation of molybdenum oxides particles formed in the samples upon impregnation and calcination. Oxomolybedenum species can give strong absorption bands in the UV-VIS region due to the ligand-to-metal charge transfer ($O^{2-} \rightarrow Mo^{6+}$).[21] The bands are usually relatively narrow and can be observed between 200 and 400 nm due to the nature of π to π* charge-transfer transition.[22] For the ligand-to-metal charge transfer, the energy of the electronic transitions have a strong dependence on the ligand field symmetry surrounding the molybdenum center. In this work for oxo-ligands, a more energetic transition is expected for tetrahedral Mo(VI) than for octahedral Mo(VI).[22] Therefore in the literature, most bands for pure tetrahedral oxomolybdenum were reported at 260-280 nm, while bands for pure octahedral oxomolybdenum were observed at 300-320 nm.[23]

In Figure 5.2, a broad band around 250-350 nm with a shoulder at 235 nm was observed for the impregnated Mo/[B]ZSM-5, while after a calcination a sharp band at 260 nm with a shoulder at 235 nm was formed. The broad band can be considered as the overlapping of the bands at 260-280 nm and 300-320 nm, suggesting the fact of polymeric structure of both tetrahedral and octahedral molybdenum centers of the supported oxomolybdate species.[24] Since the precursor $(NH_4)_6Mo_7O_{24}$ is only composed of 7 MoO_6 octahedra linked by sharing oxo-edges, we believe the tetrahedral molybdenum centers are formed during the impregnation and the drying steps, since the blue shift of the absorption bands is also reported during the impregnation step in other metal oxide catalysts due to the near surface pH changes.[25] After a calcination, the material presents two bands at 235 nm and 260 nm, implying the formation of tetrahedral molybdednum centers and the

disappearance of octahedral centers. In fact these two bands are very typically observed for $CaMoO_4$ or Na_2MoO_4, where MoO_4^{2-} anions are isolated from each other either by Ca^{2+} or Na^{+}.[26]

The UV-VIS spectra of Mo/[Al]ZSM-5 are also very well studied in the literature by other authors. Vasenin et al.[27] reported a band at 330 nm for the initial 10% Mo/[Al]ZSM-5 after drying 373K and assign the band to the precursor $(NH_4)_6Mo_7O_{24}$. Martinez and Peris[28] only observed bands at 220-250 nm for the calcined 3% Mo/[Al]ZSM-5 catalyst, indicating the molybdenum mainly exists as highly dispersed tetrahedral oxomolybdate species. Ngobeni et al.[29] also reported the bands at 220-250 nm for 2% Mo/[Al]ZSM-5 and found the addition of boron or silver as dopants does not influence the coordination sphere of molybdenum species.

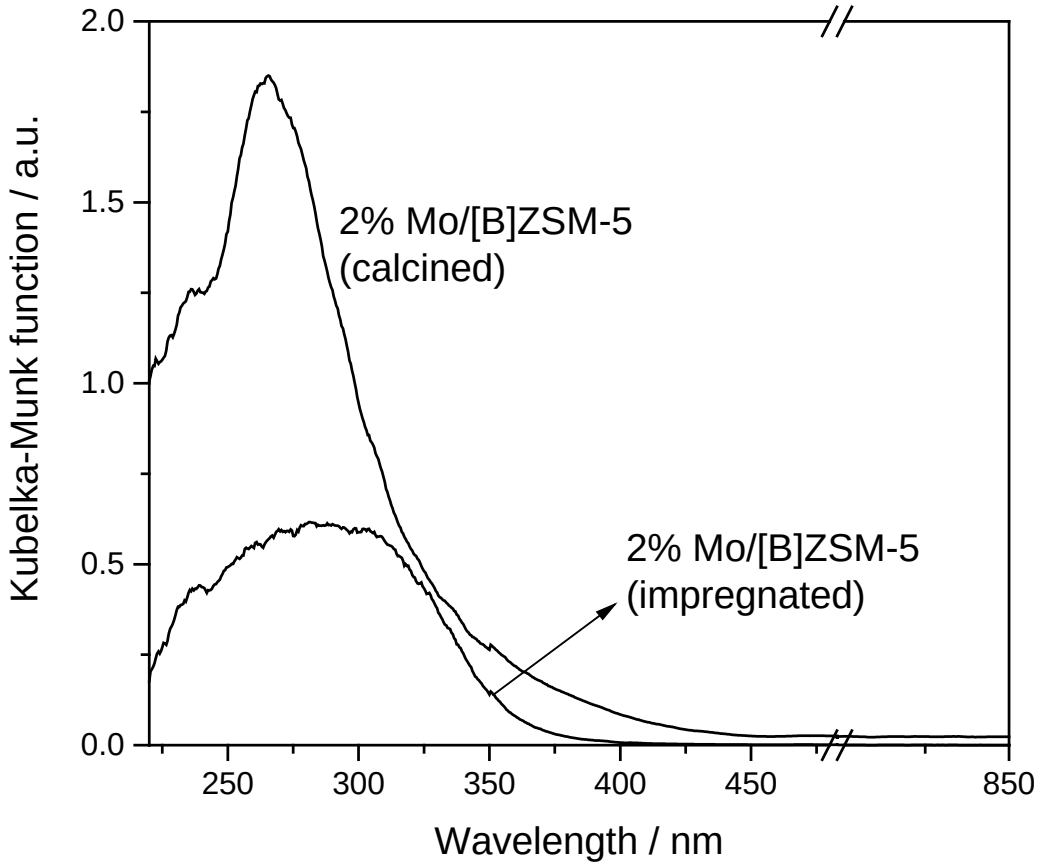

Figure 5.2 UV-VIS diffused reflectance spectra of 2%Mo/[B]ZSM-5

As the narrowing and the blue shift of the band are observed when there is a decrease of the oxomolybdates cluster size or the counter-cation numbers,[24] the UV-VIS spectra suggest that the surface oxomolybdates speices has been well dispersed and anchored onto the zeolite support, but how small the cluster is remains unclear. Weber[30] reported that the average number of adjacent molybdenum cations in very small oxide clusters is linearly correlated with the optical band gap energy of the bulk oxide, and this property can be readily determined using UV-VIS spectroscopy (Figure 5.3). According to the correlation the polyoxomolybdates turn into

mono/binuclear molybdenum oxides after calcination implying not only that the molybdenum migrates into the zeolite pores but also that these species are anchored onto the silanol groups and/or the weak Brønsted acid boron sites.

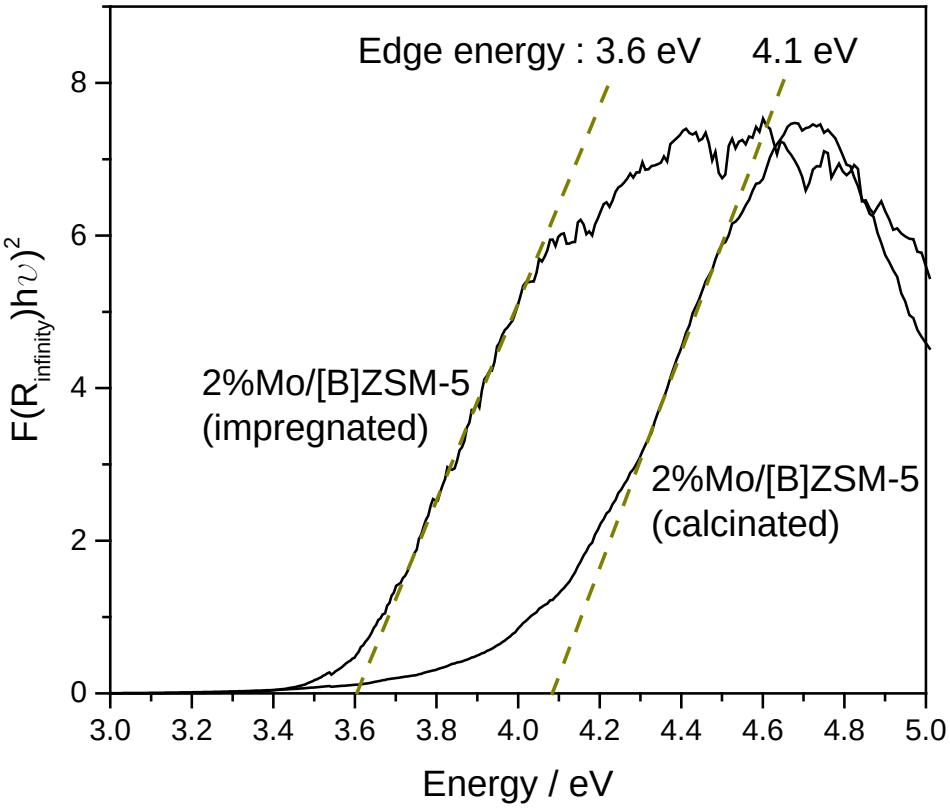

Figure 5.3 UV-VIS edge energies of 2%Mo/[B]ZSM-5

5.3.3 Investigation on the Molybdenum Carbides

After the formation of mono/binuclear molybdenum oxides, the samples were carburization in a flow of 20% CH_4/H_2 (20 sccm) at 973 K for 8 h. A temperature programmed oxidation experiment (TPO) was carried out on these samples to quantify

the ratio of Mo and carbon after the carburization step (Figure 5.4). The trace with negative values depicts the consumption of O_2 and the positive signals are due to the generation of CO and CO_2. At the beginning of the experiment, in the low temperature regime (400-600 K), CO is the favored oxidation product and as the temperature increased (700-823 K), CO_2 exceeded the CO produced to become the main product. However Ding et al.[8] reported that the reoxidation of the 4% Mo_2C/[Al]ZSM-5 occurs as a single fast process with sharp evolutions of both CO and CO_2 at about 725 K. For bulk Mo_2C the CO_x evolution temperature is even higher at about 1000 K.[8] The lowest CO_x evolution temperature suggests the best reactivity and oxygen dissociation ability of the Mo_2C/[B]ZSM-5. In addition, by comparing the oxygen consumed by carbon and by molybdenum, a Mo/C ratio of 1.9 was estimated, indicating the carburization process was almost completed with all the oxides turning into carbides.

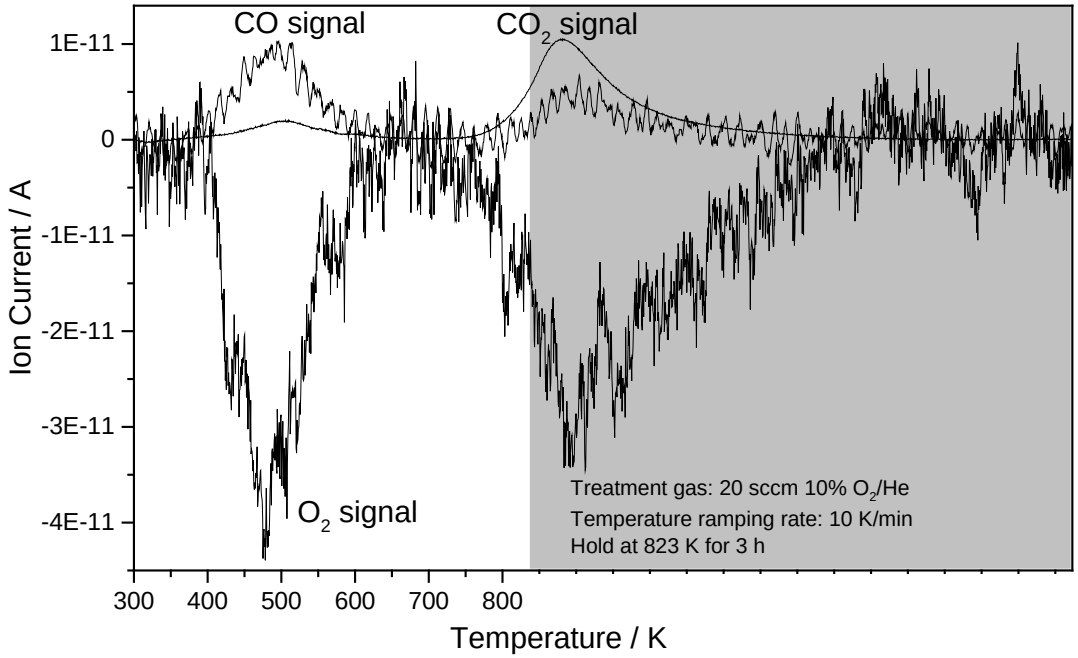

Figure 5.4 Temperature programmed oxidation of carburized 2% Mo/[B]ZSM-5

A transmission electron microscope (TEM) image of the carburized 2% Mo/[B]ZSM-5 is shown in Figure 5.5. In the image, black dots less than 1 nm in diameter can be identified inside as the well dispersed Mo_2C particles. However a few larger particles around 2 nm are also observed. This can be explained by the "knock-on" effect observed during the electron beam irradiation, where the Mo_2C particles are squeezed out from the zeolite channel to the external surface.

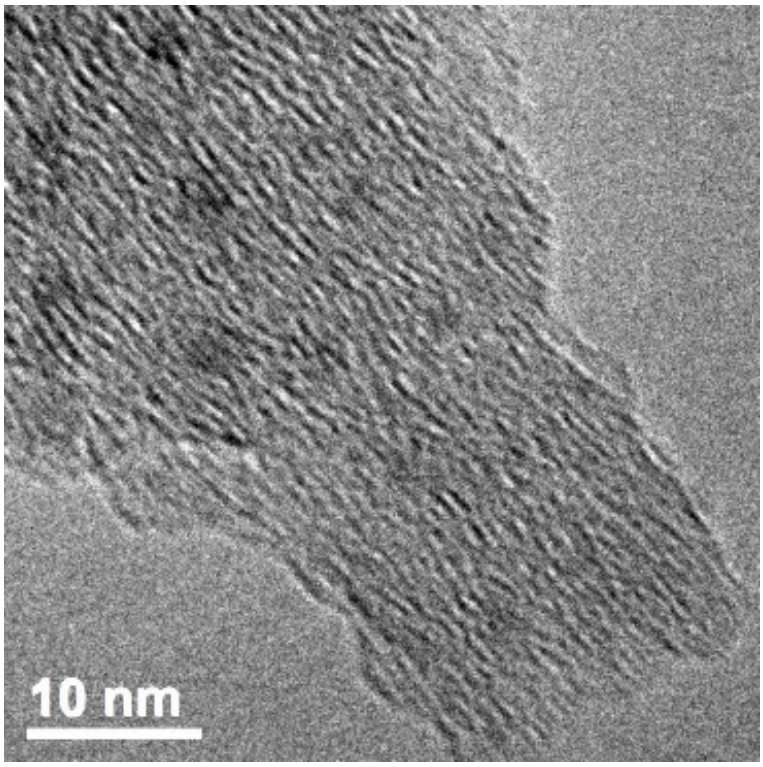

Figure 5.5 TEM image of 2% Mo/[B]ZSM-5 after carburization

5.3.4 In-situ X-ray Absorption Spectroscopy Study

The structural coordination and electronic state of Mo can be described with in-situ X-ray absorption fine structure (XAFS) spectroscopy during the carburization process. The Mo K-edge X-ray absorption near edge structure (XANES) was recorded and is shown in (Figure 5.6). A three-step K-edge feature change was observed during the carburization: The first step (upper left) was performed ramping the temperature from 298 K to 723 K at a rate of 2 K/min. Growth of the pre-edge feature was observed, that is, there is an increase of the tetrahedral symmetry of the Mo center.[31] During the second step (upper right), when the temperature was increased to 923 K at 1 K/min, a plateau was reached with no major structure change. In the third step

(lower left) the pre-edge feature became less and less intense as the temperature was increased to 973 K at 1 K/min. The disappearance of the pre-edge absorption feature - indicates that the Mo(VI)-oxo species were reduced and carbidic Mo species are formed.[8, 32] The spectra did not change further at 973 K. The lower right figure shows the overall change of the K-edge through the whole carburization process. The Mo-K absorption edge shifts to lower energies (ΔE = 4.5 eV) during the carburization process, and the ΔE is about 5 eV with Mo/[Al]ZSM-5 according to Ding et al.[8] The final oxidation state of the Mo was close to the oxidation state of Mo in Mo_2C, suggesting that the sample contains a mixture of molybdenum carbide and molybdenum oxycarbide. This result is consistent with other XANES analysis during the carburization process of Mo/[Al]ZSM-5, where Mo center is anchored either onto the silanol groups and/or Brønsted acid aluminum sites.[33, 34]

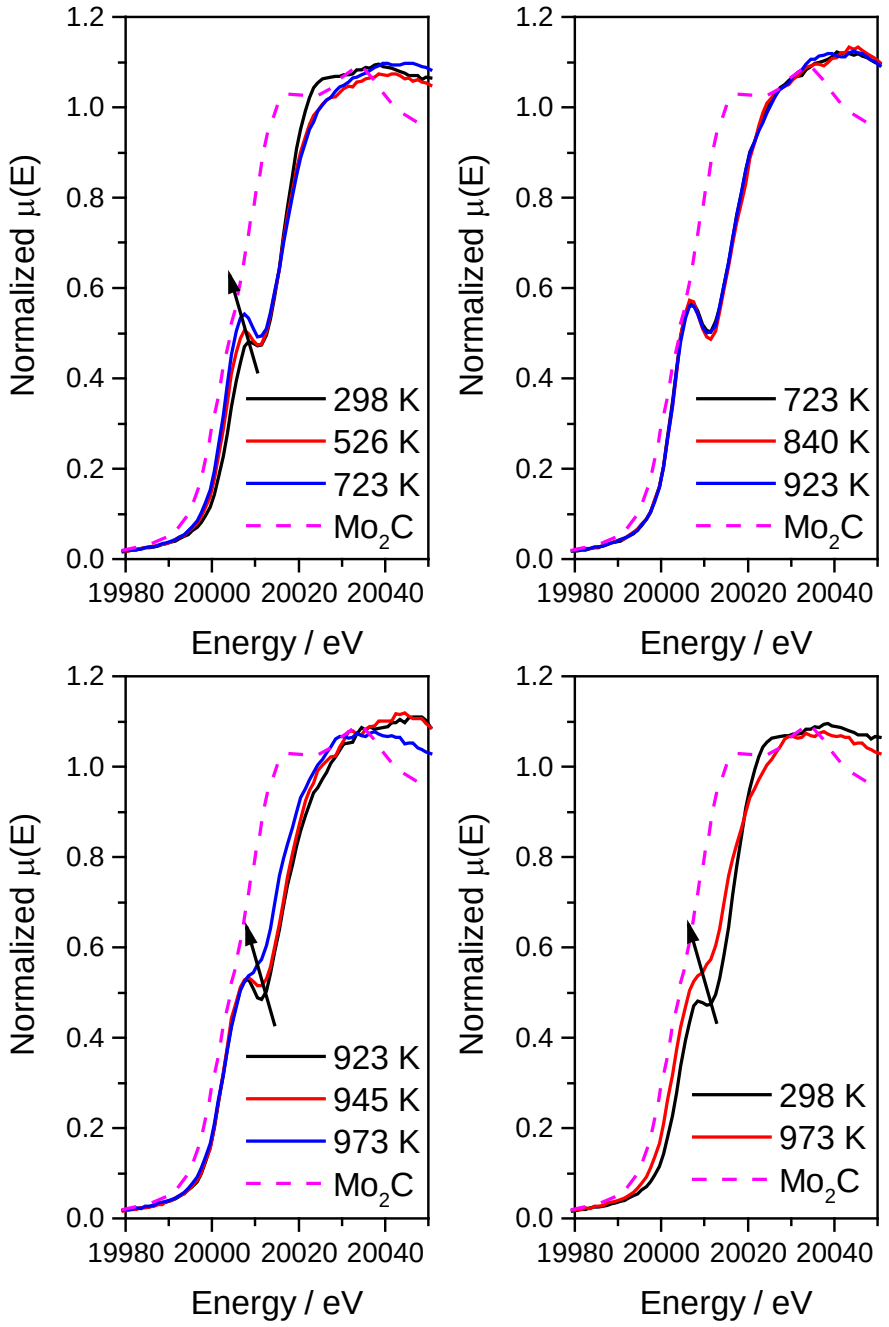

Figure 5.6 X-ray absorption near edge structure (XANES) of 2% Mo/[B]ZSM-5 during in-situ carburization process

The Extended X-ray Absorption Fine Structure (EXAFS) of the Mo in the 2% Mo/[B]ZSM-5 and standard compounds are displayed in Figure 5.7. The sample calcined at 773 K showed doublet peaks at ~1.2 Å while the intensity of all features beyond 3 Å are much weaker; these results reveal that MoO_3 crystallites are dissociated into smaller particles such as mono/binuclear molybdenum oxides.[34] The peaks at ~1.2 Å indicate the formation of Mo centers in tetrahedral coordination instead of the initial octahedral coordination environment. This observation is also in consistence with our previous discussion from the UV/VIS results. After the carburization with 20% CH_4/H_2, the molybdenum oxide species were reduced and carburized to form molybdenum carbide. As shown in Figure 6, the newly formed MoC_x species give rise to two peaks at ~1 and 2 Å. These peaks however cannot be described only using carbon neighbors in the first shell simulation, which usually only present one strong peak at ~2.5 Å as reported by others.[8, 13, 33] Instead they can be well described by one oxygen neighbor near 1.7 Å and three carbon neighbors near 2 Å and was also reported by Li et al. when describing the mechanism of the formation of MoC_x species on [Al]ZSM-5.[34] In the bulk Mo_2C, Mo has three carbon neighbors at a distance of 2.1 Å and twelve Mo neighbors at distances from 2.9 to 3.1 Å.[8] The absence of Mo-Mo pairs at the distance around 3 Å for the carburized sample suggests that the Mo small species formed upon calcination do not aggregate into larger clusters upon carburization.

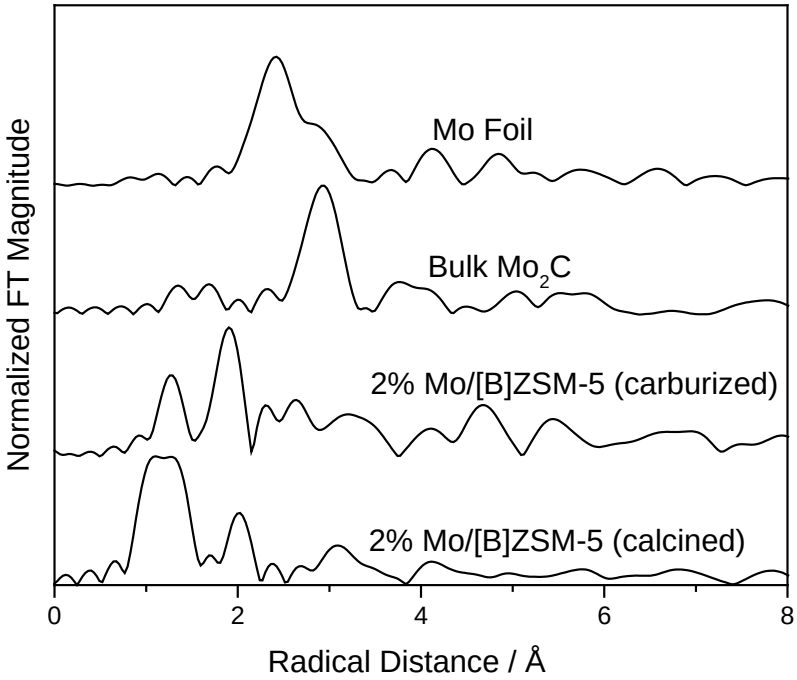

Figure 5.7 Radical structure function of Mo in standard compounds and in 2% Mo/[B]ZSM-5 before and after *in-situ* carburization

5.3.5 FT-IR Study for the Catalysts during the Synthesis Steps

In the typical [Al]ZSM-5 catalysts for the methane aromatization reactions the zeolite offers anchoring sites for the metal to disperse, and as the co-catalyst, the Brønsted acid sites catalyze the ethylene oligomerization reaction to aromatics.[33] Diffused reflectance FT-IR experiments were carried out to compare the role of [B]ZSM-5 to that of the [Al]ZSM-5 (Figure 5.8). The 2% Mo/[Al]ZSM-5 showed two IR bands assigned to OH stretching vibrations: the band at 3743 cm^{-1} attributed to terminal silanol groups,[35] and the band at 3610 cm^{-1} is typical for the acidic bridging OH of Si–OH–Al.[18] For the [B]ZSM-5, the OH vibration signal from silanol groups is slightly red-shifted to 3735 cm^{-1}, and the OH vibration band from Si–OH···B is observed at 3724 cm^{-1} and 3709 cm^{-1}. In a zeolite framework, the boron atom is

coplanar with three oxygens due to its small atomic diameter, and the distance to the fourth oxygen is too long to form strong bond.[35] Therefore the acidity of the bridging OH in [B]ZSM-5 is much weaker than that of [Al]ZSM-5. After the Mo impregnation, the intensity of the IR bands decreased, implying the substitution of the molybdenum oxides to the protons of the exchangeable OH groups. The intensity further decreased after a calcination at 773 K as a result of the molybdenum oxides being better dispersed as smaller clusters onto more anchoring sites, which is in agreement with the previous results from UV-VIS and XAS.

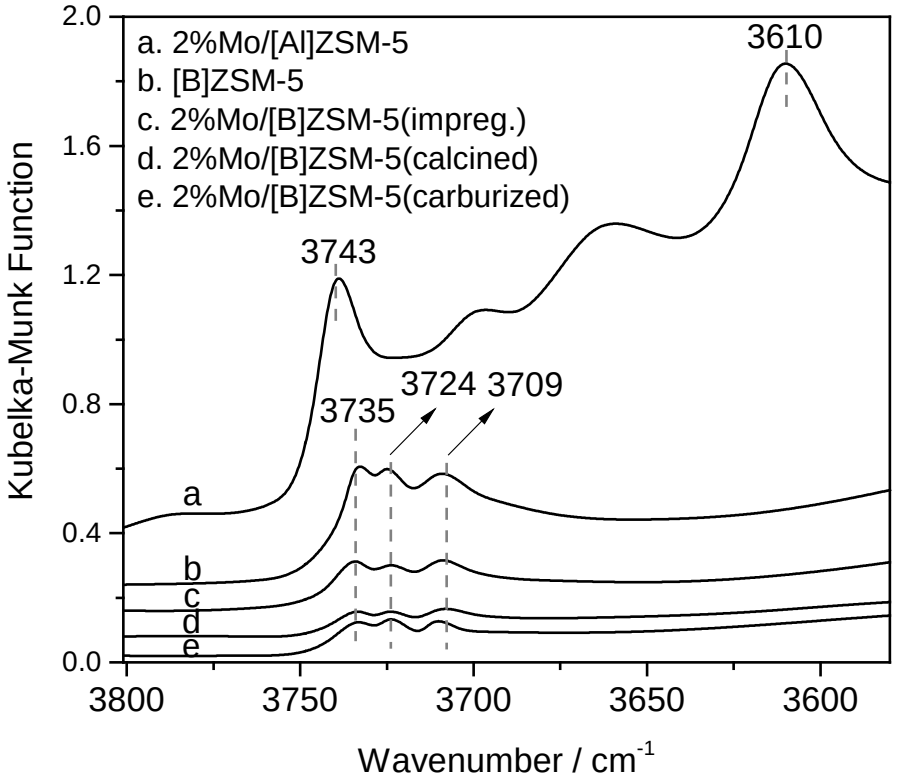

Figure 5.8 FT-IR spectra of 2%Mo/[Al]ZSM-5 and 2%Mo/[B]ZSM-5

5.4 Catalytic Tests

The catalytic properties were evaluated in a flow reactor under conditions similar to conditions reported in the literature for [Mo]-Al-ZSM-5 (923 K, 1 atm, 5% CH_4/He flow of 20 sccm, 50mg Mo_2C/[B]ZSM-5). Typically, 50 mg of the calcined Mo/[B]ZSM-5 was loaded into the reactor followed by carburization in 20% (vol.) CH_4/H_2. This step takes about 16 hours with the temperature ramping from 298 K to 623 K at 2 K/min, then to 973 K at 1 K/min, and held at 973 K for 8 hours. After this step, the system was cooled to the reaction temperature in He.[36] After the temperature was stabilized, a reaction gas consisting of 5% (vol) CH_4/He was fed into the system and the products are analyzed with an online GC equipped with TCD and FID detectors (Figure 5.9). Due to thermodynamic limitations, the conversion of methane around 1% with a 90%+ selectivity to ethylene instead of benzene. In terms of the catalyst stability of the methane aromatization reactions on Mo/[Al]ZSM-5, the Brønsted acid sites catalyzed oligomerization reaction may cause carbon deposition, which further covers the active site and leads to catalyst deactivation within a few hours.[11] According to this catalyst deactivation mechanism, Mo/[B]ZSM-5 is expected to have higher stability for methane activation reaction due to the nature of low acidity. Our result shows that the catalyst is very stable through the run, as the rate only decreases to 93% of initial reaction rate after 18 h.

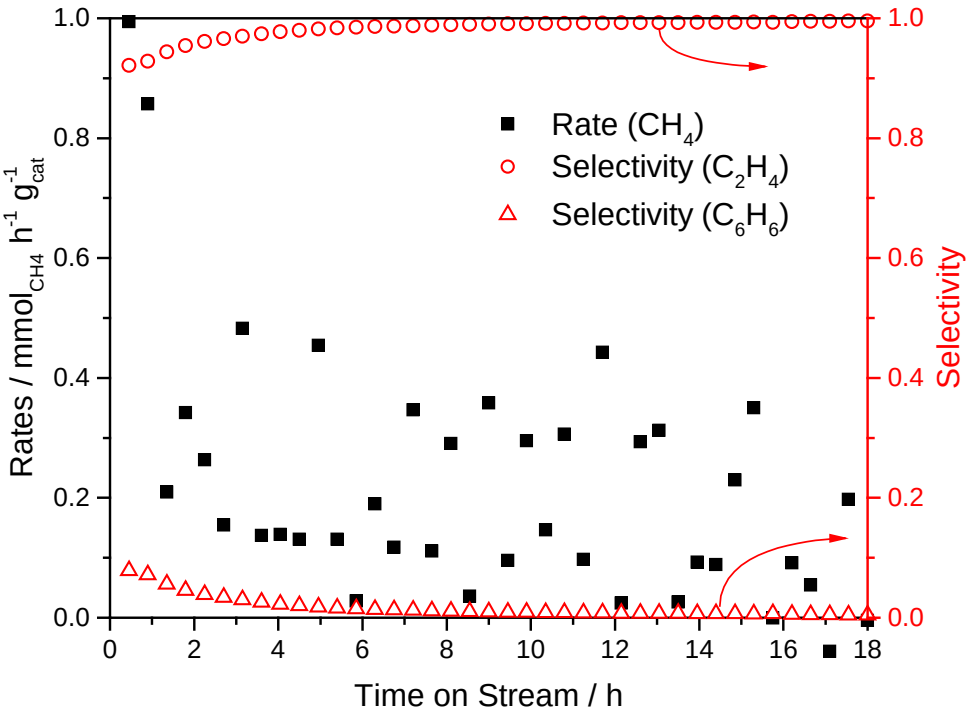

Figure 5.9 Methane activation on 2%Mo/[B]ZSM-5

5.4.1 T-test for the Reaction Data

The noisy data of methane reaction rate in Figure 5.9, is presented here because the rate is calculated from a subtraction of two large numbers (methane concentration before and after reaction). Therefore a linear regression was fitted with the rate of methane as a function of time on stream. A null hypothesis H_0=0 of the slope and the intercept is tested to verify if there is significant linear relationship between the methane rate and the time on stream. The P-value for the slope is ~0.001 and for the intercept is 0.000. In both cases, the null hypothesis is rejected, suggesting that both slope and intercept value does not equal to zero. The details of the t-test can be found in the following session.

The Hypothesis tests are performed on the slope and intercept of the reaction data listed in Table 5.3:

Table 5.3 Methane reaction rate (y) as a function of time on stream (x)

Time on stream x (h)	Methane rate y (mmol h^{-1} g^{-1})	Time on stream x (h)	Methane rate y (mmol h^{-1} g^{-1})
0.45	0.99412	9.45	0.09572
0.9	0.85691	9.9	0.29498
1.35	0.20966	10.35	0.14661
1.8	0.34177	10.8	0.30632
2.25	0.26344	11.25	0.09712
2.7	0.15439	11.7	0.44297
3.15	0.48269	12.15	0.02451
3.6	0.13715	12.6	0.29324
4.05	0.13863	13.05	0.31225
4.5	0.13055	13.5	0.02605
4.95	0.45443	13.95	0.09276
5.4	0.13058	14.4	0.08826
5.85	0.02756	14.85	0.22991
6.3	0.18987	15.3	0.35021
6.75	0.11755	15.75	-5.29e-04
7.2	0.34646	16.2	0.09137
7.65	0.11131	16.65	0.05453
8.1	0.29052	17.1	0.05638
8.55	0.03607	17.55	0.19757
9	0.35796	18	0.0048

Estimated regression line for the data listed above (using method of least squares):

$$y = 0.40578 - 0.01999x \qquad \text{Eqn. 5.1}$$

with $\alpha = 0.40578$, $\beta = -0.01999$, we can have the following equations,

$$S_{xx} = \sum_{i=1}^{n}(x_i - \bar{x})^2 \qquad \text{Eqn. 5.2}$$

$$S_{yy} = \sum_{i=1}^{n}(y_i - \bar{y})^2 \qquad \text{Eqn. 5.3}$$

$$S_{xy} = \sum_{i=1}^{n}(x_i - \bar{x})(y_i - \bar{y}) \quad \text{Eqn. 5.4}$$

$$b = S_{xy}/S_{xx} \quad \text{Eqn. 5.5}$$

$$s^2 = \frac{SSE}{n-2} = \sum_{i=1}^{n}\frac{(y_i - \hat{y}_i)^2}{n-2} = \frac{S_{yy} - bS_{xy}}{n-2} \quad \text{Eqn. 5.6}$$

n = 40, S_{xx} = 1079.32, S_{yy} = 1.77, S_{xy} = -21.58, s = 0.1878

With the above information being collected, the hypothesis test on the slope is firstly performed:

H_0: $\beta = 0$

H_1: $\beta \neq 0$

Therefore,

$$t = \frac{\beta - \beta_0}{s/\sqrt{S_{xx}}} = \frac{-0.01999 - 0}{0.1878/\sqrt{1079.32}} = -3.497$$

with n – 2 = 38 degrees of freedom (P~1.2e-3).The result suggests that the null hypothesis is rejected, and the slope value does not equal to zero.

Hypothesis testing on the intercept is conducted in the similar way below:

H_0: $\alpha = 0$

H_1: $\alpha \neq 0$

Therefore,

$$t = \frac{\alpha - \alpha_0}{s\sqrt{\sum_{i=1}^{n} x_i^2/n\, S_{xx}}} = \frac{0.40578 - 0}{0.1878\sqrt{\frac{4483.35}{40 * 1079.32}}} = 6.705$$

with n – 2 = 38 degrees of freedom (P~6.23e-8). The p-value of 6.28e-8 suggests the null hypothesis is rejected, and the intercept value does not equal to zero as well.

5.4.2 Reaction Results Comparison with the Literature of Mo/[Al]ZSM-5

The Mo/[Al]ZSM-5 has been extensively studied since Wang[5] first discovered its novel property of methane direct dehydroaromatization to benzene.[3, 6-11, 14, 33, 37-40] As shown in Figure 5.10, in comparison to Mo_2C/[Al]ZSM-5, Mo_2C/[B]ZSM-5 showed 90% selectivity towards ethylene, with only 7% selectivity to benzene. In contrast Li[41] has reported a similar selectivity for this reaction with Mo_2C/[B]ZSM-5 to that with Mo_2C/[Al]ZSM-5 (88% benzene and 3% ethylene at initial and 68% benzene and 24% ethylene after 120 min). The difference in selectivity between the results reported here and those of Li et al is due to the presence of aluminum impurities in their boron source, impurities that would introduce strong acid sites into their samples. Note too that a different catalyst synthesis method was applied in their report where Mo precursor MoO_3 and [B]ZSM-5 were physically mixed and grinded, although both impregnation and physical mixture synthesis showed similar methane conversion and products selectivity in the case of [Al]ZSM-5, as Borry and co-workers reported.[7]

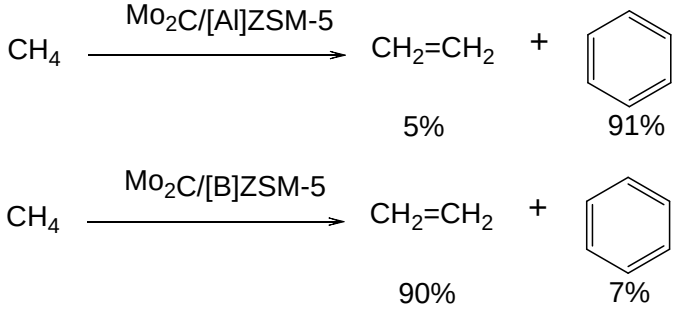

Figure 5.10 Methane activation products selectivity of Mo_2C/[Al]ZSM-5 vs. Mo_2C/[B]ZSM-5

The apparent activation energy of methane coupling reaction to ethylene was measured with a WHSV of 0.4 h^{-1}, at T = 918~933 K, and atmospheric pressure. A high activation energy of 137 kJ/mol was obtained (Figure 5.11). The measured activation energy is lower than the theoretical enthalpy (217 kJ/mol at 923 K) of this reaction. In the Mo/[Al]ZSM-5, the initial activation energy of C-H bond was discussed based on DFT and other computational simulation methods by various authors. Xing et al.[42] found a lowest activation energy of 106 kJ/mol for the C-H bond dissociation over $Mo_2(CH_2)_5$/[Al]ZSM-5 dimers. Zhou et al.[43] reported that MoO_2 center is active for C-H activation with only an energy barrier of 91 kJ/mol.

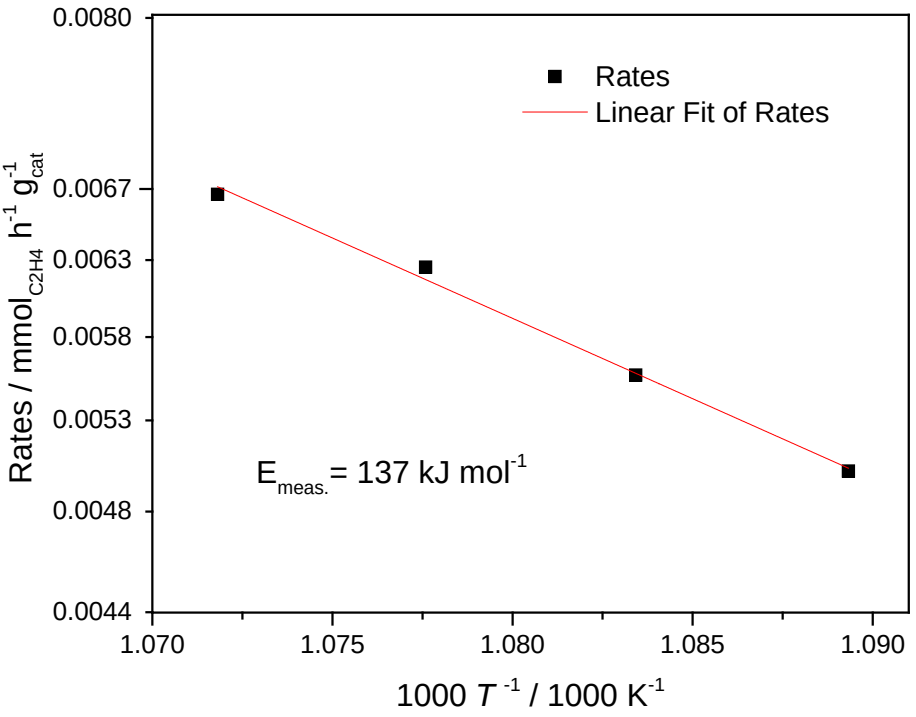

Figure 5.11 Measured apparent activation energy of methane coupling reaction with 2% Mo_2C/[B]ZSM-5

5.5 Conclusions

A highly selective methane non-oxidative coupling catalyst Mo_2C/[B]ZSM-5 was synthesized and characterized. Boron is employed instead of aluminium in the zeolite framework, which leads to a dramatic decrease in the zeolite acidity. 2% wt. of molybdenum was loaded into the zeolite by wetness impregnation. After calcination, mono and binuclear Mo oxide species were anchored onto the zeolite surface, as a high UV-VIS band gap energy (4.1 eV) was observed.[30] Molybdenum oxides were reduced and carburized to form well dispersed and isolated molybdenum carbides, as proved by the absence of Mo-Mo pairs in the EXAFS measurement. Due to the low acidity of the support, the catalyst shows a high selectivity towards ethylene (~90%) instead of aromatics. Ethylene oligomerization reaction, which is responsible for heavy coke formation, was thus inhibited. As a result, no significant catalyst deactivation was observed during the 18-hour long test.

REFERENCES

[1] J.H. Lunsford, Catalytic conversion of methane to more useful chemicals and fuels: a challenge for the 21st century, Catalysis Today, 63 (2000) 165-174.

[2] A.T. Ashcroft, A.K. Cheetham, M.L.H. Green, P.D.F. Vernon, PARTIAL OXIDATION OF METHANE TO SYNTHESIS GAS-USING CARBON-DIOXIDE, Nature, 352 (1991) 225-226.

[3] T.V. Choudhary, E. Aksoylu, D.W. Goodman, Nonoxidative activation of methane, Catalysis Reviews-Science and Engineering, 45 (2003) 151-203.

[4] PwC, Shale gas: Reshaping the US chemicals industry, in, http://www.pwc.com/us/en/industrial-products/publications/shale-gas-chemicals-industry-potential.html, 2013.

[5] L.S. Wang, L.X. Tao, M.S. Xie, G.F. Xu, J.S. Huang, Y.D. Xu, DEHYDROGENATION AND AROMATIZATION OF METHANE UNDER NONOXIDIZING CONDITIONS, Catalysis Letters, 21 (1993) 35-41.

[6] B.M. Weckhuysen, D.J. Wang, M.P. Rosynek, J.H. Lunsford, Conversion of methane to benzene over transition metal ion ZSM-5 zeolites - I. Catalytic characterization, Journal of Catalysis, 175 (1998) 338-346.

[7] R.W. Borry, Y.H. Kim, A. Huffsmith, J.A. Reimer, E. Iglesia, Structure and density of Mo and acid sites in Mo-exchanged H-ZSM5 catalysts for nonoxidative methane conversion, Journal of Physical Chemistry B, 103 (1999) 5787-5796.

[8] W.P. Ding, S.Z. Li, G.D. Meitzner, E. Iglesia, Methane conversion to aromatics on Mo/H-ZSM5: Structure of molybdenum species in working catalysts, Journal of Physical Chemistry B, 105 (2001) 506-513.

[9] Y.D. Xu, S.T. Liu, L.S. Wang, M.S. Xie, X.X. Guo, METHANE ACTIVATION WITHOUT USING OXIDANTS OVER MO/HZSM-5 ZEOLITE CATALYSTS, Catalysis Letters, 30 (1995) 135-149.

[10] F. Solymosi, J. Cserenyi, A. Szoke, T. Bansagi, A. Oszko, Aromatization of methane over supported and unsupported Mo-based catalysts, Journal of Catalysis, 165 (1997) 150-161.

[11] D.J. Wang, J.H. Lunsford, M.P. Rosynek, Characterization of a Mo/ZSM-5 catalyst for the conversion of methane to benzene, Journal of Catalysis, 169 (1997) 347-358.

[12] B.M. Weckhuysen, M.P. Rosynek, J.H. Lunsford, Characterization of surface carbon formed during the conversion of methane to benzene over Mo/H-ZSM-5 catalysts, Catalysis Letters, 52 (1998) 31-36.

[13] W.P. Ding, G.D. Meitzner, E. Iglesia, The effects of silanation of external acid sites on the structure and catalytic behavior of Mo/H-ZSM5, Journal of Catalysis, 206 (2002) 14-22.

[14] D. Ma, Y. Lu, L.L. Su, Z.S. Xu, Z.J. Tian, Y. Xu, L.W. Lin, X.H. Bao, Remarkable improvement on the methane aromatization reaction: A highly selective and coking-resistant catalyst, Journal of Physical Chemistry B, 106 (2002) 8524-8530.

[15] P.J. Chupas, K.W. Chapman, C. Kurtz, J.C. Hanson, P.L. Lee, C.P. Grey, A versatile sample-environment cell for non-ambient X-ray scattering experiments, Journal of Applied Crystallography, 41 (2008) 822-824.

[16] H. Vankoningsveld, J.C. Jansen, H. Vanbekkum, THE MONOCLINIC FRAMEWORK STRUCTURE OF ZEOLITE H-ZSM-5 - COMPARISON WITH THE ORTHORHOMBIC FRAMEWORK OF AS-SYNTHESIZED ZSM-5, Zeolites, 10 (1990) 235-242.

[17] D.T. On, S. Kaliaguine, L. Bonneviot, TITANIUM BORALITES WITH MFI STRUCTURE CHARACTERIZED USING XRD, XANES, IR, AND UV-

VISIBLE TECHNIQUES - EFFECT OF HYDROGEN-PEROXIDE ON THE PREPARATION, Journal of Catalysis, 157 (1995) 235-243.

[18] H. Koller, C.-Y. Chen, S.I. Zones, Selectivities in Post-Synthetic Modification of Borosilicate Zeolites, Topics in Catalysis, 58 (2015) 451-479.

[19] A. Cichocki, J. Datka, A. Olech, Z. Piwowarska, M. Michalik, CHANGES IN THE STRUCTURE OF ZSM-5 ZEOLITES DURING BORON AND ALUMINUM SUBSTITUTION, Journal of the Chemical Society-Faraday Transactions, 86 (1990) 753-756.

[20] B.L. Meyers, S.R. Ely, N.A. Kutz, J.A. Kaduk, E. Vandenbossche, DETERMINATION OF STRUCTURAL BORON IN BOROSILICATE MOLECULAR-SIEVES VIA X-RAY-DIFFRACTION, Journal of Catalysis, 91 (1985) 352-355.

[21] L. Wang, W.K. Hall, THE PREPARATION AND GENESIS OF MOLYBDENA ALUMINA AND RELATED CATALYST SYSTEMS, Journal of Catalysis, 77 (1982) 232-241.

[22] F.A. Cotton, G. Wilkinson, C.A. Murillo, M. Bochmann, Advanced Inorganic Chemistry, 6 ed., Wiley, New York, 1999.

[23] J.H. Ashley, P.C. Mitchell, COBALT-MOLYBDENUM-ALUMINA HYDRODESULPHURISATION CATALYSTS .1. A SPECTROSCOPIC AND MAGNETIC STUDY OF FRESH CATALYST AND MODEL COMPOUNDS, Journal of the Chemical Society a -Inorganic Physical Theoretical, (1968) 2821-&.

[24] M. Fournier, C. Louis, M. Che, P. Chaquin, D. Masure, POLYOXOMETALLATES AS MODELS FOR OXIDE CATALYSTS .1. AN UV VISIBLE REFLECTANCE STUDY OF POLYOXOMOLYBDATES - INFLUENCE OF POLYHEDRA ARRANGEMENT ON THE ELECTRONIC-TRANSITIONS AND COMPARISON WITH SUPPORTED MOLYBDENUM CATALYSTS, Journal of Catalysis, 119 (1989) 400-414.

[25] L.G. van de Water, J.A. Bergwerff, T.A. Nijhuis, K.P. de Jong, B.M. Weckhuysen, UV-Vis microspectroscopy: Probing the initial stages of supported

metal oxide catalyst preparation, Journal of the American Chemical Society, 127 (2005) 5024-5025.

[26] P.C. Mitchell, F. Trifiro, SPECTROSCOPIC INVESTIGATION OF BISMUTH-MOLYBDENUM-OXIDE CATALYSTS, Journal of the Chemical Society a - Inorganic Physical Theoretical, (1970) 3183-&.

[27] N.T. Vasenin, V.F. Anufrienko, I.Z. Ismagilov, T.V. Larina, E.A. Paukshtis, E.V. Matus, L.T. Tsikoza, M.A. Kerzhentsev, Z.R. Ismagilov, Effect of thermal treatment on states of molybdenum in Mo/H-ZSM-5 catalyst for methane dehydroaromatization: ESR and UV-VIS study, Topics in Catalysis, 32 (2005) 61-70.

[28] A. Martinez, E. Penis, Non-oxidative methane dehydroaromatization on Mo/HZSM-5 catalysts: Tuning the acidic and catalytic properties through partial exchange of zeolite protons with alkali and alkaline-earth cations, Applied Catalysis a-General, 515 (2016) 32-44.

[29] M.W. Ngobeni, A.F. Carley, M.S. Scurrell, C.R. Nicolaides, The effects of boron and silver on the oxygen-free conversion of methane over Mo/H-ZSM-5 catalysts, Journal of Molecular Catalysis a-Chemical, 305 (2009) 40-46.

[30] R.S. Weber, EFFECT OF LOCAL-STRUCTURE ON THE UV-VISIBLE ABSORPTION EDGES OF MOLYBDENUM BRIDE CLUSTERS AND SUPPORTED MOLYBDENUM OXIDES, Journal of Catalysis, 151 (1995) 470-474.

[31] S.B. Xie, K.D. Chen, A.T. Bell, E. Iglesia, Structural characterization of molybdenum oxide supported on zirconia, Journal of Physical Chemistry B, 104 (2000) 10059-10068.

[32] J. Bedard, D.-Y. Hong, A. Bhan, CH4 dehydroaromatization on Mo/H-ZSM-5: 1. Effects of co-processing H-2 and CH3COOH, Journal of Catalysis, 306 (2013) 58-67.

[33] S.T. Liu, L. Wang, R. Ohnishi, M. Ichikawa, Bifunctional catalysis of Mo/HZSM-5 in the dehydroaromatization of methane to benzene and naphthalene

XAFS/TG/DTA/MASS/FTIR characterization and supporting effects, Journal of Catalysis, 181 (1999) 175-188.

[34] W. Li, G.D. Meitzner, R.W. Borry, E. Iglesia, Raman and X-ray absorption studies of Mo species in Mo/H-ZSM5 catalysts for non-oxidative CH4 reactions, Journal of Catalysis, 191 (2000) 373-383.

[35] J. Datka, Z. Piwowarska, THE PROPERTIES OF BORALITES STUDIED BY INFRARED-SPECTROSCOPY, Journal of the Chemical Society-Faraday Transactions I, 85 (1989) 47-53.

[36] A. Mehdad, R.E. Jentoft, F.C. Jentoft, Passivation agents and conditions for Mo2C and W2C: Effect on catalytic activity for toluene hydrogenation, Journal of Catalysis, 347 (2017) 89-101.

[37] V.T.T. Ha, L.V. Tiep, P. Meriaudeau, C. Naccache, Aromatization of methane over zeolite supported molybdenum: active sites and reaction mechanism, Journal of Molecular Catalysis a-Chemical, 181 (2002) 283-290.

[38] D. Ma, Y.Y. Shu, M.J. Cheng, Y.D. Xu, X.H. Bao, On the induction period of methane aromatization over Mo-based catalysts, Journal of Catalysis, 194 (2000) 105-114.

[39] R. Ohnishi, S.T. Liu, Q. Dong, L. Wang, M. Ichikawa, Catalytic dehydrocondensation of methane with CO and CO2 toward benzene and naphthalene on Mo/HZSM-5 and Fe/Co-modified Mo/HZSM-5, Journal of Catalysis, 182 (1999) 92-103.

[40] J.-P. Tessonnier, B. Louis, S. Rigolet, M.J. Ledoux, C. Pham-Huu, Methane dehydro-aromatization on Mo/ZSM-5: About the hidden role of Bronsted acid sites, Applied Catalysis a-General, 336 (2008) 79-88.

[41] S. Li, D. Ma, Q.B. Kan, P. Wu, Y.B. Peng, C.L. Zhang, M.S. Li, Y.H. Fu, J.Y. Shen, T.H. Wu, X.H. Bao, Methane aromatization in the absence of oxygen over Mo/H B ZSM-5 catalysts, Reaction Kinetics and Catalysis Letters, 70 (2000) 349-356.

[42] S.Y. Xing, D.H. Zhou, L. Cao, X. Li, Density Functional Theory Study on Structure of Molybdenum Carbide and Catalytic Mechanism for Methane Activation over ZSM-5 Zeolite, Chinese Journal of Catalysis, 31 (2010) 415-422.

[43] D.H. Zhou, D. Ma, Y. Wang, X.C. Liu, X.H. Bao, Study with density functional theory method C-H bond activation on the MoO2/HZSM-5 on methane active center, Chemical Physics Letters, 373 (2003) 46-51.

Chapter 6

CONCLUSIONS AND RECOMMENDATIONS

6.1 Conclusions

This thesis discusses the development of catalytic processes for the production of biofuels and valuable chemicals from renewable biomass and inexpensive and abundant natural gas. Specifically three catalytic processes investigated: 1) Selective hydrodeoxygenation of furfural to 2-methylfuran on iron-promoted silica-supported copper catalyst; 2) Hydrogenation of carboxylic acids to the corresponding aldehydes over chromium-containing catalyst; 3) Non-oxidative coupling of methane to ethylene on Mo_2C/[B]ZSM-5. The catalytic reactions were investigated and in each case a mechanism to understand catalytic activity and selectivity were proposed. Also the catalysts were characterized with surface and bulk techniques to understand the structure-property relationship. The following accomplishments were achieved.

In Chapter 3, the furfural hydrogenation to furfuryl alcohol and 2-methylfuran has been investigated over Cu/SiO_2 and $Cu\text{-}Fe/SiO_2$ catalyst at low metal loading. It was found that supported Cu/SiO_2 converts furfural to furfuryl alcohol, with only a selectivity of 11% to 2-methylfuran and that the addition of a small amount of Fe (up to 0.15% w/w) to the Cu (1% w/w) catalyst increases reaction rates by more than a factor of 3 without change in selectivity (31% furfural conversion, 16% selectivity to 2-methylfuran). Catalyst pre-reduction at a temperature of 543 K changes the catalyst properties leading to a significant enhancement of 2-methylfuran selectivity (90%), when compared to pre-treatment at 483 K. TPR investigations indicate that the

reduction of Fe was not complete at either reduction temperature. In situ FT-IR experiments with NO as the probe molecule further showed that Fe^{2+} active sites are generated after a reduction at a temperature of 543 K but not at 483K. We have found two mechanisms that explain the promotion effects of iron: firstly the co-impregnated iron increased the copper dispersion and reaction rates substantially in what may be called structural promotion effect; secondly the partially reduced Fe can act as a co-catalyst and selectively convert furfuryl alcohol to 2-methylfuran, which was responsible for the reaction selectivity shift after the addition of Fe. But this second effect is only observed if the catalyst is reduced at the higher temperature.

Chapter 4 investigates the hydrogenation of carboxylic acids to the corresponding aldehydes on chromium-containing catalysts. The chromium oxide catalyst was evaluated with a series of carboxylic acids of propionic acid (C3) to hexanoic acid (C6) in a flow reactor and high selectivity (~90%) to aldehydes were observed. H_2-D_2 scrambling experiments were carried out for the chromium oxides and the results confirmed that hydrogen dissociation can occur very fast even at room temperature on the chromium oxide surface. Reaction results of different chromium oxides and in-situ UV-VIS studies confirmed that trivalent Cr(III) was the active phase in this reaction instead of the high-valent chromium species, such as Cr(IV) and Cr(VI). The reaction mechanism was investigated using D_2 isotope labeling experiments and the adsorption configurations of the acids were discussed. Finally, the rate expression of the aldehyde was derived through a Mars and van Krevelen type reaction and a kinetics experiments were carried out to validate the rate form suggested by this mechanism.

Chapter 5 presents an investigation of the non-oxidative coupling of methane to ethylene with Mo_2C/[B]ZSM-5 catalyst. The effect of zeolite acidity was investigated in the methane activation reactions. Incorporation of boron in the framework of zeolite ZSM-5 gives rise to a material with very week Brønsted acidity. The strongly acid, bridged hydroxyl group (Si-OH-Al) was not observed for [B]ZSM-5 in FT-IR spectra, indicating the surface acidity is in fact much lower than the [Al]ZSM-5. As the primary product of methane coupling reaction on Mo_2C, it was found that ethylene does not react further via oligomerization and dehydrogenation to form aromatics on the [B]ZSM-5. In-situ UV-VIS studies suggested that Mo oxides was dispersed as mono/binuclear Mo species and the further carburized Mo_2C in methane/hydrogen mixtures show that the sample catalyzes the methane coupling reaction. In-situ XAS studies showed that Mo_2C particles were anchored on the weak Brønsted acid sites and an absence of Mo-Mo pairs in EXAFS indicated that mono/binuclear molybdenum oxides species formed upon calcination does not further aggregate into large particles.

6.2 Recommendations for Future Work

6.2.1 Furfural Hydrodeoxygenation

In Chapter 3, iron-promoted silica supported copper is shown to be an efficient catalyst to selectively convert furfural to 2-methylfuran. It is interesting to investigate if this catalyst can be used to other biomass-derived oxygenates containing carbonyl group, such as acetol, 5-methylfurfural, levulinic acid, and levulinic acid esters.

In general, a metal-metal oxide type catalyst can be a great model for the hydrogenation of biomass-derived oxygenates. In addition to Cu-FeO_x, many other

catalysts have been reported. For example, Ru-RuO_2[1] and Cu-Co_3O_4[2] were reported for the hydrodeoxygenation of furfural, and Cu-MnO_2,[3] was reported for the hydrogenation of dimethyl succinate. To be specific, the combination of metal-metal oxide pair can be chosen with the following guidelines. First, the metals should be inexpensive and non-toxic to be an economic and green catalyst for the industrial process. Second, copper-based catalyst could be a good starting point, since copper has a good hydrogenation capacity and is less expensive than noble metals. Finally for the metal oxide, the metal-oxygen bond strength should be 'intermediate', considering the redox reaction of interest. If the metal-oxygen bond is too strong, which means the reducibility of the metal is poor, the oxygen vacancies are not likely to be generated and the catalyst may not be selective in terms of hydrogenation. In the contrary, the surface C–O bond cleavage rate will be limited if the metal-oxygen bond is too weak.

Brands et al.[4] reported a volcano type catalyst activity plot in ester hydrogenolysis as a function of metal-oxygen bond strength. In their report, cobalt, nickel, iron, molybdenum, zinc, manganese, yttrium, and magnesium oxides were tested and the ester hydrogenolysis activity was presented in the order: Mo>Co≥Zn≥Mn>Fe≥Y>Ni>>Mg. Before the screening experiments of all these transition metal oxides, the neighbors (Co, Ni, Mo, Zn) that have similar metal oxygen bond strength to iron are suggested to be investigated at first. Srivastava et al.[2, 5] reported a Cu-CoO_x/SiO_2 catalyst for the production of furfuryl alcohol from furfural and Cu-CoO_x/Al_2O_3 for 2-methylfuran. Cu-Ni was reported by numerous authors to convert furfural to furfuryl alcohol,[6] tetrahedralfurfuryl alcohol,[7] and cyclopentanone.[8] However, not much work was found on supported Cu-Mo and Cu-Zn catalysts for the hydrogenation of furfural and other biomass derived oxygenates.

These metal combinations can be good candidates for the HDO reaction, but the catalyst support and reduction temperature are also needs to be considered carefully. As suggested by Srivastava's work, the Cu-Co catalysts on different supports showed different selectivity. In Chapter 3 it have been already discussed the effect of reduction temperature of Cu-Fe catalyst on the products selectivity, and also all the Cu-Ni catalysts listed above were all reduced at different temperatures.

On the other hand, the Cu-Fe binary spinel structure ($CuFe_2O_4$) was formed during the calcination as discussed in Chapter 3. The further reduction of spinel structure oxide allowed the formation of better dispersed Cu active sites. Hirunsit and Faungnawakij[9] found that Cu-based catalysts reduced from Cu-metal spinel oxides showed a better activity than Cu catalyst or physical mixtures of Cu/metal oxides, for the reforming of oxygenated hydrocarbons. Such spinel oxide structures can also be formed with Co, Mn, and Cr as $CuCo_2O_4$, $CuMn_2O_4$, and $CuCr_2O_4$, which may be potential precursor candidates for the HDO reactions.

6.2.2 Carboxylic Acids Hydrogenation

Chromium-containing catalysts have shown excellent properties for the hydrogenation of carboxylic acids to the corresponding aldehydes. A series of (small) carboxylic acids, from acetic acid (C2) to hexanoic acid (C6), have been investigated on Cr_2O_3. An interesting finding in Chapter 4 is that the conversions of all other acids are high (~20%), except for acetic acid (<1%). Pestman et al. also found a poor reactivity of acetic acid on chromia and only ~8% selectivity to acetaldehyde was reported at 723 K.[10] According to their theory, the hydrogen spill-over is limited on chromia surface due to the high Cr-O bond strength.[11] However, the heterolytic dissociation of hydrogen on chromia have been presented in Chapter 4 and thus there

are other facts that limit the reaction of acetic acid on chromia. Diffused reflectance infrared Fourier transform spectroscopy (DRIFTS) experiments can be a useful approach to investigate the different reactivity of acetic acid and other carboxylic acids (C3-C6). Chen et al.[12] presented a study of propionic acid adsorption on supported Ru catalysts and found that propionic acid species were dominant on TiO_2, γ-Al_2O_3, while propionate and propanoyl species were presented on ZrO_2 surface. The different adsorbed surface species can lead to different products of either hydrogenation or ketonization products.[12] Other surface characterization techniques such as electron energy loss spectroscopy (EELS) can also provide information on the molecular adsorption/desorption of carboxylic acids on catalysts surface. Chen, Crowell, and Yates[13] suggest that the acetic acid undergoes O-H bond scission upon adsorption on Al(111) surface at 120 K, since no O-H stretching vibration was observed in the EELS. In addition, the vibration of (COO) mode was also not observed while the (Al-O) bond intensity increased, suggesting that the dissociated acetate chemisorbed to the Al(111) surface with the formation of two identical Al-O bonds. This results implied that upon adsorption, the OCO moiety showed a C_{2v} symmetry while the overall acetate has a Cs symmetry. This experiment was carried out at low temperature of 120 K with low dose of acetic acid on clean Al(111) surface.[13] However, this technique can be potentially be applied to other carboxylic acids adsorption on Cr_2O_3 catalyst.

The most promising catalyst of the ones investigated was the conventional bulk Cr_2O_3. This material only showed a 20% conversion for the C3-C6 acids. Since commercial chromium oxide only has a surface area of 8 m^2 g^{-1}(Sigma Aldrich), the reaction rates can be potentially increased by a factor of 10 or higher with a higher

surface area chromium oxide. Schwickardi et al.[14] reported a route to fabricate a wide variety of different metal oxides, with an impregnation of the activated carbons with metal salt solutions and subsequent calcination to burn off the carbon. According to their method, a BET surface area of 156 $m^2 g^{-1}$ was obtained for Cr_2O_3. Sinha and Suzuki[15] synthesized a 3D mesoporous chromium oxide prepared by a neutral templating route, where a surface of 202 $m^2 g^{-1}$ was reported. On the other hand, the supported Cr_2O_3 catalysts also have very high surface area, but they (such as Cr/Al_2O_3 in Chapter 4) showed low reactivity due to the limited ability of hydrogen dissociation of the high-valent chromium species formed on the supports. Therefore, it is interesting to investigate the reactivity of the high surface area bulk Cr_2O_3 catalysts.

6.2.3 Methane Coupling to Ethylene

In Chapter 5, we have presented non-oxidative coupling of methane to ethylene on Mo_2C/[B]ZSM-5 catalyst with a high selectivity (>90%). Through the 18-hour long reaction, the catalyst remained stable and no significant deactivation was observed. The catalyst deactivation, if there is any, is believed to occur at the surface acid sites due to the coke deposition.[16] The acid sites, however, are required for the formation of Mo_2C active species as the anchoring sites,[17] and the unsupported Mo_2C didn't show any reactivity in this reaction.[18] Therefore there is a balance between the catalyst activity and deactivation, and thus there is an optimum surface acid sites number. The acid sites of the zeolite can be presented with the Si/B ratio, as the Brønsted acid sites are related to the B concentration. For the materials presented in Chapter 5, a Si/B ratio of 70 was measured by ICP-MS. This value can be increased to study the reaction with less Brønsted acid sites, but was difficult to be further decreased through the hydrothermal synthesis method.

On the other hand, HZSM-5 supported Mo_2C was reported to show a highest activity and selectivity to benzene among the other types of zeolites as the support such as H-Beta, H-SAPO-34, and HMCM-41.[19] This was due to the fact that the pore diameter of HZSM-5 (5.4 Å) is close to the dynamic diameter of the benzene molecule (~6 Å) and the exhibit the best shape-selectivity towards the production of benzene. However, this may not be applicable to the methane coupling reaction, where ethylene is the dominant product and only trace amount of benzene is generated as the side product. Therefore it is interesting to investigate the effect of different types of zeolite as the support on the methane coupling reaction. For example, Zones and Nakagawa[20] reported a synthesis method of SSZ-33 converted from boron-beta zeolite with Si/B ratio of 14 – 16 depending on the ratio of SiO_2/B_2O_3 in the starting materials. Such zeolite of SSZ-33 with 12-membered rings and high boron concentration in the framework may allow the formation of more active molybdenum carbides species, thus it can potentially showed a higher conversion of methane.

REFERENCES

[1] J. Jae, W. Zheng, A.M. Karim, W. Guo, R.F. Lobo, D.G. Vlachos, The Role of Ru and RuO2 in the Catalytic Transfer Hydrogenation of 5-Hydroxymethylfurfural for the Production of 2,5-Dimethylfuran, Chemcatchem, 6 (2014) 848-856.

[2] S. Srivastava, G.C. Jadeja, J. Parikh, A versatile bi-metallic copper-cobalt catalyst for liquid phase hydrogenation of furfural to 2-methylfuran, Rsc Advances, 6 (2016) 1649-1658.

[3] Q. Hu, L. Yang, G.L. Fan, F. Li, Hydrogenation of biomass-derived compounds containing a carbonyl group over a copper-based nanocatalyst: Insight into the origin and influence of surface oxygen vacancies, Journal of Catalysis, 340 (2016) 184-195.

[4] D.S. Brands, E.K. Poels, A. Bliek, Ester hydrogenolysis over promoted Cu/SiO2 catalysts, Applied Catalysis a-General, 184 (1999) 279-289.

[5] S. Srivastava, N. Solanki, P. Mohanty, K.A. Shah, J.K. Parikh, A.K. Dalai, Optimization and Kinetic Studies on Hydrogenation of Furfural to Furfuryl Alcohol over SBA-15 Supported Bimetallic Copper-Cobalt Catalyst, Catalysis Letters, 145 (2015) 816-823.

[6] S. Sitthisa, D.E. Resasco, Hydrodeoxygenation of Furfural Over Supported Metal Catalysts: A Comparative Study of Cu, Pd and Ni, Catalysis Letters, 141 (2011) 784-791.

[7] L.J. Liu, H. Lou, M. Chen, Selective hydrogenation of furfural to tetrahydrofurfuryl alcohol over Ni/CNTs and bimetallic Cu-Ni/CNTs catalysts, International Journal of Hydrogen Energy, 41 (2016) 14721-14731.

[8] Y.L. Yang, Z.T. Du, Y.Z. Huang, F. Lu, F. Wang, J. Gao, J. Xu, Conversion of furfural into cyclopentanone over Ni-Cu bimetallic catalysts, Green Chemistry, 15 (2013) 1932-1940.

[9] P. Hirunsit, K. Faungnawakij, Cu-Cr, Cu-Mn, and Cu-Fe Spinel-Oxide-Type Catalysts for Reforming of Oxygenated Hydrocarbons, Journal of Physical Chemistry C, 117 (2013) 23757-23765.

[10] R. Pestman, R.M. Koster, J.A.Z. Pieterse, V. Ponec, Reactions of carboxylic acids on oxides .1. Selective hydrogenation of acetic acid to acetaldehyde, Journal of Catalysis, 168 (1997) 255-264.

[11] R. Pestman, R.M. Koster, V. Ponec, SELECTIVE HYDROGENATION OF ACETIC-ACID TOWARDS ACETALDEHYDE, Recueil Des Travaux Chimiques Des Pays-Bas-Journal of the Royal Netherlands Chemical Society, 113 (1994) 426-430.

[12] L.G. Chen, Y.P. Li, X.H. Zhang, Q. Zhang, T.J. Wang, L.L. Ma, Mechanistic insights into the effects of support on the reaction pathway for aqueous-phase hydrogenation of carboxylic acid over the supported Ru catalysts, Applied Catalysis a-General, 478 (2014) 117-128.

[13] J.G. Chen, J.E. Crowell, J.T. Yates, AN EELS AND TPD STUDY OF THE ADSORPTION AND DECOMPOSITION OF ACETIC-ACID ON THE AL(111) SURFACE, Surface Science, 172 (1986) 733-753.

[14] M. Schwickardi, T. Johann, W. Schmidt, F. Schuth, High-surface-area oxides obtained by an activated carbon route, Chemistry of Materials, 14 (2002) 3913-3919.

[15] A.K. Sinha, K. Suzuki, Three-dimensional mesoporous chromium oxide: A highly efficient material for the elimination of volatile organic compounds, Angewandte Chemie-International Edition, 44 (2005) 271-273.

[16] B.M. Weckhuysen, M.P. Rosynek, J.H. Lunsford, Characterization of surface carbon formed during the conversion of methane to benzene over Mo/H-ZSM-5 catalysts, Catalysis Letters, 52 (1998) 31-36.

[17] S.T. Liu, L. Wang, R. Ohnishi, M. Ichikawa, Bifunctional catalysis of Mo/HZSM-5 in the dehydroaromatization of methane to benzene and naphthalene XAFS/TG/DTA/MASS/FTIR characterization and supporting effects, Journal of Catalysis, 181 (1999) 175-188.

[18] F. Solymosi, J. Cserenyi, A. Szoke, T. Bansagi, A. Oszko, Aromatization of methane over supported and unsupported Mo-based catalysts, Journal of Catalysis, 165 (1997) 150-161.

[19] C.L. Zhang, S.A. Li, Y. Yuan, W.X. Zhang, T.H. Wu, L.W. Lin, Aromatization of methane in the absence of oxygen over Mo-based catalysts supported on different types of zeolites, Catalysis Letters, 56 (1998) 207-213.

[20] S.I. Zones, Y. Nakagawa, BORON BETA-ZEOLITE HYDROTHERMAL CONVERSIONS - THE INFLUENCE OF TEMPLATE STRUCTURE AND OF BORON CONCENTRATION AND SOURCE, Microporous Materials, 2 (1994) 543-555.

Appendix A

REPRINT PERMISSION

Reprint Permission for Text/Figures in Chapter 3

JOHN WILEY AND SONS LICENSE
TERMS AND CONDITIONS

Oct 06, 2017

This Agreement between Huibo Sheng ("You") and John Wiley and Sons ("John Wiley and Sons") consists of your license details and the terms and conditions provided by John Wiley and Sons and Copyright Clearance Center.

License Number	4175570065443
License date	Aug 24, 2017
Licensed Content Publisher	John Wiley and Sons
Licensed Content Publication	ChemCatChem
Licensed Content Title	Iron-Promotion of Silica-Supported Copper Catalysts for Furfural Hydrodeoxygenation
Licensed Content Author	Huibo Sheng,Raul F. Lobo
Licensed Content Date	Sep 30, 2016
Licensed Content Pages	7
Type of Use	Dissertation/Thesis
Requestor type	Author of this Wiley article
Format	Print and electronic
Portion	Full article
Will you be	No

translating?	
Title of your thesis / dissertation	Hydrogenation of Biomass Derived Oxygenates
Expected completion date	Aug 2017
Expected size (number of pages)	27
Requestor Location	Huibo Sheng 150 Academy St NEWARK, DE 19716 United States Attn: Huibo Sheng
Publisher Tax ID	EU826007151
Billing Type	Invoice
Billing Address	Huibo Sheng 150 Academy St NEWARK, DE 19716 United States Attn: Huibo Sheng
Total	**0.00 USD**